PFG

# Photogrammetrie Fernerkundung Geoinformation

Journal for Photogrammetry, Remote Sensing and Geoinformation Science

Organ der Deutschen Gesellschaft für Photogrammetrie, Fernerkundung und Geoinformation (DGPF) e. V.

Jahrgang 2013, Heft 1




E. Schweizerbart'sche Verlagsbuchhandlung
(Nägele u. Obermiller) Stuttgart 2013

Deutsche Gesellschaft für Photogrammetrie, Fernerkundung
und Geoinformation (DGPF) e.V.
Gegründet 1909

Die *Deutsche Gesellschaft für Photogrammetrie, Fernerkundung und Geoinformation* (DGPF) e.V. unterstützt als Mitglieds- bzw. Trägergesellschaft die folgenden Dachverbände:

International Society
for Photogrammetry
and Remote Sensing

Deutsche Arbeits-
gemeinschaft für
Mustererkennung e.V.

GeoUnion
Alfred-Wegener-Stiftung

Herausgeber:

Präsident: Prof. Dr. Thomas Kolbe, Technische Universität München, Institut für Geodäsie, GIS und Landmanagement, Lehrstuhl für Geoinformatik, Arcisstraße 21, 80333 München, Germany, Tel. +49-89-289-23888
Geschäftsstelle: Dr. Klaus-Ulrich Komp, c/o EFTAS Fernerkundung Technologietransfer GmbH, Oststraße 2–18, 48145 Münster, Germany, e-mail: klaus.komp@eftas.com
Published by: E. Schweizerbart'sche Verlagsbuchhandlung (Nägele u. Obermiller), Johannesstraße 3A, 70176 Stuttgart, Germany, Tel.: +49-711 351456-0, Fax: +49-711 351456-99, e-mail: mail@schweizerbart.de
Internet: http://www.schweizerbart.de
♾ Gedruckt auf alterungsbeständigem Papier nach ISO 9706-1994

ISSN 1432-8364
Science Citation Index Expanded (also known as SciSearch®) Journal Citation Reports/Science Edition

Erscheinungsweise: 6 Hefte pro Jahrgang.
Bezugspreis im Abonnement: € 229,– pro Jahrgang. Mitglieder der DGPF erhalten die Zeitschrift kostenlos. Der Online-Zugang ist im regulären Subskriptionspreis enthalten.
Anzeigenverwaltung: E. Schweizerbart'sche Verlagsbuchhandlung (Nägele u. Obermiller), Johannesstraße 3A, 70176 Stuttgart, Germany, Tel.: +49-711 351456-0; Fax: +49-711 351456-99.
e-mail: mail@schweizerbart.de, Internet: http://www.schweizerbart.de
Bernhard Harzer Verlag GmbH, Westmarkstraße 59/59a, 76227 Karlsruhe, Germany, Tel.: +49-721 944020, Fax: +49-721 9440230, e-mail: Info@harzer.de, Internet: www.harzer.de
Printed in Germany by Tutte Druckerei GmbH, 94121 Salzweg bei Passau, Germany.

# PFG – Jahrgang 2013, Heft 1
# Inhaltsverzeichnis

## Originalbeiträge



## Beitrag aus Wissenschaft und Praxis



## Mitteilungen



Zusammenfassungen der „Originalbeiträge“ und der „Beiträge aus Wissenschaft und Praxis“ (deutsch und englisch) sind auch verfügbar unter www.dgpf.de/neu/pfg/ausgaben.htm

PFG 2013 / 1, 005 – 0017
Stuttgart, February 2013

Article

# Neural Network Modelling of Tehran Land Subsidence Measured by Persistent Scatterer Interferometry

Maryam Dehghani, Shiraz, Iran, Mohammad Javad Valadan Zoej & Iman Entezam, Tehran, Iran

**Keywords:** persistent scatterer, neural network, modelling, sensitivity analysis

**Summary:** A large area located in the southwest of Tehran is subject to land subsidence induced by over-exploitation of groundwater. Since the use of conventional SAR Interferometry was not possible due to the large spatial baseline and rapid temporal decorrelation, persistent scatterer interferometry (PS-InSAR) using two different ascending and descending datasets of ENVISAT ASAR was applied in order to monitor the deformation. PS-InSAR is a recently developed technique used to address the decorrelation problem by identifying scatterers, called persistent scatterers (PS), the echo of which varies little in time. The estimation of the deformation rate was thus possible only in the PS pixels. In order to retrieve the spatial pattern of the subsidence, deformation rate at non-PS pixels were estimated by a proposed neural network modelling method separately applied on both descending and ascending datasets. Input variables of the network are geology and hydrogeology parameters of the aquifer system, while the network output is the subsidence rate. The performance of the neural network trained by the PS pixels was tested on a separate validation data. It was found that the trained network is able to predict the subsidence rate with the accuracy of less than 5 mm/a. The results were then compared to the levelling measurements acquired over a different time interval. The root-mean-square error (RMSE) between the measurements and the modelled deformation rate across the leveling tracks is 19.8 mm/a. The different deformation rates of both datasets in some points were most likely due to the different time intervals covered by the radar and levelling data. Neural network-based sensitivity analysis was finally performed to evaluate the influences of different geology and hydrogeology factors on the subsidence. The sensitivity analysis results that were interestingly similar for both radar datasets showed that the hydraulic conductivity, the thickness of fine-grained sediments and the water level decline are the first three most effective factors on the subsidence occurrence in Tehran basin.

**Zusammenfassung:** *Neuronales Netz zur Modellierung von Bodensenkungen bei Teheran gemessen durch Persistent Scatterer Interferometry.* Ein großes Gebiet südwestlich von Teheran ist von Bodensenkungen wegen übermäßiger Grundwasserentnahme betroffen. Die vorliegende Untersuchung baut auf zwei Datensätzen von ENVISAT ASAR auf, einem in Nord- und einem in Südrichtung geflogenen. Früher war der Einsatz von SAR Interferometrie wegen langer Basen und zu schneller zeitlicher Veränderungen am Objekt nicht möglich. Die neue Persistent Scatterer Methode (PS-InSAR) nutzt Objekte, deren Reflexionscharakteristik nur einer geringen zeitlichen Variabilität unterliegt. Allerdings kann die Deformation nur an ausgewählten, den so genannten PS-Pixeln bestimmt werden. Die dazwischenliegenden Räume wurden in dieser Untersuchung durch neuronale Netze überbrückt, die geologische und hydrogeologische Parameter berücksichtigen. Die innere Genauigkeit der Methode wurde durch unterschiedliche Trainingsdatensätze überprüft und ergab eine Genauigkeit der Prognose des Senkungsbetrages von weniger als 5 mm/a. Die äußere Genauigkeit wurde durch Nivellement bestimmt und ergab einen RMS-Fehler entlang der Nivellementslinien von 19,8 mm/a. Die große Abweichung dürfte auf unterschiedliche Zeitintervalle zwischen der SAR-Datenerfassung und den Nivellements beruhen. Die neuronalen Netze wurden außerdem zur Bewertung des Einflusses von geologischen und hydrogeologischen Parametern auf die Senkungsraten eingesetzt. Als die drei wichtigsten Einflussfaktoren haben sich die hydraulische Leitfähigkeit des Untergrundes, die Mächtigkeit der feinkörnigen Sedimente und der Rückgang des Grundwasserspiegels gezeigt. Beide SAR-Datensätze führten zum gleichen Ergebnis.


www.schweizerbart.de
DOI: 10.1127/1432-8364/2013/0154
1432-8364/13/0154 $ 3.25

## 1 Introduction

Excessive groundwater pumping causes an increasing effective stress in aquifer systems. The changes in the effective stress cause some degree of compaction in fine-grained sediments within the aquifer system resulting in land subsidence. The land subsidence induced by overexploitation of groundwater is one of the major problems with its environmental consequences in most parts of Iran. One of these areas is located in the southwest of Tehran, the capital city of Iran. The Tehran Basin with an area of 2250 km$^2$ is located between the Alborz Mountains to the north and Arad and Fashapouye Mountains to the south.

The National Cartographic Center (NCC) of Iran firstly measured the land subsidence by precision levelling during 1995–2002. Later, the Geological Survey of Iran (GSI) in cooperation with other organizations including NCC and the Water Management Organization launched a comprehensive study on subsidence in and around Tehran. The area was studied from different points of view including geology, geophysics, tectonic and geotechnics. According to the geological map (1:100,000 scale), the Tehran Basin consists of different geological units including lower-middle Eocene (Karaj formation) and Quaternary units. The southern part of the area primarily contains Quaternary (Qt1 and Qt2) units as indicated in Fig. 1b. The Qt1, or Kahrizak formation, features different properties in the northern and southern parts of the area, consists of silt and cream clay in the subsidence area, and is exposed by different faults such as the Kahrizak, south Rey and North Rey faults (Fig. 1a). The deposit of fine-grained sediments due to flooding generates the clay silt of Kahrizak. The Qt2, or Tehran formation, contains young alluvial fans mainly covering the southern part of the Tehran Basin. This formation has an unsorted alluvial and a flood deposit with an average thickness of 60 m, primarily composed of gravel, pebble and sand in a sandy silt matrix (Shemshaki et al. 2005).

The extent and thickness of the fine-grained sediments serves as one of the most important factors for land subsidence caused by groundwater extraction. The greater extent and thickness an aquifer system has, the more compaction occurs. According to the studies performed by the Engineering Geology group of the Geological Survey of Iran (GSI), the thickest part of the alluvial layers that constitute the aquifer system belongs to the area with a higher subsidence rate. The contours indicating the alluvial thickness are illustrated in Fig. 4e. Moreover, the central part of the subsidence

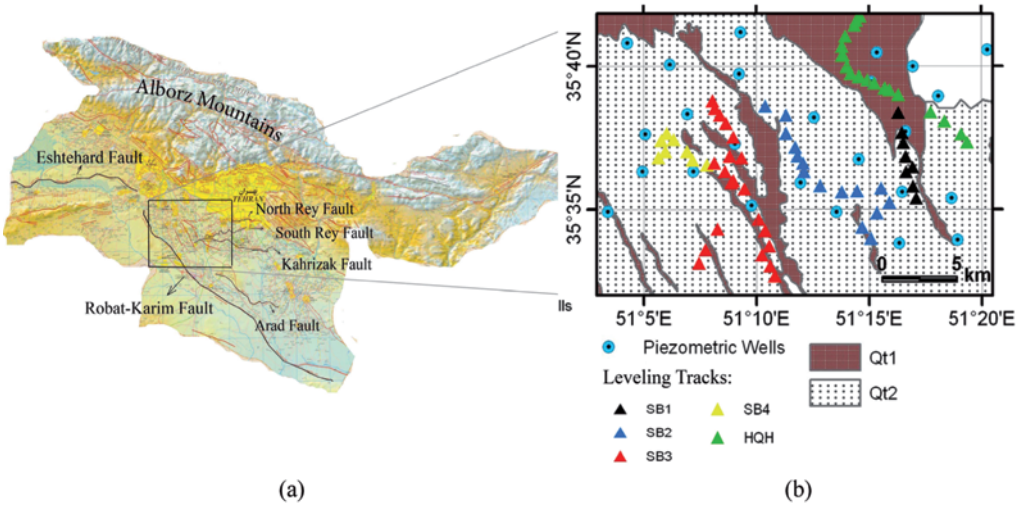


**Fig. 1:** (a) Location of different faults surrounding the study area in Tehran province. The black rectangle depicts the area subject to subsidence. (b) Geological units mainly consisting of Quaternary sediments. The blue circles represent piezometric wells while the black triangles indicate the levelling stations.

area contains higher amounts of fine-grained sediments, including clay, at up to 100% as observed in Fig. 4f. Moreover, geotechnical tests indicate that the storage coefficient have smaller values in the southern part of the aquifer system compared to the northern part (Fig. 4c). The decrease of the storage coefficient is due to the existence of higher amounts of fine-grained sediments in the aquifer system. The average value of the storage coefficient of Tehran aquifer system is estimated as 5% (Shemshaki et al. 2005). Moreover, as shown in Fig. 4d, the hydraulic conductivity of the aquifer system decreases generally from north to south of the area and in the northeast of the area. The decrease of the hydraulic conductivity in the northeast is mostly due to the decrease of thickness of the saturated zone.

The main part of the Tehran basin dedicated to the agricultural activities is subject to the land subsidence due to the over-exploitation of groundwater. According to the latest studies, groundwater level depth exceeds 100 m in the north of the aquifer system (Fig. 4b). A unit hydrograph of the Tehran basin (Fig. 2) indicating the overall changes of water level was extracted from the piezometric information (Shemshaki et al. 2005). The locations of piezometric wells are shown in Fig. 1b. As observed in Fig. 2, the water level dramatically declined by about 9 m in 20 years. The volume change of the aquifer system during 10 years is estimated as 6.6 km$^3$. The number of pumping wells has increased from 3906 in 1969 to 26076 in 2003. A comparison of the number of wells and the volume of the extracted water between 1968 and 2003 shows that the ability of the aquifer system to yield water has significantly decreased due to insufficient recharge. The water level changes between 1968 and 2003 are shown as contour lines in Fig. 4a.

Among the various ground- and space-based techniques available, interferometric Synthetic Aperture Radar (InSAR) provides precise measurements of land surface deformation over large areas and at high spatial resolution (Galloway et al. 1998, Amelung et al. 1999, Peltzer et al. 1998, Fruneau & Sarti 2000, Tesauro et al. 2000, Crosetto et al. 2002, Motagh et al. 2006). However, conventional interferometry fails when the ground surface is covered by significant amounts of vegetation, due to a loss of correlation (Galloway & Hoffmann 2007) as in Tehran basin. Persistent scatterer InSAR (PS-InSAR) is a recently developed technique used to address the decorrelation problem by identifying scatterers, called persistent scatterers (PS), the echo of which varies little in time (Ferretti et al. 2000, Hooper et al. 2004, Kampes 2005). PS-InSAR gives measurements at a few sparse locations, i.e. PS points. However, despite of the improvement due to PS-InSAR approaches it should be noted that, if the spatial density of the detected persistent scatterers is low, the deformation pattern cannot be reliably retrieved. A sufficient number of PS pixels is required to map local variation of the deformation for deeper understanding of the subsidence extent and spatial distribution that enables us to better manage the water resources and construction tasks. It is however impor-

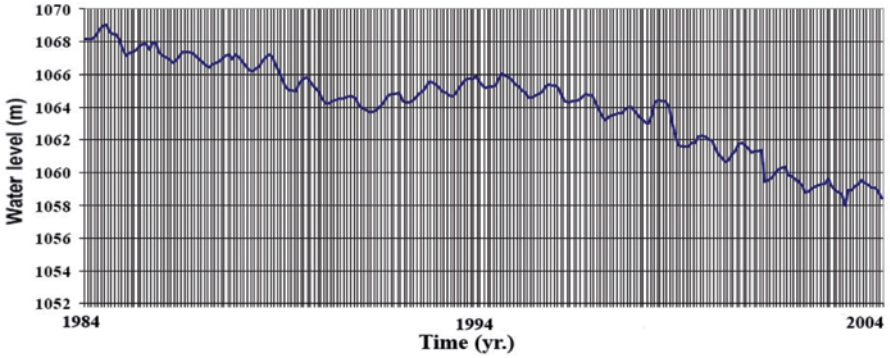


**Fig. 2:** Unit hydrograph for the Tehran aquifer system extracted from the groundwater information (Shemshaki et al. 2005).

tant to have the subsidence spatial extent and pattern for land managements (González & Fernández 2011). As in the Tehran basin many agricultural fields exist, the persistent scatterer density is low due to the lack of coherent scatterers over the time interval of consideration. There are various algorithms to retrieve the spatial pattern of the subsidence using the values at PS pixels. Classic interpolation techniques such as kriging can be generally used to estimate the deformation at a non-persistent scatterer based on the known deformation of surrounding persistent scatterers. However, these methods are based only on the deformation values of the neighbouring pixels. There are some analytical methods that try to predict the aquifer compaction using the geology and hydrogeology information (Hoffmann et al. 2003). However, we are left with great errors using these methods when we are facing the lack of accurate and detailed information of the aquifer system.

In such cases, the methods based on the intelligence systems can be effectively used instead of modelling the subsidence. In this paper we present a method based on a back-propagation neural network in order to model the subsidence signal. The deformation at non-persistent scatterer is estimated by neural network interpolation using not only the PS-InSAR derived deformation of the persistent scatterers but also their hydrogeology properties that highly affects the subsidence. The constructed neural network is trained using the hydrogeology parameters of the aquifer system as input variables of the network and PS-InSAR derived subsidence rate at PS pixels as the network output. The PS pixels whose deformation could be measured by PS-InSAR are used to train the network. The trained neural network is then used: (i) to retrieve the spatial pattern of the subsidence or to estimate the subsidence rate at non-PS pixels and to (ii) perform sensitivity analysis to identify a hydrogeology factor with the most influence on the subsidence. In other words, we can recognize to which hydrogeology factor the subsidence in Tehran basin is most sensitive.

This paper is structured as follows: Section 2 presents the proposed modelling method based on neural network and the mathematical framework of the sensitivity analysis. In section 3, the information layers fed to the neural network and the obtained results will be presented. Moreover, the sensitivity analysis results are given in this section. Finally, concluding remarks are given in section 4.

## 2 Subsidence Modelling based on Neural Network

Neural networks are based on the structure and functioning of the human brain and consist of a large number of simple processing units known as neurons. The neural network function is determined largely by the connections between neurons. It is trained by adjusting the values of the connections (weights) between neurons so that a particular input leads to a specific target output. The network is adjusted based on a comparison of the output and the target until the network output matches the target.

The output signal of neuron $k$ in layer $l$ is calculated as follows:

$$y^{(l)_k} = s^{(l)_0}\left(w^{(l-1)_{k1}} \cdot y^{(l-1)_1} + \ldots + w^{(l-1)_{kK_{l-1}}} \cdot y^{(l-1)_{K_{l-1}}} + w^{(l-1)_{k0}}\right) \quad 1 \le k \le K_l \tag{1}$$

Where $K_l$ is the number of neurons in layer $l$, $s^{(l)_0}(.)$ is the activation function, $w^{(l-1)_{ki}}$ is the weight of the input $y^{(l-1)_{ki}}$ to the neuron k in which $1 \le i \le K_{l-1}$ and $w^{(0)_{k0}}$ is the bias value corresponding to the neuron $k$. It should be noted that $y^{(l-1)_{ki}}$ is actually the output of $i$th neuron in the previous layer. If $l = 1$, $y^{(l-1)_{ki}}$ is the input variables to the neural network. Weights are updated using the mean-squared error (MSE) as cost or error function through the training process. Readers are referred to e.g. Haykin et al. (1995) for further information about the training process and updating the weights.

One of the important factors that affect the success of modelling procedure is the ability to extract information about the relationships between the model structure's inputs and outputs from the trained neural network (Hashem 1992). This information can be used as a basis for the analysis of the model and determination of the most significant factors that affect

it. HASHEM (1992) presented a closed-form expression for first order as well as higher order output sensitivities w.r.t. variations in the input variables for multilayer feedforward neural networks. These sensitivities can be used as a basis for inference about input-output relationships. In order to estimate the sensitivity of the network output w.r.t. to its inputs, the partial derivative, $\frac{\partial y}{\partial x_i}$ is estimated where y is the network output and $x_i$ is its *i*th input. Consider a neural network with 2 hidden layers consisting of $K_1$ and $K_2$ neurons. $\frac{\partial y}{\partial x_i}$ is then calculated as follows:

$$\frac{\partial \hat{y}}{\partial x_i} = \sum_{k_2=1}^{K_2} \frac{\partial \hat{y}}{\partial y^{(2)_{k_2}}} \cdot \frac{\partial y^{(2)_{k_2}}}{\partial y^{(1)}} \cdot \frac{\partial y^{(1)}}{\partial x_i} \quad i = 1,...,n \quad (2)$$

Where $n$ is the number of input variables, $\hat{y}$ is the network output, and $y^{(1)}$ and $y^{(2)}$ are the outputs of the first and second hidden layer, respectively. $x_i$ is its *i*th input. The updated weights from training step are used to calculate (2). The more sensitive the output w.r.t. to $x_i$ is, the higher the $\frac{\partial y}{\partial x_i}$ is. A little change to $x_i$ will then cause a great change to the output $\hat{y}$.

Subsidence due to the over-exploitation of groundwater is a complex procedure influenced by different geology and hydrogeology factors. Groundwater information collected at different piezometric wells in the Tehran basin showed that the water level decline is not the only important cause for the subsidence occurrence in this area (DEHGHANI et al. 2010). Instead, some other geology and hydrogeology factors such as the fine-grained sediments thickness in the aquifer system are controlling the subsidence rate. In this paper, a method based on neural network is presented to model the subsidence for areas in which we could not measure the deformation rate using PS-InSAR. Moreover, in order to identify the main

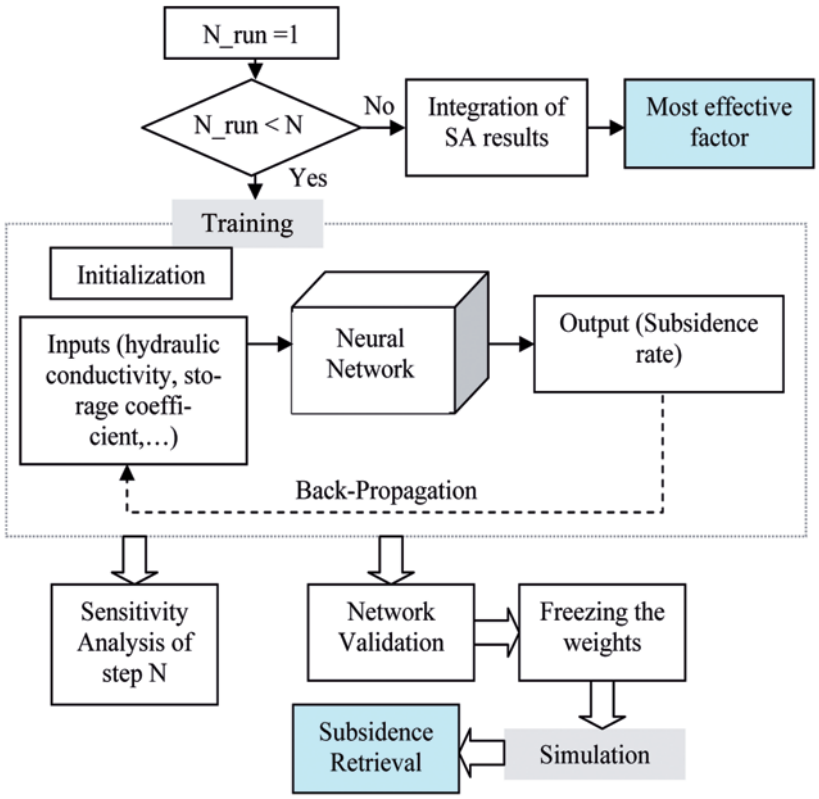


**Fig. 3:** Framework of the presented method for modelling the subsidence and sensitivity analysis.

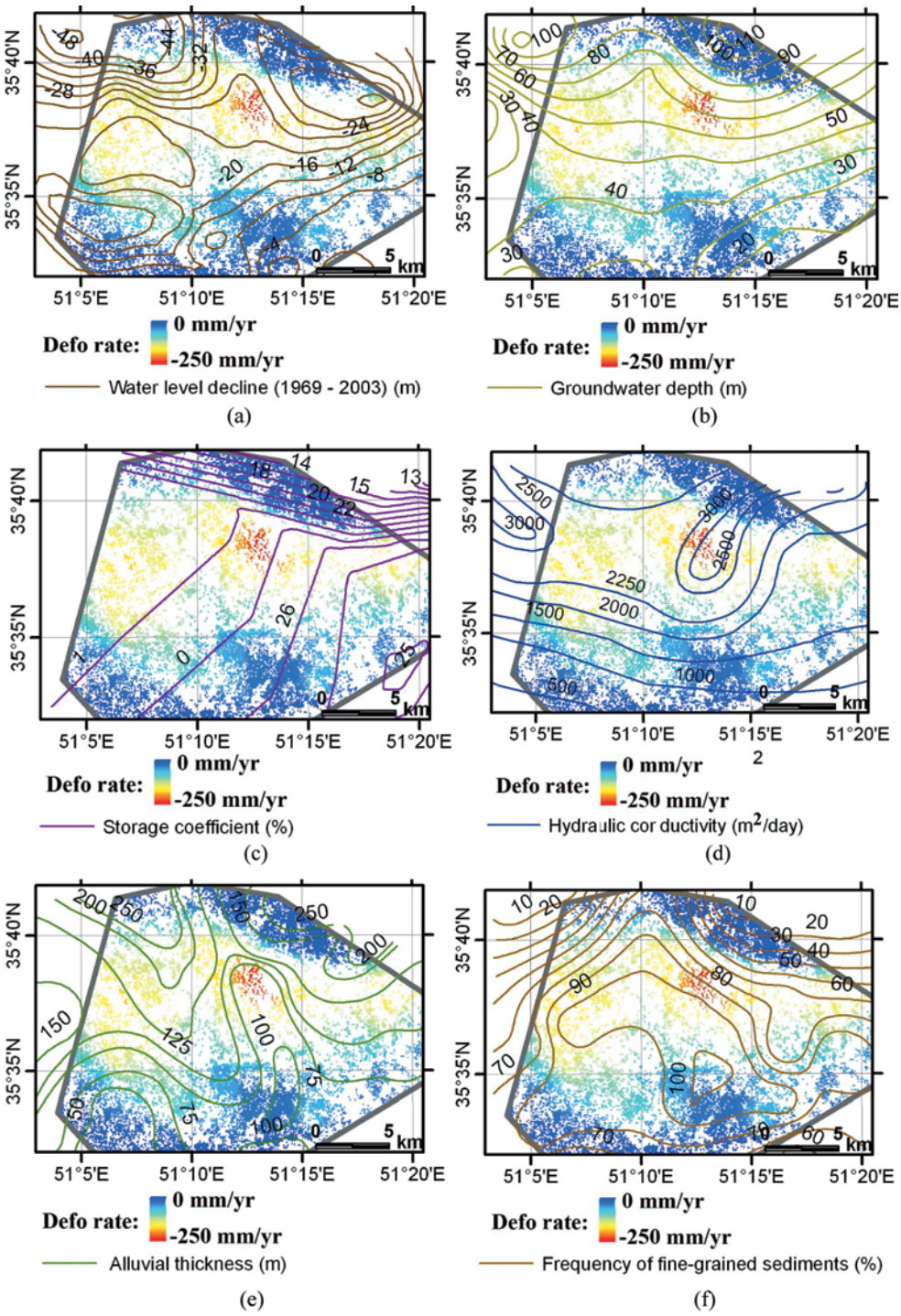


**Fig. 4:** Network inputs and output: (a) water level decline between 1969 and 2003, (b) groundwater depth, (c) storage coefficient, (d) hydraulic conductivity, (e) alluvial thickness, (f) frequency of fine-grained sediments in terms of percentage.

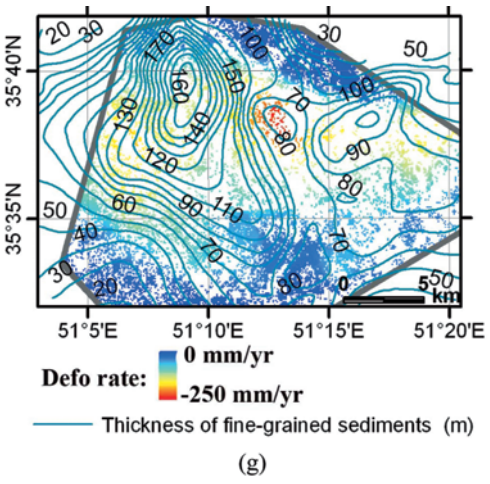


**Fig. 4:** Network inputs and output: (g) thickness of fine-grained sediments.

controlling factors in the Tehran basin subsidence, the sensitivity analysis was performed using the trained network. The framework of the presented method for subsidence modelling and sensitivity analysis is illustrated in Fig. 3.

The first step in the network construction is to determine the number of layers and their neurons as well as the activation functions. The most proper network architecture here was identified in a trial-and-error manner. As the network initialization for training is randomly done, the obtained results including the updated weights and the sensitivity analysis result are slightly different in each run. It should be noted that each run includes a complete training procedure. The criterion for stopping the training procedure in each run is the number of iterations. According to Fig. 3 a neural network is fully trained in N independent runs where N can be arbitrarily set. The trained network is tested at the end of each run using the validation data. Moreover, the sensitivity analysis result obtained in each run will be saved for further integration. The updated weights corresponding to the minimum overall network error are used for the final simulation step.

The network input variables are hydrogeology factors controlling the subsidence rate while the output is the subsidence rate at PS pixels derived from PS-InSAR. The Tehran basin subsidence was monitored using PS-InSAR technique by which the annual deformation rate was measured at persistent scatterer locations. The available radar data consisted of 22 descending ENVISAT ASAR images of track 149 acquired between 2003 and 2008 and 19 ascending ENVISAT ASAR images of track 414 spanning between 2004 and 2009. PS-InSAR method was separately applied on both ascending and descending radar data. The results obtained from PS-InSAR indicate that the deformation time series contained a significant linear component on which the insignificant seasonal fluctuations are superimposed (Dehghani et al. 2010, Dehghani et al. 2009). The PS-InSAR results were then used to extract the annual deformation rate that is assumed to be constant from 2003 to 2009 as deformation time series suggested. The estimated subsidence rates obtained from descending and ascending data are slightly different due to the different imaging geometries of both datasets and non pure vertical components of the deformation system (Samieie-Esfahany et al. 2009).

The number of PS pixels detected from ascending and descending data is around 400,000 and 800,000, respectively. Due to the low spatial density of PS pixels, the deformation pattern cannot be easily recognized in the area. Hence, the presented modelling method is used to estimate the deformation rate at non-persistent scatterers in order to retrieve the deformation pattern. About 60% of the detected persistent scatterers are used to train the network while the rest is applied for network validation. The introduction of the inputs and output of the network as well as the obtained results from the modelling are presented in the next section.

## 3 Results

The available hydrogeology information of the Tehran basin includes hydraulic conductivity, storage coefficient, frequency and thickness of fine-grained sediments, groundwater depth, amount of water level decline between 1969 and 2003 extracted from piezometric measurements and alluvial thickness of the Tehran aquifer system. These proper-

ties were measured at different measurement sites across the study area using various methods including geotechnical testing and geophysics approaches. The point measurements were then converted to contour lines using interpolation. All the information layers superimposed as contours on the deformation rate map of PS pixels are shown in Fig. 4 as already explained.

In order to make the hydrogeology data compatible with the PS-InSAR-derived subsidence data in the neural network, all data were interpolated into grids with the pixel size of 90 m. Therefore, the total number of 320 × 210 pixels for which there are 7 features, i.e. hydrogeology information, covered the study area. A network consisting of two hidden layers of 20 and 5 neurons with the tangent sigmoid activation function was constructed. The hydrogeology information at PS pixels and their derived deformation rate were used as the network input and output, respectively. The constructed network was trained using 60% of the detected PS pixels. As already noted, the network was constructed in $N$ runs ($N$ is here set to 50) for each of which the trained network was tested using the validation data, i.e. 40% of the PS pixels. After comparing the results of different runs, the weights corresponding to the minimum overall network error are used for final simulation step.

The correlation between the trained network output and the observed subsidence rate for training and validation pixels in both ascending and descending datasets is illustrated in Fig. 5.

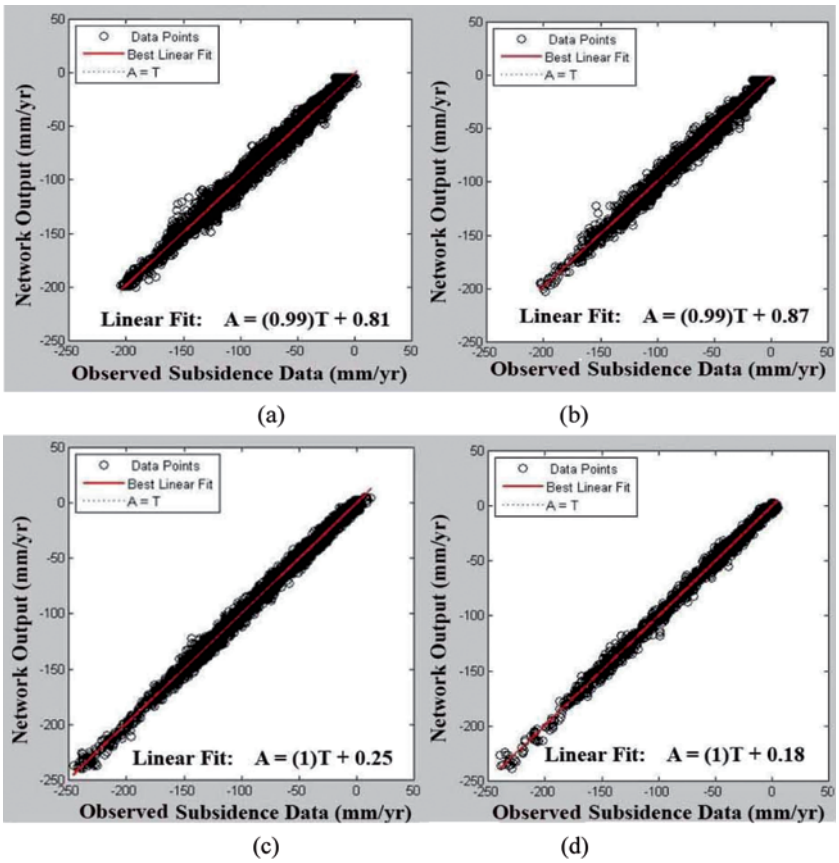


**Fig. 5:** Correlation between the subsidence rate simulated from the trained network (y axis) and the observed one derived from the PS-InSAR (x axis) for different datasets: (a-b) training and validation data of the descending mode, and (c-d) training and validation data of the ascending mode.

As can be observed in Fig. 5, a high correlation exits between the simulated subsidence data and the observed one extracted from PS-InSAR. The linear regression equation for each dataset presented below its corresponding plot is significantly close to $A=T$ where $A$ and $T$ is the simulated and observed deformation values, respectively. In order to better validate the performance of the model, the subsidence rate at all PS pixels (training and validation pixels) for which the observed subsidence rate is available from PS-InSAR is simulated by the trained network as shown in Fig. 6. In this figure, the observed and simulated subsidence rates for both datasets are illustrated. Furthermore, the residual map as the

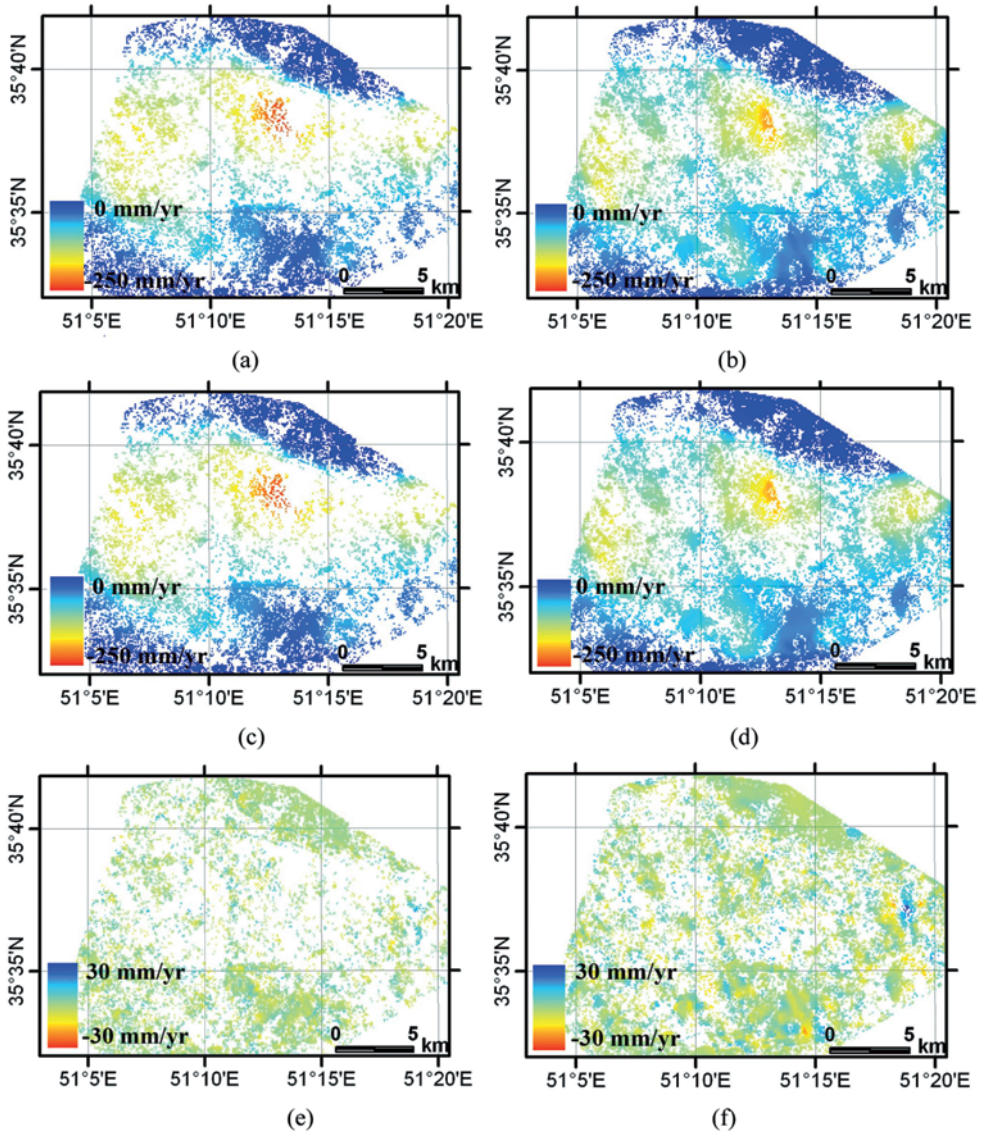


**Fig. 6:** Observed deformation rate obtained from the (a) descending and (b) ascending data; simulated deformation rate using the (c) descending and (d) ascending data; residual map as the difference between the observed deformation rate and the simulated one using the (e) descending and (f) ascending data.

difference between the observed and modelled subsidence rate is presented in Figs. 6c and 6f. Accordingly, the most amount of subsidence could be simulated by the proposed model and the residual map has a noisy behaviour rather than a systematic one. The root-mean-square error (RMSE) of the residual map is estimated as 3.53 mm and 4.58 mm for the descending and ascending datasets, respectively. The low values of RMSE are an indication of the high performance for the subsidence modelling.

The subsidence rate for all pixels (PS and non-PS) in the study area was then simulated by the trained network (Fig. 7).

As shown in Fig. 7, the spatial subsidence pattern including 3 main lobes has been retrieved. The slight difference observed between the spatial subsidence patterns simulated from descending and ascending modes is related to their different imaging geometry. The maximum deformation rates estimated from descending and ascending datasets are 241 mm/a and 203 mm/a, respectively. The coincidence of the spatial pattern of the subsidence area with the cultivated area indicates that the subsidence in the Tehran basin is due to groundwater exploitation. The spatial profiles across the deformation show that the subsidence follows a "v" type pattern.

The results obtained from the proposed method were compared to the levelling data collected by NCC in two periods, 2004 and 2005 (Arabi et al. 2008). The available levelling data consists of five levelling tracks, SB1, SB2, SB3, SB4 and HQH as illustrated in Fig. 1 in different colours. The deformation rates at levelling stations are estimated from the trained neural network and then compared

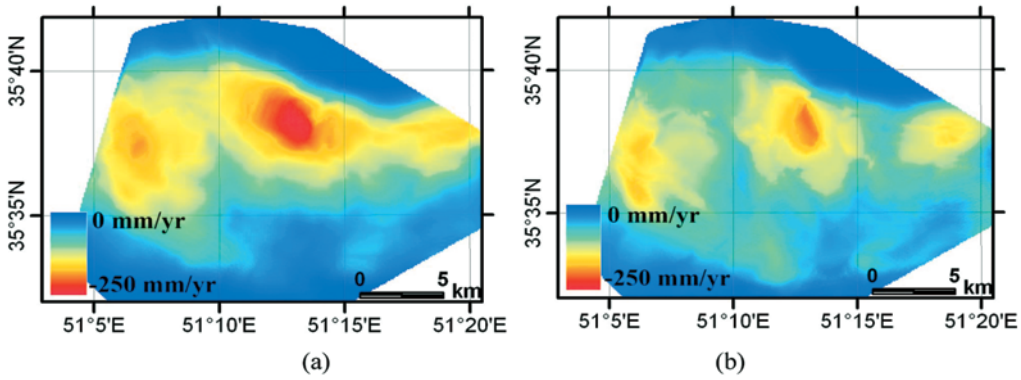


**Fig. 7:** Subsidence rate simulated from the proposed method applied on (a) descending dataset and (b) ascending dataset.

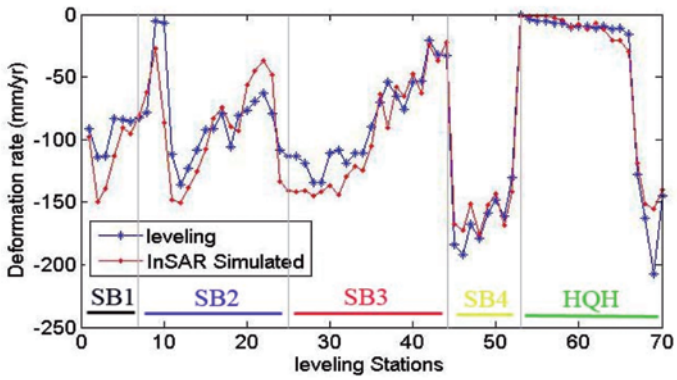


**Fig. 8:** Comparison of subsidence rate inferred from the proposed method (red lines) and levelling (blue lines) across different levelling tracks SB1, SB2, SB3, SB4 and HQH.

to the values measured by levelling. The comparison between levelling measurements and the vertically-converted subsidence rate estimated from the proposed method is shown in Fig. 8. The overall RMSE between levelling measurements and the vertically-converted subsidence rate extracted from the proposed method is estimated as 19.8 mm/a.

The different deformation rate of both datasets is most likely due to the different time intervals covered by the radar data (2004 and 2008) and levelling measurements (2004 and 2005), though the spatial distribution of the rates from levelling is consistent with that derived from the proposed method.

According to the diagram of Fig. 3, in order to study the effect of each input variables on the subsidence the sensitivity analysis is performed at the end of each run for all pixels. In each run, the sensitivity of the subsidence to different input variables (7 factors in here) is calculated for each pixel using the updated weights (2). The calculated sensitivities are then sorted based on their values indicating the significance order of the input variables affected by the subsidence rate. The maximum value is corresponding to the most effective factor. Finally, the sensitivity analysis outcomes of all 50 runs are integrated to obtain more reliable results. The final result is presented as a histogram showing the number of pixels for which one factor is indicated as the most effective one (Fig. 9). For example, according to Fig. 9 in about 3500 pixels the most effective factor on the subsidence occurrence is the hydraulic conductivity (#1). In fact, the effectiveness of a factor is determined by the number of pixels in which that factor is the most effective one. According to Figs. 9a and 9b, the subsidence has the most sensitivity to the hydraulic conductivity, thickness of fine-grained sediments and water level decline.

A considerable fact is that the sensitivity analysis results separately obtained from the descending and ascending data are highly comparable. The significance orders extracted from both datasets are exactly similar. This may indicate the correctness of the generated model.

## 4 Conclusions

Studying the land subsidence first requires measuring the magnitude of the deformation caused by this phenomenon. Analysis of the temporal and spatial behaviour of the deformation caused by subsidence allows us to mitigate its devastating effects and manage water resources. PS-InSAR is a method recently developed to measure the deformation in an area suffering from temporal and spatial

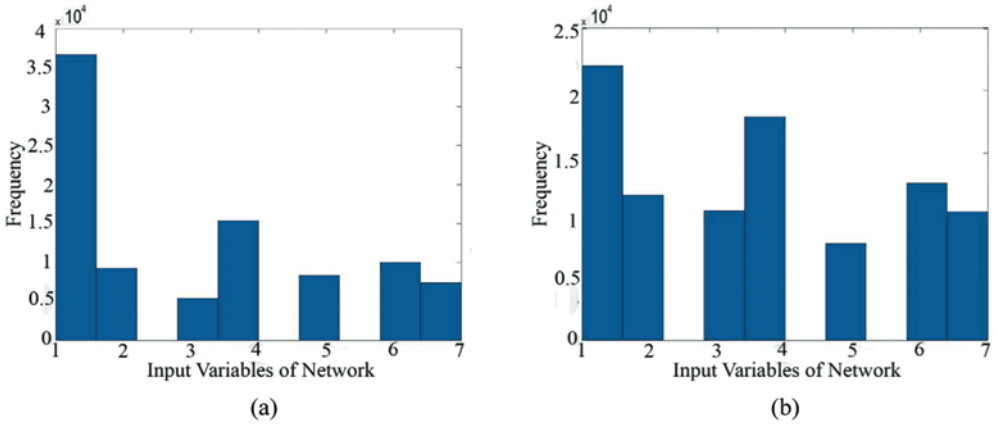


**Fig. 9:** Histograms of the sensitivity analysis results obtained from (a) descending data and (b) ascending data. The X-axis indicates the input variables (#1: hydraulic conductivity, #2: storage coefficient, #3: frequency of fine-grained sediments, #4: thickness of fine-grained sediments, #5: groundwater depth, #6: amount of water level decline and #7: alluvial thickness). Y-axis represents for the number of pixels.

decorrelation. However, this technique is able to measure the deformation at only PS pixels, the backscattering of which varies little in time. The subsidence estimation from PS-InSAR does not show local variations when the spatial density measurement points decreases which is mostly the case due to the occurrence of the subsidence in the rural areas. It is, on the other hand, critical to know about the local variations of the deformation particularly for the construction purposes. In this paper we presented an algorithm based on a neural network to estimate the subsidence rate in the non-PS pixels in which we were not able to directly measure the deformation by PS-InSAR method. Hydrogeology properties of the aquifer system were used as input variables of the network while the subsidence rate is taken as the network output. The PS pixels for which the subsidence rate is known from the PS-InSAR measurements were used to train and validate the network. The trained network was then applied to simulate the subsidence rate at all pixels (PS and non-PS pixels). This leads to retrieve the subsidence spatial pattern in the Tehran basin. The coincidence of the spatial pattern of the subsidence area with the cultivated area indicates that the subsidence in Tehran basin is due to groundwater exploitation. The maximum deformation rates estimated from descending and ascending datasets are 241 mm/a and 203 mm/a, respectively. The spatial profiles across the deformation area indicate that the subsidence follows a "v" type pattern. The results were then compared to the levelling measurements. The comparison showed that the deformation rates predicted at the levelling stations broadly agrees with the levelling measurements. The RMSE of 19.8 mm/a is most likely due to the different time intervals covered by the radar data (2004 and 2008) and levelling measurements (2004 and 2005), though the spatial distribution of the rates from levelling is consistent with that derived from the proposed method.

The sensitivity of the subsidence to different input parameters was finally investigated using the updated weights obtained in the training process. We found that the Tehran subsidence is mostly sensitive to the hydraulic conductivity, thickness of fine-grained sediments and water level decline.

## Acknowledgements

We wish to thank the European Space Agency (ESA) for providing ENVISAT ASAR data. We convey our sincere gratitude to the Geological Survey of Iran for providing the hydrogeological information. The authors wish to thank the Delft University of Technology for all their kind scientific supports for persistent scatterer interferometry.

## References

Amelung, F., Galloway, D.L., Bell, J.W., Zebker, H.A. & Laczniak, R.L., 1999: Sensing the ups and downs of Las Vegas – InSAR reveals structural control of land subsidence and aquifer-system deformation. – Geology **27** (6): 483–486.

Arabi, S., Maleki, E. & Talebi, A. 2008: Report of land subsidence in south-west of Tehran. – National Cartographic Center of Iran, national scientific report.

Crosetto, M., Tscherning, C.C., Crippa, B. & Castillo, M., 2002: Subsidence monitoring using SAR interferometry: reduction of the atmospheric effects using stochastic filtering. – Geophysical Research Letters **29** (9): 26.1–26.4.

Dehghani, M., Hooper, A., Hanssen, R., Valadan Zoej, M.J., Saatchi, S. & Entezam, I., 2009: Hybrid conventional and Persistent Scatterers SAR Interferometry for Land Subsidence Monitoring in southwest Tehran, Iran. – Fringe Workshop 2009, Italy.

Dehghani, M., Valadan Zouj, M.J., Entezam, I., Saatchi, S. & Shemshaki, A., 2010: Interferometric Measurements of Ground Surface Subsidence induced by Overexploitation of Groundwater. – Journal of Applied Remote Sensing **37** (1): 147–156.

Ferretti, A., Prati, C. & Rocca, F., 2000: Nonlinear subsidence rate estimation using Permanent Scatterers in Differential SAR Interferometry. – IEEE Transactions on Geoscience & Remote Sensing **38** (5): 2202–2212.

Fruneau, B. & Sarti, F., 2000: Detection of ground subsidence in the city of Paris using radar interferometry: isolation from atmospheric artifacts using correlation. – Geophysical Research Letters **27** (24): 3981–3984.

Galloway, D.L., Hudnut, K.W., Ingebritsen, S.E., Phillips, S.P., Peltzer, G., Rogez, F. & Rosen, P.A., 1998: Detection of aquifer system compaction and land subsidence using interferometric synthetic aperture radar, Antelope Valley, Mo-

jave Desert, California. – Water Resources Research **34** (10): 2573–2585.

Galloway, D.L. & Hoffmann, J., 2007: The application of satellite differential SAR interferometry-derived ground displacements in hydrogeology. – Hydrogeology Journal **15:** 133–154.

González, P.J. & Fernández, I., 2011: Drought-driven transient aquifer compaction imaged using multitemporal satellite radar interferometry. – Geology **39:** 551–554.

Hashem, S., 1992: Sensitivity analysis for feedforward Artificial Neural Networks with differentiable activation functions. – 1992 International Joint Conferences on Neural Networks, IEEE Press **1:** 419–424, Baltimore, MD, USA.

Haykin, S.S., Haykin, S. & Van Veen, B., 1995: Neural Network: a Comprehensive Foundation, IEEE Version.

Hoffmann, J., Leake, S.A., Galloway, D.L. & Wilson, A.M., 2003: MODFLOW-2000 groundwater model – user guide to the subsidence and aquifer-system compaction (SUB) package. – U.S. Geological Survey Open-File Report **03-233**.

Hooper, A., Zebker, H., Segall, P. & Kampes, B., 2004: A new method for measuring deformation on volcanoes and other natural terrains using InSAR persistent scatterers. – Geophysical Research Letters **31:** 611–615.

Kampes, B.M., 2005: Displacements Parameter Estimation using Permanent Scatterer Interferometry. – Ph.D. thesis, Delft University of Technology.

Motagh, M., Djamour, Y., Walter, T.R., Wetzel, H.U., Zschau, J. & Arabi, S., 2006: Land subsidence in Mashhad Valley, northeast Iran: results from InSAR, levelling and GPS. – Geophysical Journal International **168**, doi: 10.1111/j.1365–246X.2006.03246.x.

Peltzer, G., Rosen, P., Rogez, F. & Hudnut, K., 1998: Poro-elastic rebound along the Landers 1992 earthquake surface rupture. – Journal of Geophysical Research **103:** 30.131–30.145.

Samieie-Esfahany, S., Hanssen, R.F., Thienen-Visser, K.V. & Muntendam-Bos, A., 2009: On the Effect of horizontal Deformation on InSAR Subsidence Estimates. – Fringe Workshop 2009, Italy.

Shemshaki, A., Blourchi, M.J. & Ansari, F.M., 2005: Earth subsidence review at Tehran plain-Shahriar (first report). – Report No: Engeo84-06/02, http://gsi.ir/General/Lang_en/Page_27/GroupId_01-01/TypeId_All/Start_20/Action_ListView/WebsiteId_13/3.html (30.10.2012).

Tesauro, M., Beradino, P., Lanari, R., SansoSti, E., Fornaro, G. & Franceschetti, G., 2000: Urban subsidence inside the City of Napoli (Italy) observed with synthetic aperture radar interferometry at Campi Flegrei caldera. – Journal of Geophysical Research **27:** 1961–1964.

Addresses of the authors:

Dr. Maryam Dehghani, Assistant Professor, Dept. of Civil and Environmental Engineering, School of Engineering, Shiraz University, Zand St., Shiraz, Iran, Tel.: +98-711-6133162, Fax: +98-711-6473161, e-mail: dehghani_rsgsi@yahoo.com

Dr. Mohammad Javad Valadan Zoej, Associate Professor, Faculty of Geodesy and Geomatics Engineering, K. N. Toosi University of Technology, Tehran, Iran, Tel.: +98-21-88770218, e-mail: valadanzouj@kntu.ac.ir.

Dr. Iman Entezam, Engineering Geology Group, Geological Survey of Iran (GSI), Tehran, Iran, Tel.: +98-21-64592228, e-mail: dr.entezam@gmail.com

Manuskript eingereicht: Mai 2012
Angenommen: September 2012

PFG 2013 / 1, 0019–0030
Stuttgart, February 2013

Article

# Performance Comparison of Contemporary Anomaly Detectors for Detecting Man-Made Objects in Hyperspectral Images

Safa Khazai, Abdolreza Safari, Barat Mojaradi & Saeid Homayouni, Tehran, Iran

**Keywords**: anomaly detection, hyperspectral images, man-made objects

**Summary:** Anomaly detection (AD) is an important and challenging area in hyperspectral image analysis. Based on different approaches, numerous AD algorithms have been presented and developed throughout the literature. This paper aims to compare detection performances of contemporary AD algorithms for detecting man-made objects in hyperspectral imagery. The algorithms used in this study include the segmented based Reed-Xiaoli (RX) algorithm, the principal component analysis based RX (PCA-RX), the orthogonal subspace projection based anomaly detector (OSP-AD), the kernel PCA-RX, and the kernel based one-class support vector machines. To evaluate the performance of the algorithms, three real hyperspectral datasets are employed. The performance comparison is then carried out on the basis of the receiving operative characteristics (ROC) curve and the average of false alarm rate (AFAR). Experimental results suggest that among the AD algorithms the OSP-AD is the most promising detector for detecting man-made targets.

**Zusammenfassung:** *Vergleich der Leistungsfähigkeit von modernen Anomaliedetektoren zur Erkennung von künstlichen Objekten in Hyperspektralbildern*. Die Erkennung von Anomalien in der Analyse von Hyperspektralbildern ist eine wichtige und anspruchsvolle Aufgabe. In der Literatur findet man viele Algorithmen zur Anomaliedetektion. Dieser Artikel vergleicht die modernen Detektoren hinsichtlich ihrer Leistungsfähigkeit zur Erkennung von künstlichen Objekten. Die Studie berücksichtigt den „Segmented Based Reed-Xiaoli (RX) Algorithmus", den auf der Hauptachsenanalyse basierenden Reed-Xiaoli (RX) Algorithmus (PCA-RX), den auf der „Orthogonal Subspace Projection" basierenden Anomaliedetektor (OSP-AD), den Kernel PCA-RX, and die „Kernel Based One-Class Support Vector Machines". Der Untersuchung lagen drei Hyperspektraldatensätze zu Grunde. Als Kenngrößen wurden die „Receiving Operative Characteristics (ROC) Curve" und die „Average of False Alarm Rate (AFAR)" gewählt. Nach unseren Ergebnissen dürfte der OSP-AD für die Erkennung von künstlichen Objekten am geeignetsten sein.

## 1 Introduction

Hyperspectral images in general consist of hundreds of narrow and contiguous spectral channels, from the visible to the shortwave infrared region of the electromagnetic spectrum. Such data have great potential to detect and identify earth surface objects and phenomena in a remotely sensed scene. When the signature of the target of interest is known, the target detection (TD) approach can be used. However, TD algorithms are dependent on the degree of signal mismatch between the spectral libraries and the spectra observed in an image. This is because of the difficulties to perform an accurate spectral calibration and to get reliable atmospheric data to convert reflectance values to the radiance spectra (Banerjee et al. 2006). Moreover, in many applications, the spectral signatures of the targets are often unknown. Hence, the anomaly detection (AD) approach can be used as an automatic TD system (Wilson 1998). AD algorithms enable one to detect targets whose signatures are spectrally distinct from their environment with no *a priori* knowledge other than that targets are rare, i.e. they have a low probability of occurrence in an image

 www.schweizerbart.de
DOI: 10.1127/1432-8364/2013/0155 1432-8364/13/0155 $ 3.00

scene (Reed & Yu 1990, Banerjee et al. 2006, Schweizer & Moura 2001).

The kind of anomalies to be detected depends on the specific application. They may vary from crop stress identification in precision agriculture and infected trees in forestry to rare minerals in geology and mining (Matteoli et al. 2010). In particular, man-made objects are the most common type of anomalies considered in the public safety domain, e.g. search and rescue operations, and reconnaissance and surveillance applications. Man-made objects are typically characterized by a spectral signature different from the signatures of their surroundings. Moreover, in contrast to natural anomalies, the sizes of man-made anomalies are usually known. Also, depending on the spatial resolution of the sensor, the man-made targets may not be clearly resolved; therefore, they cover only a few pixels, i.e. multipixel targets, or even less than a single pixel, i.e. subpixel targets (Matteoli et al. 2010).

The Reed-Xiaoli (RX) (Reed & Yu 1990) is a benchmark anomaly detector for hyperspectral images. It is derived from the generalized likelihood ratio test (GLRT) (Kay 1998). The RX, along with its many modified versions (Chang 2002), requires that the covariance matrix can be estimated from the neighbourhood pixels of the target pixel, i.e. the local background. As a result, the detection performance of RX is strongly affected by two problems. The first problem is the small sample size. It requires the estimation of a local background covariance matrix from a small number of samples in the high-dimensional space. Under this circumstance, the result is a badly-conditioned and unstable estimation. The second problem is the non-homogeneity of the local background; if this occurs, the effectiveness of the covariance matrix estimation is undetermined (Matteoli et al. 2009).

To overcome the problems with RX, numerous algorithms based on different AD approaches have been presented and developed in the literature. The main difference between the AD approaches lies in the manner in which the background is characterized. In previous studies, no comparative analysis of the contemporary AD algorithms performed on the same dataset and also in identical operating conditions has been done. This study aims to provide such a comparative analysis for the detection of man-made objects. The detection performance of the AD algorithms is generally evaluated on either multipixel or sometimes only on subpixel targets. In contrast, this research attempts to provide a quantitative evaluation of the AD methods at both multipixel and subpixel levels.

The rest of this paper is organized as follows. Section 2 provides an overview of the AD approaches. Materials and methods are given in section 3. Experimental results and discussions are outlined and argued in sections 4 and 5, respectively. Finally, concluding remarks are given in section 6.

## 2 The AD Approaches

The AD approaches can be categorized into three major groups as follows.

1) Improved versions of the RX that use solutions to improve the estimation of the covariance matrix. A possible solution is to regularize the covariance matrix (Hoffbeck & Landgrebe 1996). Based on this solution, Nasrabadi (2008) proposed the regularized-RX that regularizes the covariance matrix by adding a scaled identity matrix to it. However, the most common solutions are as follows:
   - Clustering-based solution. This solution models the background using a clustering of all image pixels. A well-known AD algorithm that uses this solution is the segmented based RX (Seg-RX) proposed by Carlotto (2005). Based on a hyperspectral dataset, Matteoli et al. (2007) showed that the performance of the Seg-RX is superior to the regularized-RX.
   - Dimension reduction (DR) solution. This solution uses DR techniques to reduce the dimension of hyperspectral data prior to AD using RX. In fact, the principal component analysis (PCA) is the common technique used in the DR literature. Therefore, the PCA based RX (PCA-RX) (Basener & Messinger 2009) can be considered as the conventional DR-based detector.

2) Linear subspace based methods. These methods use the linear mixing model to exploit the fact that target and background signals can be reasonably assumed lying in two distinct subspaces of the data space (Matteoli et al. 2010). Two well-known methods in this category are the signal subspace processing AD (SSP-AD) (Ranney & Soumekh 2006) and the orthogonal subspace projection based AD (OSP-AD) (Chang 2005). Matteoli et al. (2007) showed that the OSP-AD outperforms the SSP-AD algorithm based on a hyperspectral image, in which several target panels have been embedded.
3) Kernel-based methods. The basic principle of these methods is that a nonlinear mapping is used to extend the input space to a higher dimensional feature space, the so-called *Hilbert* space (Kwon & Nasrabadi 2007). Kernel functions are used to implicitly compute the dot products in *Hilbert* space without mapping the input vectors into that space (Schölkopf et al. 2001). The Gaussian kernel is commonly accepted for kernel methods (Tax 2001) given by $k(x_i, x_j) = \exp(-|x_i - x_j|^2/\sigma^2)$, where $x_i$ and $x_j$ are two objects in the original feature, i.e. spectral band, space, and $\sigma$ denotes the Gaussian kernel width.
The kernel-based AD methods can be grouped into two sub-categories:
   - Kernel-based versions of the RX that adopt a Gaussian model in *Hilbert* feature space. The Kernel-RX (Kwon & Nasrabadi 2005) and the Kernel PCA-RX (KPCA-RX) (Nasrabadi 2009) are two known methods in this category. Nasrabadi (2009) showed that KPCA-RX outperforms the Kernel-RX on the HYDICE forest radiance dataset.
   - Non-parametric methods such as the kernel-based one-class support vector machines (K1SVM) (Tax & Duin 1999). For the first time, Banerjee et al. (2006) used the K1SVM for AD in hyperspectral images. Based on the HYDICE forest radiance dataset, they also showed that the detection performance of the K1SVM is superior to that of the Gaussian Markov random field (GMRF) based detector proposed by Schweizer & Moura (2001).

## 3 Materials and Methods

### 3.1 *Data Description*

There is a lack of shared hyperspectral datasets for detection purposes (Matteoli et al. 2010). Moreover, the available datasets contain few target samples with known ground truth target locations for valid tests. Hence, most of previous works published, especially those about the subpixel AD, have used simulated data for evaluating the detection performance of AD algorithms.

The only available dataset, which contains several subpixel man-made objects, is the target detection blind test (TDBT) dataset (RIT 2012). Moreover, the FOI (Swedish Defense Research Agency) has provided a hyperspectral dataset containing some vehicles at multipixel level placed in a countryside where no such objects are expected. This dataset is publicly available at FOI (2012). In this study, we also employ an AVIRIS (Airborne Visible and InfraRed Imaging Spectrometer) dataset that contains some multipixel helicopters.

#### TDBT dataset

The TDBT dataset includes two HyMap radiance and reflectance images of Cooke City in Montana, USA. The images were collected by the airborne HyMap (Hyperspectral Mapper) sensor, which has 126 spectral bands (Snyder et al. 2008). The ground resolution of the imagery data is approximately 3 m.

In the HyMap images twelve man-made objects were deployed in an open grass region during the airborne image acquisition. We chose ROI-1 with the size of 90 × 90 pixels in the HyMap radiance image which covers the entire open grass region (Fig. 1). Two

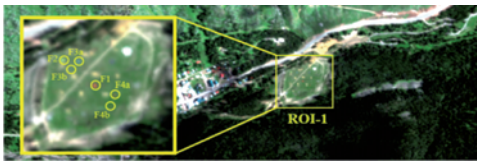


**Fig. 1:** True colour composite of the HyMap radiance image. The box specifies the ROI-1 on which the positions of self-test targets are superimposed.

**Tab. 1:** Characteristics of the targets.

| Self-test targets | | | Blind-test targets | | |
|---|---|---|---|---|---|
| Name | Size | Type | Name | Size | Type |
| F1 | 3 × 3 m | Red Cotton | F5a | 2 × 2 m | Maroon Nylon |
| F2 | 3 × 3 m | Yello Nylon | F5b | 1 × 1 m | Maroon Nylon |
| F3a | 2 × 2 m | Blue Cotton | F6a | 2 × 2 m | Gray Nylon |
| F3b | 1 × 1 m | Blue Cotton | F6b | 1 × 1 m | Gray Nylon |
| F4a | 2 × 2 m | Red Nylon | F7a | 2 × 2 m | Green Cotton |
| F4b | 1 × 1 m | Red Nylon | F7b | 1 × 1 m | Green Cotton |

of the twelve targets are at full pixel, i.e. resolved size; the other ten are at subpixel sizes. The targets include six fabric panels for the self-test and six for the blind-test. Fig. 1 shows the locations of six self-test targets in the ROI-1, while Tab. 1 briefly describes each target in more detail. In Fig. 1, the positions of blind-test targets are not known, because the (ground truth) locations of these targets are currently unavailable to users.

## AVIRIS dataset

The data is an airborne hyperspectral image of a naval air station in San Diego, California, collected by AVIRIS in 1998. The image has 220 spectral bands with a 10 nm spectral width from 0.4 to 2.45 μm and with a ground sampling distance of 3.5 m. The 20 atmospheric water absorption bands (numbered 104–108, 150–163, and 220) were removed from the original image. In addition, 11 noisy bands with low signal-to-noise ratios (numbered 103, 109–112, 148–149, 164–165, and 217–219) were removed, resulting in a total of 189 bands. From this image, a subset consists of 80 × 70 pixels is used, named ROI-2 (Fig. 2). The ROI-2 contains six Sea Hawk helicopters as multipixel targets. These targets have been detected by the spectral angle mapper (SAM) algorithm with an angle threshold of 0.05.

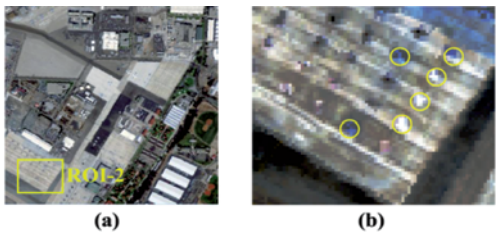


**Fig. 2:** (a) colour composite of the AVIRIS image; (b) zoomed window of the ROI-2 where the circles denote the helicopters.

## FOI dataset

This dataset was collected in an airborne measurement over a countryside in Sweden. It has 60 spectral bands in the visual and near infrared range (390 nm–960 nm) with spectral resolution about 10 nm (Wadströmer et al. 2010). The dataset includes the two scenes 1 and 2 which consist of 1024 × 4000 pixels where for the scene 1 the ground truth of the objects of interest is known. Moreover, each scene was captured in four flights. From scene 1, we used four test subsets with the size of 45 × 45 pixels around four vehicles (Fig. 3).

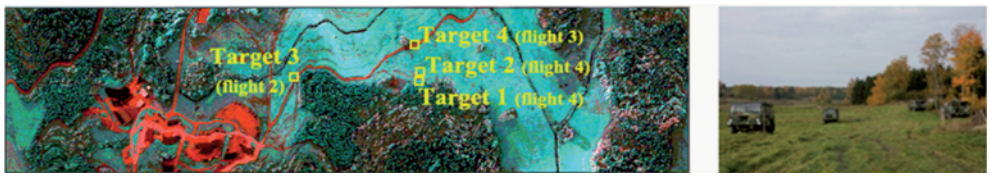


**Fig. 3:** FOI dataset; left: colour composite of scene 1 (flight 4) with the test subsets around four vehicles; right: picture of some of the vehicles in scene 1.

## 3.2 *Contemporary AD Algorithms used*

### Seg-RX

The Seg-RX requires that an unsupervised classification, i.e. segmentation, is performed prior to perform the RX. After obtaining a thematic map, the mean vector and the covariance matrix are estimated over each cluster. Finally, to assign an anomaly value to each test pixel $y$, the well-known Mahalanobis distance is computed between the $y$ and its spectrally nearest cluster $j$ as follows (Matteoli et al. 2009):

$$SRX(y) = (y - \hat{\mu}_j)^T \hat{C}_j^{-1} (y - \hat{\mu}_j) \underset{>H_1}{\overset{\leq H_0}{}} \eta \qquad (1)$$

where $\hat{\mu}_j$ and $\hat{C}_j$ are the mean spectral vector and the estimated covariance matrix for cluster $j$, and $\eta$ is a detection threshold. The spectrally nearest cluster is typically related to the most common cluster in the local neighbouring pixels around the target pixel. The test (1) makes a decision between two competing hypotheses: $H_0$ (target absent hypothesis) and $H_1$ (target present hypothesis).

To segment the images, we employed the well-known K-means algorithm. The main problem of K-means is how to choose the optimal number of clusters. A good solution to select the optimum number of clusters is to apply the K-means algorithm with a different number of desired clusters. Then, one can select the best solution among them by a validity index such as the Davies-Bouldin index (Duran & Petrou 2007).

### PCA-RX

The PCA-RX detector is performed by applying a forward PCA transform, setting the appropriate value of the first PCs to be retained, applying an inverse PCA, and then performing the RX on the resulting image (Basener & Messinger 2009). The PCA is known for its ability to map the data for finding the most important or influencing components in a dataset. These components are optimal and can almost completely represent all data in a reduced feature space. The principal components (PCs) are uncorrelated and ordered according to their magnitude of variance of the original signal (Jackson 1991).

By performing PCA, it can be expected that a few PCs can explain most of the variation in the original data. A key question, that arises here, is how the number of the first PCs should be chosen. There are several methods presented in the literature for determining the optimal number of PCs. A simple but efficient method is the eigenvalue ratio estimator (ERE) algorithm (Ahn & Horenstein 2008). It estimates the optimum number of first PCs via maximizing the ratio of two adjacent eigenvalues (in decreasing order) of the data covariance matrix.

### OSP-AD

The use of OSP for AD was proposed by Chang (2005). For target detection tasks, the OSP detector is given by

$$OSP(y) = d^T (I - WW^{\#}) y \underset{>H_1}{\overset{\leq H_0}{}} \eta \qquad (2)$$

where $d$ is a given spectral signature, $W^{\#} = (W^T W)^{-1} W^T$, and $W$ is a matrix whose columns are projection vectors. The product $WW^{\#}$ represents a subspace for characterizing the spectra that are used to generate the projection vectors. The projection vectors are defined as either endmembers or eigenvectors obtained by the first components of the singular value decomposition (SVD) (Matteoli et al. 2010). However, for AD tasks, the $y$ can be used directly to define the $d$. Moreover, for detecting the multipixel targets which have distinct spectra from the local background pixels, the mean spectrum of the local background pixels is used as a projection vector for local background pixels. In this regard, the resulting detector does not require determining the projection vectors by SVD.

### K1SVM

Two K1SVM algorithms have been presented in the literature. The first one is called the v-support vector classifier ($v$-SVC) (Schölkopf et al. 1999) and aims at finding a hyperplane that separates normal training data from the origin with maximum margin. The second one is the support vector domain description

(SVDD) which is the most common K1SVM algorithm. The SVDD seeks the minimum hypersphere that encloses all normal training data (Tax & Duin 1999). When using the Gaussian kernel, the *v*-SVC solution is equivalent to that of the SVDD (Tax 2001). Given *n* pixels $\{x_i\}_{i=1}^{n}$ belonging to the local background and a Gaussian kernel *k*, the K1SVM problem becomes the following:

$$\min_{\alpha_i} \sum_i \sum_j \alpha_i \alpha_j k(x_i, x_j) \quad (3)$$

with two constraints on Lagrange multipliers ($\alpha_i$): $\sum \alpha_i = 1$ and $0 \le \alpha_i \le 1/(nv)$, where objects $x_i$ with nonzero $\alpha_i$ are called the support vectors (SVs), and *v* is called the rejection rate which tackles the presence of outliers within the local background for constructing an optimal hypersphere.

The K1SVM test statistic defines a pixel *y* is an anomaly when the Euclidean distance from the *y* to the centre of the hypersphere is bigger than the hypersphere radius (Tax 2001).

$$1 - 2\sum_i \alpha_i k(x_i, y) + \sum_i \sum_j \alpha_i \alpha_j k(x_i, x_j) > R^2 \quad (4)$$

where *R* can be determined by calculating the distance from the centre of hypersphere to any of the SVs on the boundary, i.e. objects $x_i$ with $0 < \alpha_i < 1/(nv)$. To improve the detection performance of K1SVM in hyperspectral images, a normalized test statistic can be derived through dividing the original test statistic by the squared radius (Banerjee et al. 2006).

The main problem of kernel-based AD methods such as the K1SVM is the optimal setting of $\sigma$. A straightforward method for estimation of the $\sigma$ is given by Khazai et al. (2011):

$$\hat{\sigma} = \frac{d_{\max}}{\sqrt{\ln(n(1-v)+1)}} \quad (5)$$

where $d_{max}$ is the maximum Euclidean distance between training instances, i.e. surrounding pixels of the target pixel, and the *v* is set experimentally by users. In this study, we set *v* to 0.1; this means that 10% of pixels in the local background are allowed to be outliers.

### KPCA-RX

The KPCA (Schölkopf et al. 1998) is an algorithm for computing the PC vectors in *Hilbert* feature space. However, the KPCA-RX (Nasrabadi 2009) is an improved version of the Kernel-RX. This detector is compactly given by the following test statistic:

$$KPCA(y) = (K_y - K_{\hat{\mu}})^T WW^T (K_y - K_{\hat{\mu}}) \underset{>H_1}{\overset{\le H_0}{}} \eta \quad (6)$$

where $K_y$ is the centred $k(y, X_b)$ which is a kernel-based vector that uses local background pixels $X_b = [x_1, x_2, ..., x_n]$, $K_{\hat{\mu}}$ is the centred $k(\bar{x}, X_b)$ that uses $\bar{x} = 1/n\sum x_i$ as input, and *W* is a matrix containing the most significant, i.e. the first, eigenvectors of the centred kernel matrix $k(X_b, X_b)$. The number of first eigenvectors is a configurable constant that can be estimated using the ERE method.

## 3.3 *Accuracy Assessment*

The primary way used to analyse the ability of AD algorithms is a two-dimensional display of the detection maps. To obtain a fair visual comparison between the AD algorithms, each detection map should be normalized by its maximum value. However, the detection performance of AD methods is usually evaluated based on their experimental receiver operating characteristic (ROC) curves (Wilson 1998). The ROC curve represents the detection rate versus the false alarm rate (FAR) over a particular operating scenario. The detection values for the entire data are, firstly, normalized between zero and one. Then, the detection threshold varies from one to zero through a decrement rate, e.g. 0.001. For each detection threshold, the number of target pixels correctly detected and the corresponding number of false alarms, i.e. non-target pixels, are computed based on the ground truth data of the target pixels.

In this study, the experimental ROC curves of the AD algorithms are plotted using a log-scale on the FAR axis. Compared to the conventional scale of the FAR axis, behaviours of the detectors in a low FAR region are better demonstrated using the log-scale. It is worth-

while to note that the low FAR region is the actual operating region of interest for AD methods (Matteoli et al. 2010). In this study, we compare the performance of the AD algorithms in the low FAR region ranging from 0 to 0.01.

Moreover, to get a quantitative evaluation of the AD methods, the average of FAR (AFAR) values (Bajorski et al. 2004) is used. The AFAR is calculated by averaging the FAR encountered for each detected target pixel $i$ as follows:

$$AFAR = \frac{1}{m}\sum_{i=1}^{m} FAR_i \tag{7}$$

where $m$ represents the number of target pixels. In this study, to alleviate the problem of few target samples in the available datasets, 95% confidence intervals (assuming a Gaussian trial) for AFAR values are computed given by Kerekes (2008):

$$a \pm \frac{\sqrt{a(1-a)}\tau_{N-1,0.025}}{\sqrt{N}} \tag{8}$$

where $a$ is the AFAR value, $N$ represents the number of image pixels within the ROI, and $\tau_{N-1,0.025}$ denotes the cut-off value of a Student t distributed random variable with $N$–1 degrees of freedom such that the probability that the Student t random variable is greater than the cut-off value is (1–0.95)/2, i.e. 0.025.

## 4 Experimental Results

For each dataset, all pixel vectors are first normalized by a maximum spectral value in the image, so that the entries of the normalized pixel vectors fit into the interval of spectral values between zero and one. The rescaling of pixel vectors was mainly performed to effectively utilize the dynamic range of Gaussian kernel used for kernel-based methods (Kwon & Nasrabadi 2005).

An important decision for the AD methods is the way to choose the local background of each pixel. Generally, the dual window technique is used on multipixel targets as the size of targets of interest is bigger than the ground resolution of the image. This technique separates the local area around each pixel into two regions, an inner window region (IWR) and an outer window region (OWR). The IWR is used to capture a target present, while the OWR is employed to model the local background of the target. For ROI-1, as the size of IWR is always 1 × 1, the size of OWR should be set only. Experimentally, a constant window size of 5 × 5 is used to scan the image for all the algorithms on subpixel targets. For ROI-2, the sizes of IWR and OWR were experimentally selected 5 × 5 (as the length of helicopters is about 15 m) and 11 × 11 pixels, respectively. Also, for FOI subsets, we used the size of IWR and OWR to 15 × 15 as the length of vehicles is 7 m and 31 m × 31 m, respectively.

### 4.1 *Results for TDBT Dataset*

Fig. 4 presents the normalized detection results obtained on the ROI-1, where the positions of the self-test target pixels are superimposed.

From Fig. 4, it can be observed that while the OSP-AD provides the best background suppression ability, the K1SVM results in the worst background suppression in comparison with the other algorithms.

Fig. 5 presents the experimental ROC curves of the AD methods obtained on the ROI-1. It shows that the OSP-AD and Seg-RX result in better ROC curves compared to the other algorithms in the low FAR region considered. However, the AFAR values with 95% confidence intervals are 2% ± 1%, 4% ± 1%, 5% ± 1%, 6% ± 1%, and 7% ± 1% using

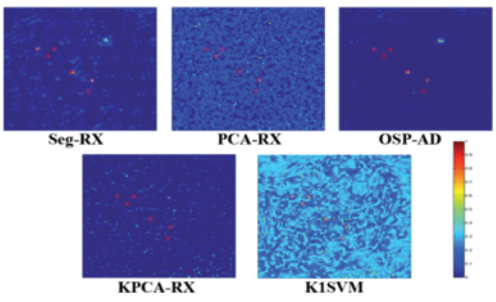


**Fig. 4:** 2D detection results in the ROI-2 using the AD methods. The target pixels are denoted by red circles.

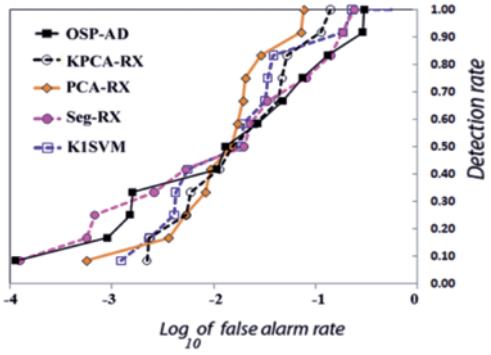


**Fig. 5:** Experimental ROC curves of the algorithms obtained on the ROI-1.

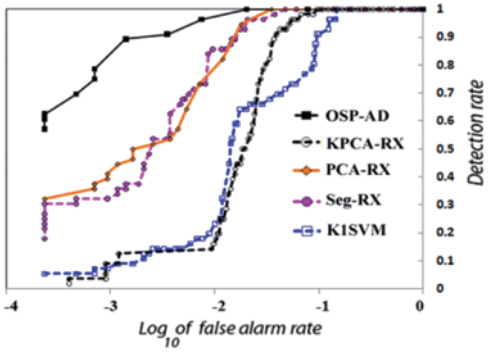


**Fig. 7:** Experimental ROC curves of the algorithms obtained in the ROI-2.

the PCA-RX, KPCA-RX, Seg-RX, OSP-AD, and K1SVM detectors. Therefore, the PCA-RX provides about 2%, 3%, 4%, and 5% less AFAR compared to the KPCA-RX, Seg-RX, OSP-AD, and K1SVM, respectively. Consequently, the PCA-RX manages to detect all subpixel targets with a lower AFAR to a greater degree than other algorithms.

## 4.2 *Results for AVIRIS Dataset*

Fig. 6 depicts the normalized detection results obtained on the ROI-2, where the positions of the target pixels are superimposed. Moreover, Fig. 7 shows the experimental ROC curves obtained by the AD methods.

As can be seen in Fig. 6, both the OSP-AD and PCA-RX algorithms provide strong background suppression ability in comparison with

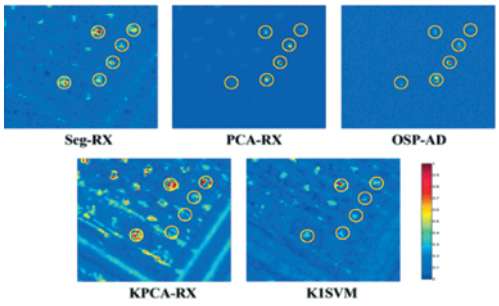


**Fig. 6:** 2D detection results of the AD methods obtained on the ROI-2. The target pixels are denoted by yellow circles.

the other algorithms. Moreover, based on a comparison of ROC curves, Fig. 7 illustrates that the OSP-AD yields a superior detection performance compared to the other detectors in both the low and high FAR regions.

The AFAR values with 95% confidence intervals are 0.05% ± 0.04%, 0.09% ± 0.07%, 0.4% ± 0.1%, 2.1% ± 1%, and 3.2% ± 1% using the OSP-AD, PCA-RX, Seg-RX, KPCA-RX, and K1SVM detectors. Thus, the OSP-AD decreases the AFAR value about 0.04%, 0.35%, 1.95%, 2.05%, and 3.15% compared to the PCA-RX, Seg-RX, KPCA-RX, and K1SVM, respectively. Moreover, the application of PCA-RX results in similar AFAR values exceeding OSP-AD by only 0.04%.

## 4.3 *Results for FOI Dataset*

Fig. 8 depicts the normalized detection results of the AD methods obtained on the FOI test subsets. It highlights that for background suppression, while the best results are obtained on the test subset 4, the worst results are achieved on the test subset 3.

Fig. 9 shows the average ROC curves of the AD methods achieved on the four test sets. From this figure, we can observe that the OSP-AD performs the best out of all the AD algorithms in both the low and high FAR regions. In addition, it illustrates that the PCA-RX has the lowest performance in the low FAR region. Moreover, Figs. 8 and 9 indicate that among the AD algorithms the kernel-based methods,

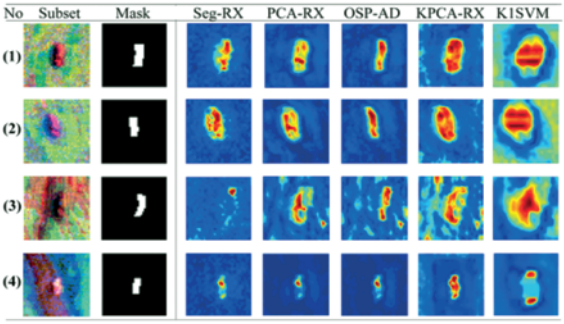


**Fig. 8:** FOI test subsets around each target with detection maps obtained by AD methods.

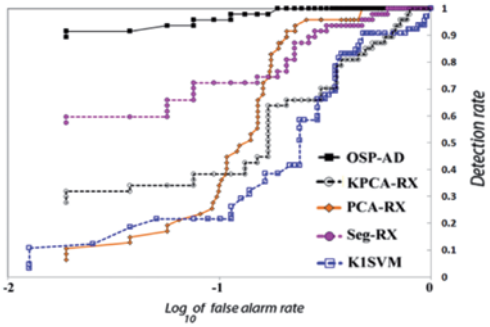


**Fig. 9:** Average ROC curves of the algorithms obtained on the four FOI test subsets.

i.e. K1SVM and KPCA-RX, provide the worst results on the examined test subsets.

The results also show that the AFAR values of the methods with their 95% confidence intervals are 3.2% ± 1%, 3.7% ± 1%, 4.3% ± 1%, 7.9% ± 1%, and 12% ± 2% using the OSP-AD, PCA-RX, Seg-RX, KPCA-RX, and K1SVM algorithms, respectively. Thus, for the FOI test subsets, the OSP-AD performs the best out of all the AD algorithms considered. Comparative analysis also reveals that the PCA-RX provides only a 0.5% smaller AFAR value than the OSP-AD.

## 5 Discussion

Based on the experimental results obtained using the contemporary AD algorithms, two important points are presented and discussed here:

### 5.1 *The Effect of Background Complexity on Detection Performance*

In general, when the local background consists of multiple data classes, AD algorithms suffer from low performance. A solution to evaluate the complexity level of the background is estimating the intrinsic dimensionality (ID) of the data. A simple method for estimating the ID in a given dataset is to estimate the number of first PCs to be retained (Martinez et al. 2010). Based on the ERE method, Tab. 2 shows the number of ID obtained over each dataset.

From Tab. 2, we can observe that the TDBT and AVIRIS datasets have a low complexity level of background. In contrast, the complexity level of the background for the FOI test subsets is very high. However, comparing the results obtained from the AVIRIS and FOI

**Tab. 2:** ID and range of AFAR values obtained on the datasets used.

| **Dataset →** | TDBT (ROI-1) | AVIRIS (ROI-2) | FOI (test subsets) | | | |
|---|---|---|---|---|---|---|
| | | | 1 | 2 | 3 | 4 |
| ID | 2 | 1 | 34 | 30 | 29 | 8 |
| The AFAR values | 2%–7% | 0.05%–3% | 3.2%–12% | | | |

subsets, it can be concluded that the poor performance of the detectors on FOI test subsets is due to the high complexity level of the background. Clearly, when the value of estimated ID is not significant, AD algorithms can provide appropriate results. This can be demonstrated on the TDBT and AVIRIS datasets as the AFAR values of the methods is very low compared to the FOI test subsets.

### 5.2 *Comparison with other Results*

Based on the HYDICE forest radiance dataset, the results obtained by Nasrabadi (2009) and Banerjee et al. (2006) show that the KPCA-RX and K1SVM can detect man-made objects well. Nonetheless, our experiments demonstrate that these kernel-based AD algorithms result in poor performance compared to the OSP-AD and PCA-RX algorithms. This result implies that using the kernel-based AD methods, it may not be possible to detect man-made anomalies in the original feature space. Evangelista et al. (2006) also indicated that the kernel-based AD methods suffer from the so-called curse of dimensionality. As a result, the kernel-based AD methods may provide a high detection performance in combination with DR techniques (as a preprocessing step).

On the other hand, in a study for the purpose of detecting multipixel man-made targets in hyperspectral images, Borghys et al. (2011) compared the detection performance of the OSP-AD and Seg-RX algorithms. They reported that the OSP-AD gives better results than the Seg-RX using three HyMap image scenes, Oberpfaffenhofen, Hartheim, and Camargue. Moreover, Matteoli et al. (2007) analysed an image dataset acquired by the SIM-GA sensor, and showed that the OSP-AD has superior performance compared to the Seg-RX algorithm. This study also confirms the superiority of the OSP-AD over the Seg-RX algorithm based on the experimental results obtained from the AVIRIS and FOI datasets.

## 6 Conclusion

The experiments in question suggest some conclusions about the capabilities of five contemporary anomaly detectors Seg-RX, PCA-RX, OSP-AD, KPCA-RX, and K1SVM in detecting man-made anomalies. Based on the three examined datasets, the results showed that the OSP-AD achieves the best performance for detecting multipixel man-made targets. Moreover, to detect the subpixel targets, while the PCA-RX is overall the best AD algorithm, the OSP-AD and Seg-RX provide the best performance in the low FAR region, which is in fact the operating region of interest for AD methods. Consequently, the OSP-AD is the most promising AD algorithm for detecting man-made objects. This research also found that the kernel-based methods applied to the data in the original space are not suitable for detecting man-made objects. However, we point out that the use of more hyperspectral datasets can provide more reliable assessments. In addition, all results are dependent on the IWR and OWR parameter settings, signal-to-noise level, and the free parameters involved. The impact of these factors on the detection performance along with the computational complexity of the algorithms will be investigated in future work.

## Acknowledgements

The authors would like to thank the Digital Imaging and Remote Sensing group in the Center for Imaging Science, Rochester Institute of Technology, Rochester, NY, USA, for providing the Target Detection Test datasets, Dr. J.P. Kerekes for his valuable help in providing truth locations of the blind-test targets, the Swedish Defence Research Agency, specially Niclas Wadströmer and Jörgen Ahlberg, for providing the FOI dataset, and Dr. D.M.J. Tax for the MATLAB dd-tools, which allowed us to implement the K1SVM.

## References


Ahn, S.C. & Horenstein, A., 2008: Eigenvalue ratio test for the number of factors. – Working paper, Arizona State University.

Bajorski, P., Ientilucci, E. & Schott, J., 2004: Comparison of basis vector selection methods for target and background subspaces as applied to subpixel target detection. – SPIE **5425:** 97–108.

Banerjee, A., Burlina, P. & Diehl, C., 2006: A support vector method for anomaly detection in hyperspectral imagery. – IEEE Transactions on Geoscience and Remote Sensing **44** (8): 2282–2291.

Basener, W.F. & Messinger, D.W., 2009: Enhanced detection and visualization of anomalies in spectral imagery. – Shen, S.S. & Lewis, P.E. (eds.): Algorithms and Technologies for Multispectral, Hyperspectral, and Ultraspectral Imagery XV. – SPIE **7334**.

Borghys, D., Achard, V., Rotman, S.R., Gorelik, N., Perneel, C. & Schweicher, E., 2011: Hyperspectral anomaly detection: a comparative evaluation of methods. – General Assembly and Scientific Symposium of the International Union of Radio Science **XXX** URSI: 1–4.

Carlotto, M.J., 2005: A cluster-based approach for detecting man-made objects and changes in imagery. – IEEE Transactions on Geoscience and Remote Sensing **43** (2): 374–387.

Chang, C.-I., 2002: Anomaly detection and classification for hyperspectral imagery. – IEEE Transactions on Geoscience and Remote Sensing **40** (6): 1314–1325.

Chang, C.-I., 2005: Orthogonal subspace projection (OSP) revisited: A comprehensive study and analysis. – IEEE Transactions on Geoscience and Remote Sensing **43** (3): 502–518.

Duran, D. & Petrou, M., 2007: A time-efficient method for anomaly detection in hyperspectral images. – IEEE Transactions on Geoscience and Remote Sensing **45** (12): 3894–3904.

Evangelista, P.F., Embrechts, M.J. & Szymanski, B.K., 2006: Taming the curse of dimensionality in kernels and novelty detection. – Applied Soft Computing Technologies: The Challenge of Complexity: 425–438.

FOI, 2012: http://www.foi.se/hsi/ (2.9.2012).

Hoffbeck, J. & Landgrebe, D., 1996: Covariance matrix estimation and classification with limited training data. – IEEE Transaction on Pattern Analysis and Machine Intelligence **18** (7): 763–767.

Jackson, J.E., 1991: A User's guide to principal components. – John Wiley and Sons.

Kay, S.M., 1998: Fundamentals of statistical signal processing: detection theory. – Prentice-Hall, Upper Saddle River, NJ, USA.

Khazai, S., Homayouni, S., Safari, A. & Mojaradi, B., 2011: Anomaly detection in hyperspectral images based on an adaptive support vector method. – IEEE Geoscience and Remote Sensing Letters **8** (4): 646–650.

Kerekes, J.P., 2008: Receiver operating characteristic curve confidence intervals and regions. – IEEE Geoscience and Remote Sensing Letters **5** (2): 251–255.

Kwon, H. & Nasrabadi, N.M., 2005: Kernel RX-algorithm: a nonlinear anomaly detector for hyperspectral imagery. – IEEE Transactions on Geoscience and Remote Sensing **43** (2): 388–397.

Kwon, H. & Nasrabadi, N.M., 2007: A comparative analysis of kernel subspace target detectors for hyperspectral imagery. – EURASIP Journal on Advances in Signal Processing **2007** (1).

Martinez., W.L., Martinez, A. & Solka, J., 2010: Exploratory data analysis with MATLAB. – Second Edition, CRC Press.

Matteoli, S., Carnesecchi, F., Diani, M. & Corsini, G., 2007: Comparative analysis of hyperspectral anomaly detection strategies on a new high spatial and spectral resolution data set. – SPIE **6748**.

Matteoli, S., Diani, M. & Corsini, G., 2009: Different approaches for improved covariance matrix estimation in hyperspectral anomaly detection. – Riunione Annuale GTTI: 1–8.

Matteoli, S., Diani, M. & Corsini, G., 2010: A tutorial overview of anomaly detection in hyperspectral images. – IEEE A&E Systems Magazine **25** (7): 5–27.

Nasrabadi, N.M., 2008: Regularization for spectral matched filter and RX anomaly detector. – SPIE **6966**.

Nasrabadi, N.M., 2009: Kernel subspace-based anomaly detection for hyperspectral imagery. – Hyperspectral Image and Signal Processing: Evolution in Remote Sensing, WHISPERS '09.

Ranney, K.I. & Soumekh, M., 2006: Hyperspectral anomaly detection within the signal subspace. – IEEE Geoscience and Remote Sensing Letters **3** (3): 312–316.

Reed, I.S. & Yu, X., 1990: Adaptive multiple-band CFAR detection of an optical pattern with unknown spectral distribution. – IEEE Transactions on Acoustics, Speech, and Signal Processing **38** (10): 1760–1770.

RIT, 2012: http://dirsapps.cis.rit.edu/blindtest/ (2.9.2012).

Schölkopf, B., Smola, A. & Muller, K.-R., 1998: Nonlinear component analysis as a kernel eigen-

value problem. – Neural Computation **10:** 1299–1319.

Schölkopf, B., Williamson, R.C., Smola, A. & Shawe-Taylor, J., 1999: SV estimation of a distribution's support. – NIPS'99.

Schölkopf, B., Platt, J.C., Shawe-Taylor, J. & Smola, A., 2001: Estimating the support of a high dimensional distribution. – Neural Computation **13** (7): 1443–1471.

Schweizer, S.M. & Moura, J.M.F., 2001: Efficient detection in hyperspectral imagery. – IEEE Transactions on Geoscience and Remote Sensing **10** (4): 584–597.

Snyder, D., Kerekes, J., Fairweather, I., Crabtree, R., Shive, J. & Hager, S., 2008: Development of a web-based application to evaluate target finding algorithms. – IEEE International Geoscience and Remote Sensing Symposium (IGARSS) **2:** 915–918.

Tax, D.M.J., 2001: One-class classification. – Ph.D. dissertation, Delft University of Technology.

Tax, D.M.J. & Duin, R.P.W., 1999: Support vector domain description. – Pattern Recognition Letters **20** (11): 1191–1199.

Wadströmer, N., Ahlberg, J. & Svensson, T., 2010: A new hyperspectral dataset and some challenges. – Shen, S.S. & Lewis, P.E. (eds.): Algorithms and Technologies for Multispectral, Hyperspectral, and Ultraspectral Imagery XVI. – SPIE **7695**.

Wilson, T.A., 1998: Automatic target cueing of hyperspectral image data. – Ph.D. dissertation, Air Force Institute of Technology, USA.

Addresses of the authors:

Dr. Safa Khazai, Prof. Dr. Abdolreza Safari & Prof. Dr. Saeid Homayouni, Department of Surveying and Geomatics Engineering, University College of Engineering, University of Tehran, PO Box 11155-4563, Tehran, Iran, Tel: +98-021-8800884, Fax: +98-21-88008837, e-mails: {khazai}{asafari}{shomayounis}@ut.ac.ir.

Prof. Dr. Barat Mojaradi, School of Civil Engineering, Iran University of Science & Technology, Narmak, PO Box 16765-163, Tehran, Iran, Tel: +98-21-77240399 & 77240565, Fax: +98-21-77240398, e-mail: mojaradi@iust.ac.ir.

Manuskript eingereicht: Februar 2012
Angenommen: Juni 2012

PFG 2013 / 1, 0031 – 0041
Stuttgart, February 2013

Article

# Introducing a Method for Spectral Enrichment of the High Spatial Resolution Images

Fakhereh Alidoost, Mohammad R. Mobasheri & Ali A. Abkar, Tehran, Iran

**Keywords:** spatial resolution, spectral resolution, urban environments, spectral mixture analysis, image fusion

**Summary:** Almost all pixels located in the urban region imaged by high/medium spatial resolution sensor systems are mixed. To resolve this problem, usually the unmixing techniques are deployed. One of the useful unmixing methods is spectral mixture analysis. It can be grouped into two parts of spectral unmixing and spatial unmixing. In this study, spectral reflectance of important urban classes is determined using spatial unmixing method. To this end, spatial information from IKONOS imagery and spectral information from Hyperion data are employed. The validity of the proposed method is substantiated through comparison of an original Hyperion image with the reconstructed image. The experimental results lead to a mean RMSE and a mean NCC of 0.03 and 0.89 respectively. In the next stage, using the extracted spectral reflectance, an image with 4 m spatial resolution and 136 bands is produced where variability of urban land covers is taken into account. It is believed that this methodology will help researcher to monitor urban change as well as urban pollution effectively.

**Zusammenfassung:** *Neue Methode zur spektralen Verbesserung von räumlich hoch aufgelösten Fernerkundungsszenen.* In urbanen Gebieten besitzen Fernerkundungsszenen fast ausschließlich Mischpixel. Üblicherweise werden unmixing Methoden wie die spectral unmixing analysis verwendet. Diese lässt sich in die spektrale und die räumliche Entmischung gliedern. Die vorliegende Untersuchung hat gezeigt, dass mit Unterstützung der räumlichen Entmischung die Identifizierung der spektralen Klassen städtischer Gebiete verbessert werden kann. Die Methode wurde mit IKONOS-Daten für die räumliche und Hyperion-Daten für die spektrale Information erprobt und ergab eine Genauigkeit für den RMSE von 0,03 und den NCC von 0,89. Aus beiden Datensätzen wurde eine Bildkarte mit einer GSD von 4 m und einer spektralen Auflösung von 136 Kanälen hergestellt, die sehr gut die Vielfalt der urbanen Landnutzung wiedergibt und das Monitoring von Landnutzungswandel und Umweltverschmutzung ermöglicht.

## 1 Introduction

There are several important un-answered questions regarding the spectral properties of urban surface materials. For instance, how do these materials differ in their spectral responses? What are the most suitable spectral bands for mapping urban land cover? What are spectral limitations of current high spatial resolution remote sensor systems in terms of mapping urban land cover?

Merging the data collected by sensors with different spatial and spectral resolutions may in many cases be a valuable tool to the analyst (Haertel & Shimabukuro 2005). Multisensor multiresolution technique (MMT) is a technique that can be applied to unmix low spatial resolution images using information regarding pixel composition extracted from co-registered high-resolution images. This makes fusion of the low and high-resolution images for synergetic interpretation possible (Zhukov et al. 1999).

High resolution remote sensing data are of special interest for a variety of applications related to urban planning and management. Hyperspectral data, on the other hand, provide extensive spectral information that can help to discriminate materials (Mobasheri & Ghamary Asl 2011) and (Herold et al. 2002).


www.schweizerbart.de
DOI: 10.1127/1432-8364/2013/0156
1432-8364/13/0156 $ 2.75

In this work, an approach that employs the linear unmixing model is used. The technique is expected to produce reflectance images with both high spectral and spatial resolution. The data used are IKONOS multispectral and Hyperion hyperspectral images in urban environments. The concept of mixed pixels, spectral mixture analysis (SMA) and MMT is discussed in section 2. Section 3 illustrates the proposed method. Study area and preprocessing steps are introduced in section 4. The experiments, results and discussion are presented in section 5. Finally, conclusions and recommendations for MMT application in urban environments are given in section 6.

## 2 Background

### 2.1 *Fraction Determination*

Some approaches determine the endmembers in mixed pixels. This is done by using the SMA technique. The equations of the SMA technique can be given by:

$$\rho'_\lambda = \sum_{i=1}^{N} f_i * \rho_{i\lambda} + \varepsilon_\lambda \qquad (1)$$

Where $\rho'_\lambda$ is mixed pixel reflectance, $f_i$ and $\rho_{i\lambda}$ are fraction and reflectance of *i*th endmember in the pixel respectively and $\varepsilon_\lambda$ is the model residual taken as error involved due to the un-accounted materials as well as measurement errors. Then for determining endmember fractions, (1) can be written in a matrix form as:

$$\begin{bmatrix} \rho'_1 \\ \rho'_2 \\ \vdots \\ \rho'_m \end{bmatrix} = \begin{bmatrix} \rho_{11} & \rho_{12} & \cdots & \rho_{1n} \\ \rho_{21} & \rho_{22} & \cdots & \rho_{2n} \\ \vdots & \vdots & \ddots & \vdots \\ \rho_{m1} & \rho_{m2} & \cdots & \rho_{mn} \end{bmatrix} \begin{bmatrix} f_1 \\ f_2 \\ \vdots \\ f_n \end{bmatrix} + \varepsilon_\lambda \qquad (2)$$

where $m$ is the number of bands, i.e. number of equations, $n$ is the number of endmembers, i.e. number of column of the $\rho$ matrix. The fraction of each endmember in a pixel can be calculated using the least-squares method in which the residual $\varepsilon_\lambda$ is minimized. The least-squares method is subject to two constraints: all fractions are nonnegative and sum of fractions equals 1.

In a standard application of SMA, a fixed number of sample endmembers are selected and the entire image pixels are modeled by the spectra of the components of these samples. However, this procedure is limited, because the selected endmember spectra may not effectively model all elements in the image, or a pixel may be modeled by endmembers that do not correspond to the materials located in its field of view (Powell et al. 2007). Multi endmember spectral mixture analysis (MESMA) allows the number and type of endmembers to vary pixel by pixel and as a result endmember variability is taken into account.

### 2.2 *Determination of Class Reflectance Spectra*

The determination of the radiance (or reflectance) spectra of the classes in each mixed pixel using spectral mixture analysis is the objective of some urban research. For determining class reflectance spectra in one band and $n$ pixels, (1) can be written as:

$$\begin{bmatrix} \rho'_1 \\ \rho'_2 \\ \vdots \\ \rho'_m \end{bmatrix} = \begin{bmatrix} f_{11} & f_{12} & \cdots & f_{1n} \\ f_{21} & f_{22} & \cdots & f_{2n} \\ \vdots & \vdots & \ddots & \vdots \\ f_{m1} & f_{m2} & \cdots & f_{mn} \end{bmatrix} \begin{bmatrix} \rho_1 \\ \rho_2 \\ \vdots \\ \rho_n \end{bmatrix} + \varepsilon_\lambda \qquad (3)$$

where $\rho'$, $f$ and $\rho$ are $n \times 1$, $n \times m$ and $m \times 1$ are matrices, $n$ is the number of pixels, i.e. number of equations, $m$ is the number of classes and the number of column of the $f$ matrix and $\varepsilon$ is the model residual. A constrained least-squares method is used to retrieve spectral information (band-$i$ reflectance) for each of the class reflectance spectra ($\rho$). The use of a constrained method is justified when one expects that the solution fulfils the following two conditions: 1) the radiance (or reflectance) values must be positive and 2) the radiance values cannot be larger than the radiance saturation values of low resolution sensor (or reflectance cannot be larger than 1). In these approaches, determination of class fractions for forming coefficient matrix and selection of suitable pixels are of vital importance.

In recent years Zhukov et al. (1999), Zurita-Milla et al. (2008), Zurita-Milla et al. (2009), Mezned & Abdeljaoued (2009), Haertel & Shimabukuro (2005), Zeng et al. (2007), Busetto et al. (2008), Amoros Lopez et al. (2010) and Amoros Lopez et al. (2011) used this method for determining class reflectance spectra. Subtle analysis of these works reveals that there are a few of these researches that have been focused on urban environments using this method applied to very high spatial resolution images such as IKONOS, QuickBird and GeoEye as well as hyperspectral images such as Hyperion and AVIRIS.

To apply the aforementioned equations to all bands and all pixels in the image, there are still two major problems. Firstly, the coefficient matrix (fractions matrix) may get too big. Secondly, the variability of spectra within a class cannot be found, i.e. only one spectrum can be determined for each class. To overcome these problems, different solutions are suggested. A window with certain dimension in low spatial resolution image can be used to consider class spectra variability in the whole image where the central pixel will be unmixed using characteristics of its neighbouring pixels. It is noteworthy that in this approach, window size and pixel size in low resolution imagery is important since it might produce large errors particularly for the case of urban areas.

## 3 Methodology

It is believed that by using high spatial and high spectral resolution imagery of the same scene, it is possible to extract spectral reflectance of sub-pixel themes. However, in this process two assumptions are made: 1) availability of relatively high spatial/spectral resolution images for the scene, 2) applicability of the linear mixing model. The technique presented in this work is named spectral enrichment of the high-spatial resolution images (SEHR). The method consists of five steps. In the first step, the high spatial resolution data are used to compute the fractional coverage of different classes present in each pixel. In the second and third steps the fractions are used to look for per-pixel endmembers reflectance spectra. In the fourth step, the extracted reflectance curves will be validated and in the final step, this information will be fused to high spatial resolution image to produce an image having both high spatial and spectral characteristics simultaneously. From this point of view, the high-resolution image is conventionally called the classifying instrument (CI), while the lower-resolution image is called the measuring instrument (MI) (Zhukov et al. 1999).

(3) is used for the determination of the class reflectance in one band and in $n$ pixels. The SMA equation system and its constraints for the determination of reflectance spectra of each of the classes are presented in (4).

$$\begin{aligned} &P' = F.P + V \\ &\overline{P} = (F^T W F)^{-1} F^T W P' \\ &\left\{ \begin{matrix} V^T W V : \min \\ 0 \le \overline{P} \le 1 \end{matrix} \right\} \end{aligned} \tag{4}$$

Where P' is the mixed pixels reflectance matrix, $F$ and P are the fraction and the reflectance matrices respectively, $V$ is the model residual matrix, $\overline{P}$ is the estimated reflectance and $W$ is the weight matrix.

As mentioned earlier, the method consists of the following operations:

1. Classification of high resolution image and extraction of the pixels class fractions.
2. Window-based unmixing of the MI-pixels for the calculation of the reflectance spectra for each class.
3. Class reflectance spectra clustering for determination of class sample reflectance spectra.
4. Validation.
5. Image fusion.

### 3.1 *Fraction Determination*

The high spatial resolution image is used to determine the fraction of the main class components present in the mixed pixels. In many researches (section 2), the CI image is classified using unsupervised classification technique. In this study, in order to compare the result of hard and soft classification in the MMT, the CI image is classified into *nc* classes using K-means as a hard clustering tech-

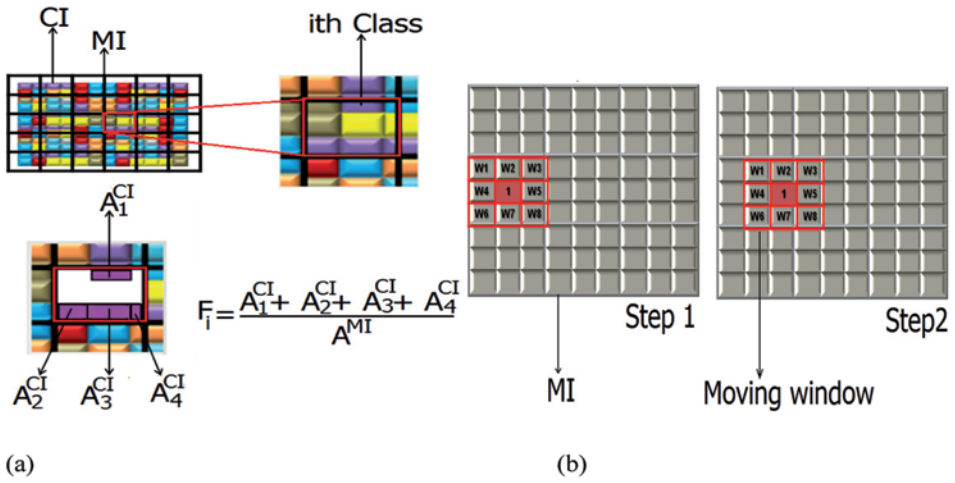


**Fig. 1:** (a) Fraction determination: The fractions related to each MI pixel are calculated using the area of each class; (b) Weighted moving window.

nique (MacQueen 1967) and Fuzzy C-means as a soft clustering technique (Bezdek 1981). Several *nc* values ranging from 3 to 20 are tested in this work. In this paper a novel approach is used for the determination of each class fraction in each mixed pixel. Both CI and MI images are brought to the same coordinate system. The fractions related to each MI pixel are calculated using the area of each class in one mixed pixel in the map coordinate system through (5). It is important to note that in the map coordinate system, the intersection of low and high spatial resolution pixels result in many sub-pixel regions where they have been considered in this equation (Fig. 1a). Therefore, these sub-pixels area that contributed to mixing reflectance spectra are considered in (5). In addition, the sum-to-one and non-negativity of fraction values are also satisfied.

$$f_i = \frac{\sum_{j=1}^{n} (A_j^{CI})}{A^{MI}} \qquad (5)$$

where, $f_i$ is the fraction for $i$th class, $A_j^{CI}$ is the area of $j$th polygon in $i$th class, $A^{MI}$ is the area of a mixed pixel and $n$ is the number of polygons in $i$th class.

## 3.2 *Calculation of Class Reflectance*

To retrieve the class reflectance spectra, the inverse linear spectral mixture analysis is used (4). The unmixing procedure for the MI pixels is performed. According to Zhukov et al. (1999), "the unmixing of the MI pixels is performed in the moving window mode". In order to unmix the central MI pixel in the window, contextual information of the surrounding MI pixels is used" (Fig. 1b). A $n$ by $n$ window which is moving 1 MI pixel step at a time is used in order to solve $n^2$ equations to unmix the central pixel. The size of selected window should be kept as small as possible so that the fused image gets spectrally consistent with the variability expected for the low spatial resolution images (Zurita-Milla et al. 2008). On the other hand, the size of this window should be sufficiently large to provide enough equations for solving the equation system. Since each system of equations results in a unique solution, the size of the selected windows should be appropriate to fulfil this task (Zurita-Milla et al. 2008). In this study, moving windows of 3 by 3 and 5 by 5 pixels dimensions are used, since high spectral variability of urban areas does not allow the use of windows of larger size. A weighted constrained least-square method is deployed for deriving the class reflectance spectra (Fig. 1b). Weights

can be calculated using spectral similarity and Euclidean distance in each window (Busetto et al. 2008). For the spectral similarity, the spectral information divergence (SID) method (Chang 1999) is used. As a result, larger weights are assigned to the pixels which are closer and more similar to central pixel in each window (6).

$$W = \frac{\text{Similarity}}{\text{Distance}} \tag{6}$$

### 3.3 *Determination of the Candidate Class Reflectance Spectra*

Having applied the aforementioned moving windows to MI pixels, a set of reflectance spectra for each class is derived (Fig. 2a). It is worth noting that by averaging over this set, one reflectance spectra will be assigned to each class. However, this averaging procedure misses the within-class variability. Moreover, with this averaging it becomes hard to identify the noisy spectra if one is interested in. To avoid these difficulties, as a novel approach the K-means clustering technique is used in this work. Each set of reflectance spectra for each class is clustered into ns candidate class reflectance spectra (Fig. 2b).

### 3.4 *Validation of the SEHR Technique*

If the class reflectance spectra and class fractions in the mixed pixels are accessible, it is possible to reconstruct the reflectance spectra of that mixed pixel using (1). However, these mixed pixels not being used in the calculation of the class reflectance spectra can be used for validation. The validity of the proposed method is substantiated through a comparison of the original mixed pixels with the reconstructed ones. As mentioned in section 3, each class has many candidate reflectance spectra and each mixed pixel contains several classes. For the reconstruction of the mixed pixel, different combinations of class reflectance spectra are mixed and tested with the original pixel reflectance spectra. The best reconstructed mixed pixel compared to the relevant original mixed pixel is selected based on minimum root-mean-square error (RMSE) values. This approach is based on MESMA technique offered by Powell et al. (2007).

The quantitative assessment is conducted by applying the RMSE, relative error (R_Error) and normalized cross correlation (NCC) (Bieniarz et al. 2011) for each reconstructed MI pixel (7, 8 & 9). Finally, the mean RMSE, mean R_Error and mean NCC for the whole reconstructed MI image are calculated.

$$RMSE_j = \sqrt{\frac{\sum_{i=1}^{n}(\rho_i^C - \rho_i^O)^2}{n-1}} \quad j = 1:N \tag{7}$$

$$NCC_j = \frac{1}{n-1}\sum_{i=1}^{n}\frac{(\rho_i^C - \rho_m^C)(\rho_i^O - \rho_m^O)}{\sigma^C \sigma^O} \quad j = 1:N \tag{8}$$

$$R\_Error_j = \left|\frac{\rho_m^O - \rho_m^C}{\rho_m^O}\right| \times 100 \quad j = 1:N \tag{9}$$

where, $N$ is the number of reconstructed pixels, $n$ is the number of bands, $\rho_i^C$ and $\rho_i^O$ stand for

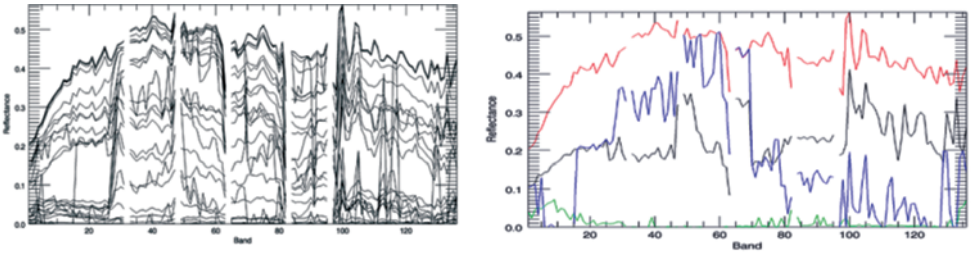


(a) (b)

**Fig. 2:** (a) A set of reflectance spectra for one class; (b) Candidate class reflectance spectra for same class.

reconstructed and original reflectance in *i*th band, $\rho_m^C$ and $\rho_m^O$ are the mean of reconstructed and original reflectance in *n* bands, ($\sigma^C$) and ($\sigma^O$) are the standard deviation of reconstructed and original reflectance in *n* bands.

### 3.5 *Image Fusion*

Finally, a fused image is generated by replacing each of the CI pixels by its corresponding spectral signature. This process results in a hyperspectral/high spatial resolution image with spatial/spectral variability in an urban environment. Spatial variability is addressed by allowing the type of reflectance spectra for each class to vary throughout the image. Spectral variability is addressed by allowing the number and type of spectra to vary from pixel to pixel as defined by Powell et al. (2007).

## 4 Datasets and Pre-processing

### 4.1 *Study Area*

The test area is located at Qods city in the south west of Tehran, Iran. An IKONOS MS and EO-1 Hyperion image with 4 m and 30 m spatial resolution respectively are supplied for this area (Fig. 3). This area is selected based on heterogeneity of the landscape in urban environment, cloud free condition and small difference in the acquisition time of IKONOS and Hyperion images.

### 4.2 *Image Pre-processing*

#### IKONOS Data

The IKONOS data consisted of one panchromatic image with 1 m spatial resolution and one multi-spectral image with 4 spectral bands (b/g/r/nir) and 4 m spatial resolution. It was acquired on August 29, 2004.

Geometric correction is carried out by the supplier (National Cartographic Center of Iran) using 1:2000 topographic maps through the nearest neighbour re-sampling approach.

10 and 11 are used for converting IKONOS DN data to reflectance (Taylor 2005). This preprocessing is needed for image fusion approach mentioned in the previous section.

Reflectance is defined as (Taylor 2005),

$$\rho_i = \frac{\pi L_i d^2}{E_i \cos(\theta)} \tag{10}$$

where, $\rho_i$ is the unitless planetary reflectance, $L_i$ is the radiance for spectral band *i* at the sensor's aperture (W/(m²·µm·sr)), *d* is the Earth-sun distance, $E_i$ is the mean solar exoatmospheric irradiance at band *i* (W/(m²·µm)) and $\theta$ is the solar zenith angle. $L_i$ can be obtained with the correct units from the IKONOS image product by converting from DN to radiance using (12) (Taylor 2005),

$$L_i = \frac{10^4 \times DN_i}{Calcoef_i \times bandwidth_i} \tag{11}$$

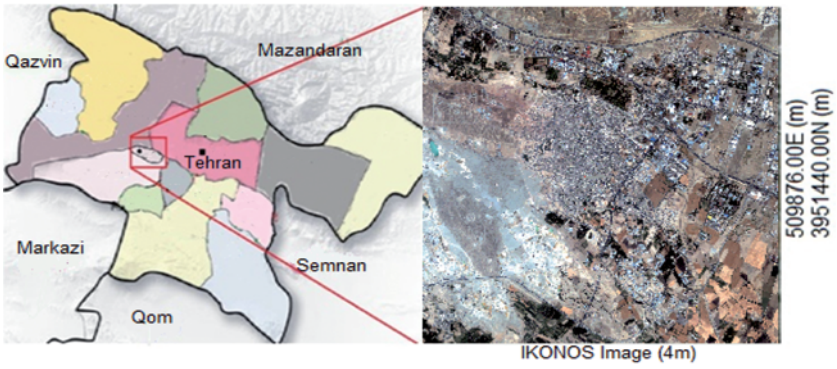


**Fig. 3:** Location of the study area in Qods city in the south west of Tehran, Iran.

where, $Calcoef_i$ is the radiometric calibration coefficient (DN/(mW·cm$^2$·sr)) and $bandwidth_i$ is the width of the spectral band *i* (nm). Both $Calcoef_i$ and $bandwidth_i$ for the IKONOS bands are given by Taylor (2005). The Earth-sun distance (d) can be obtained from any nautical handbook (Taylor 2005).

### Hyperion data

An EO-1 Hyperion image acquired on August 21, 2004, around 11:00 a.m. local time is used for this study. These data are available from the USGS website with 242 spectral bands at 30 m spatial resolution.

Due to the low signal-to-noise ratio for the first few as well as the last few Hyperion spectral bands and also because of the heavy water absorption in several bands, only 196 bands were selected (bands 8 to 57 and 79 to 224). A shift of one pixel in the line direction is corrected in the SWIR image data. This shift occurs at column 128 (Staenz et al. 2002). In addition, an atmospheric correction is carried out using FLAASH in ENVI 4.7 ® software with the appropriate input data. As a result, radiance is converted to reflectance.

Geometric correction for Hyperion relative to geo-referenced IKONOS is done using 18 ground control points (GCPs) and 7 check points by the nearest neighbour re-sampling and second order of polynomial equations in PCI ® 9.1 software. The geometric errors obtained for GCPs and check points are 5.95 m and 6.63 m, respectively. However, using very high spatial resolution images, it is necessary to carry out precise registration and avoid misalignment errors. In this paper the geocoding results are adequate, showing a RMSE of 0.2 pixels. An analysis of the MMT sensitivity to sensor errors showed that the co-registration errors should not exceed 10 to 20 percent of the low-resolution pixel size (Zhukov et al. 1999).

Finally, the corrected Hyperion data with 136 appropriate bands according to EO1HS-DATA (Barry 2001) in the UTM Zone 39 N WGS-84 projection are used in this study.

## 5 Results and Discussion

A sample subset (30 by 30 pixels) from Hyperion image is selected as the study area. This subset corresponds to a subset (219 by 219 pixels) of the IKONOS image. Both image subsets covering the study area are shown in Fig. 4. The sample site is predominantly covered by urban structures, i.e. buildings, road, roofs, parking lots etc. The subset from Hyperion image has no bad stripes. The sample subset is divided into two parts. Part 1 is used for determination of class reflectance spectra using inverse linear spectral mixture whereas part 2 is used for validation. Hereinafter, part 1 and 2 are called the unmixing image (UI) and validation image (VI), respectively.

For an assessment purpose, four different schemes are deployed (Tab. 1). The results of mean RMSE for these four schemes are

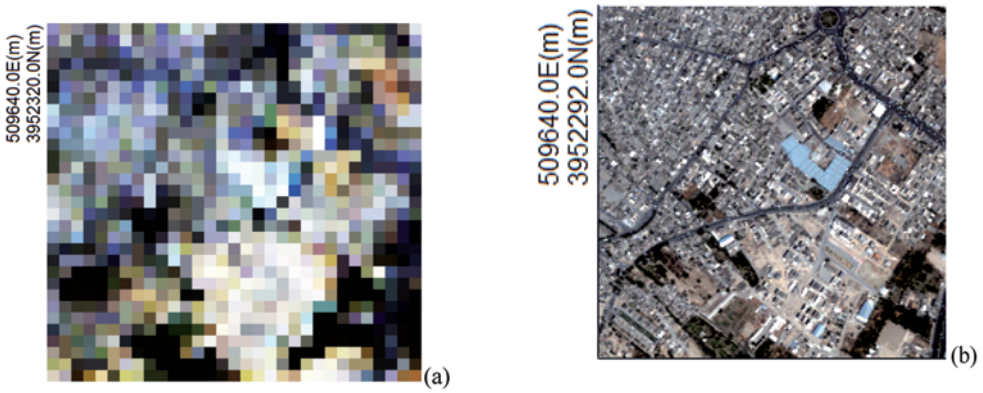


**Fig. 4:** The sample site, (a) Hyperion image (30 m) (30×30 pixels) and (b) IKONOS image (4 m) (219×219 pixels).

**Tab. 1:** The four different proposed schemes.

| Scheme | Detail |
|---|---|
| 1 | IKONOS image classification using K-means algorithm and linear constrained least-square unmixing |
| 2 | IKONOS image classification using K-means algorithm and linear weighted constrained least-square unmixing |
| 3 | IKONOS image classification using Fuzzy C-means algorithm and linear constrained least-square unmixing |
| 4 | IKONOS image classification using Fuzzy C-means algorithm and linear weighted constrained least-square unmixing |

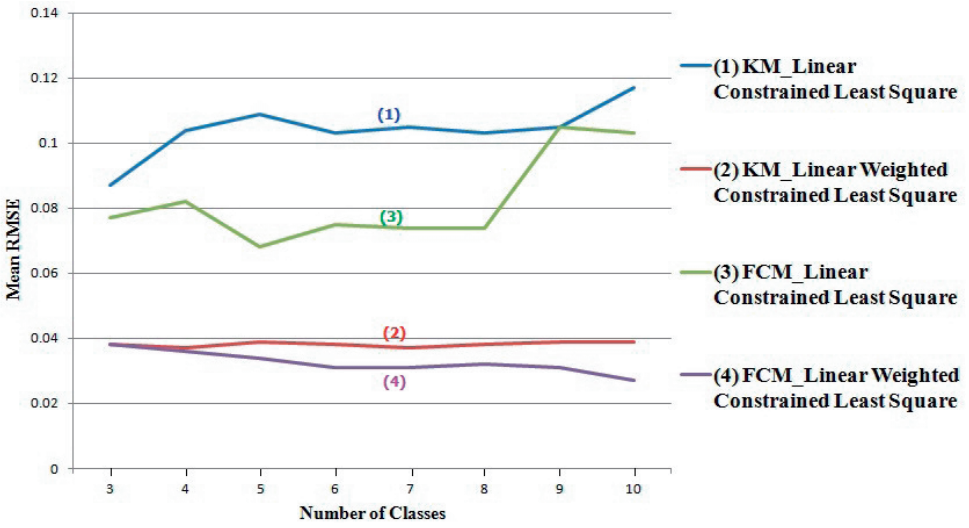


**Fig. 5:** The mean RMSE for four schemes.

shown in Fig. 5. It can be seen that the weighted unmixing performs better compared to unweighted unmixing. In addition, image classification by the Fuzzy C-means algorithm works better compared to the K-means algorithm (Fig. 5). So, the best results are obtained through the 4th scheme.

The classification of CI into six and ten classes has produced minimum mean RMSE (Fig. 5, curve 4). However, it should be noted that this is not a decisive result for the best number of classes in the proposed methodology because the unmixing results may vary for different conditions, like subset dimension, number of candidate reflectance spectra, moving window size and random rules in K-means clustering. Classification of IKONOS image is performed with *nc*=3 to *nc*=20 where *nc*=10 gives a minimum mean RMSE during the constrained unmixing in six runs of the method (Fig. 6). For the number of classes greater

**Tab. 2:** Mean errors (RMSE and R_error) and Mean NCC values between reconstructed and original Hyperion image.

| | |
|---|---|
| 10 | Number of Classes |
| 4 | Maximum number of sub classes |
| [0.008, 0.183, 0.027] | [min, max, mean] RMSE |
| [0.002, 35.21, 5.00] | [min, max, mean] R_Error (%) |
| 0.89 | Mean NCC |

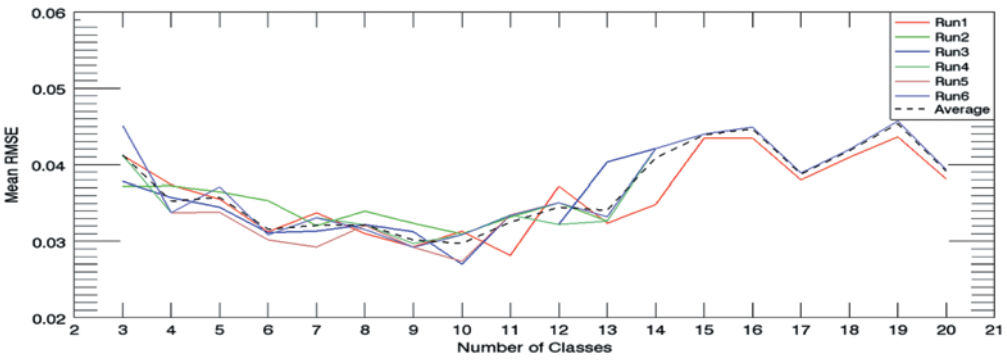


**Fig. 6:** The mean RMSE for the 4th scheme.

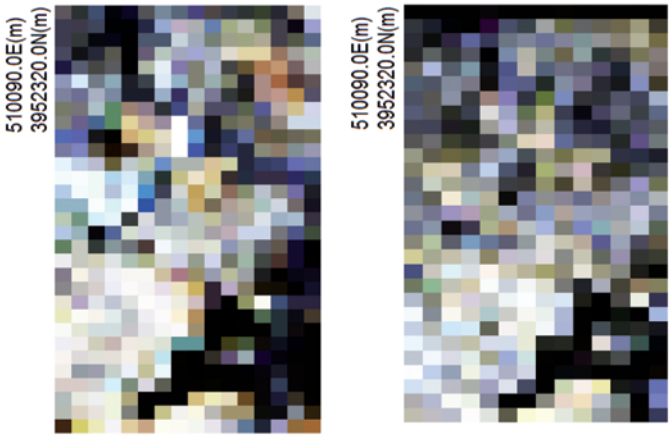


**Fig. 7:** (a) Original Hyperion (30 m); (b) reconstructed Hyperion (30 m).

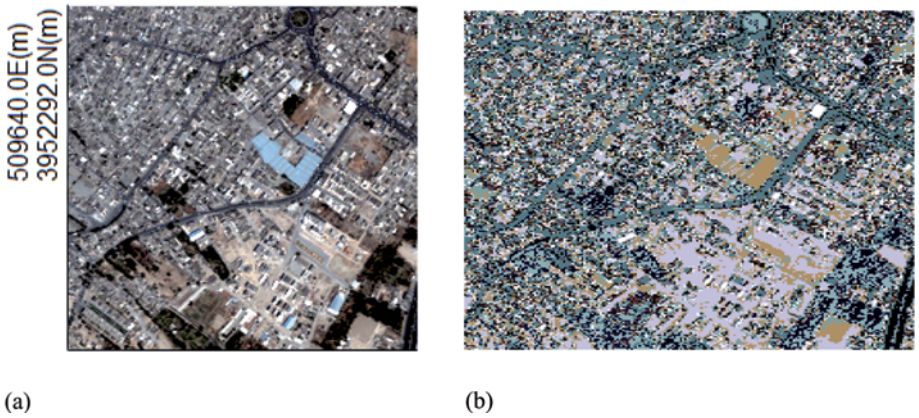


**Fig. 8:** (a) IKONOS image (4 m); (b) fused image (4 m).

than 9, an increase in the window size corresponds to an increase in the amount of error (Fig. 6) all due to the fact that the larger windows may have more land cover variability.

According to section 3.4, the Hyperion image is reconstructed for VI using defined candidate reflectance spectra form UI (Fig. 7). The range and mean errors (RMSE and R_error) and mean NCC values between reconstructed and original Hyperion image are depicted in Tab. 2. The results indicate that the SEHR approach is successful in retrieving urban class reflectance from the Hyperion image.

The fused image has the property of a hyperspectral image with 136 bands as well as a high spatial resolution image with 4 m pixel size (Fig. 8). It is important to notice that the accuracy of the results is influenced by the preprocessing steps. The Hyperspectral image was geo-referenced using a mathematical polynomial model. The geo-referencing results were showing a RMSE near 0.2 pixel size, i.e. 6 m. This error caused a misallocation in the fused image of about 2 pixels considering the spatial resolution of IKONOS image (4 m) and probably bad representation of the fused image due to this mis-registration. Also, the quality of the fused image is impacted by the quality of the reflectance values of the CI that is mentioned in section 3.5.

## 6 Conclusions

In this paper, a new approach (SEHR) for spectral enrichment of high spatial resolution images such as IKONOS was suggested. Four different schemes were designed and tested to retrieve surface spectral reflectance based on spatial unmixing processes. The technique was performed using Hyperion and IKONOS image data.

The estimated values for the spectral reflectance were evaluated by comparing the original mixed pixels to the reconstructed ones. The results showed that the IKONOS classification works better if Fuzzy C-means algorithm and linear weighted constrained least square unmixing were deployed compared to other schemes. Then, the retrieved class reflectance spectra were used to fuse a 30 m resolution hyperspectral image with 136 bands (Hyperion data) with a 4 m resolution multispectral image (IKONOS data). The fusion of the Hyperion with IKONOS datasets can be considered as a powerful technique to differentiate land cover classes. It was also found that, regardless of characteristics of different images, fusion can be carried out in feature level as well. Although SEHR was designed for IKONOS MS and Hyperion data, it can be applied to any two sets of image data. Output of this approach can be used to identify land covers, developing a spectral library of urban material, urban air pollution monitoring, exploring the parameters affecting urban reflectance changes and energy flows.

## Acknowledgements

The authors wish to thank the Remote Sensing Department of K.N. Toosi University of Technology for their suggestions and support in the development of this study. Also, the authors would like to thank the anonymous reviewers for their comments on the manuscript. We also offer our appreciation to the National Cartographic Center of Iran and the User Services USGS for providing remotely sensed data.

## References

Amoros-Lopez, J., Gomez-Chova, L., Guanter, L., Alonso, L. & Moreno, J., 2010: Multi-Resolution Spatial Unmixing for MERIS and LANDSAT Image Fusion. – IGARSS: 3672–3675.

Amoros-Lopez, J., Gomez-Chova, L., Alonso, L. & Guanter, L., 2011: Regularized Multiresolution Spatial Unmixing for ENVISAT/MERIS and Landsat/TM Image Fusion. – IEEE Geoscience and Remote Sensing Letters **8:** 844–848.

Barry, P., 2001: EO-1/ Hyperion Science Data User's Guide.

Bezdek, J., 1981: Pattern Recognition With Fuzzy Objective Function Algorithms. – New York, Plenum.

Bieniarz, J., Cerra, D., Avbelj, J., Reinartz, P. & Muller, R., 2011: Hyperspectral Image Resolution Enhancement Based On Spectral Unmixing And Information Fusion. – ISPRS **XXXVIII**-4/W19.

Busetto, L., Meroni, M. & Colombo, R., 2008: Combining medium and coarse spatial resolution satellite data to improve the estimation of

sub-pixel NDVI time series. – Remote Sensing of Environment **112:** 118–131.

Chang, C.I., 1999: Spectral information divergence for hyperspectral image analysis. – Geoscience and Remote Sensing Symposium, IGARSS **99**.

Haertel, V.F. & Shimabukuro, Y. E., 2005: Spectral Linear Mixing Model in Low Spatial Resolution Image Data. – IEEE Transactions on Geoscience and Remote Sensing: 2555–2562.

Herold, M., Gardner, M., Hadley, B. & Roberts, D., 2002: The Spectral Dimension in Urban Land Cover Mapping from Highresolution Optical Remote Sensing Data. – **3rd** Symposium on Remote Sensing of Urban Areas. Istanbul, Turkey.

MacQueen, J.B., 1967: Some Methods for classification and Analysis of Multivariate Observations. – **5th** Berkeley Symposium on Mathematical Statistics and Probability: 281–297, University of California Press.

Mezned, N. & Abdeljaoued, S., 2009: Unmixing Based Landsat ETM+ and ASTER Image Fusion For Hybrid Multispectral Image Analysis. – Advances in Geoscience and Remote Sensing: 407–418.

Mobasheri, M.R. & Ghamary Asl, M., 2011: Classification by diagnosing all absorption features (CDAF) for the most abundant minerals in airborne hyperspectral images. – EURASIP Journal on Advances in Signal Processing **102:** 1–7.

Powell, R.L., Roberts, D.A., Dennison, P.E. & Hess, L.L., 2007: Sub-pixel mapping of urban land cover using multiple endmember spectral mixture analysis: Manaus, Brazil. – Remote Sensing of Environment **106:** 253–267.

Staenz, K., Neville, R.A. & Clavette, S., 2002: Retrieval of Surface Reflectance from Hyperion Radiance Data. – IEEE Geoscience and Remote Sensing Symposium IGARSS **3:** 1419–1421.

Taylor, M., 2005: IKONOS Radiometric Calibration and Performance after 5 Years on Orbit. – CALCON 2005 Conference. Logan, Utah.

Zeng, Y., Schaepman, M.E., Wu, B., Clevers, J.G. & Bregt, A.K., 2007: Using Linear Spectral Unmixing Of High Spatial Resolution And Hyperspectral Data For Geometric-Optical Modelling. – ISPRS **XXXVI**/7-C50.

Zhukov, B., Oertel, D., Lanzl, F. & Reinhackel, G., 1999: Unmixing-Based Multisensor Multiresolution Image Fusion. – IEEE Transactions on Geoscience and Remote Sensing: 1212–1226.

Zhang, Y., 2002: Problems in the fusion of commercial high-resolution satellite as well as Landsat 7 images and initial solutions. – ISPRS, Commission IV, WG VII/7.

Zurita-Milla, R., Clevers, J.G. & Schaepman, M.E., 2008: Unmixing-Based Landsat TM and MERIS FR Data Fusion. – IEEE Geoscience and Remote Sensing Letters: 453–457.

Zurita-Milla, R., Kaiser, G., Clevers, J. & Schneider, W., 2009: Downscaling time series of MERIS full resolution data to monitor vegetation seasonal dynamics. – Remote Sensing of Environment **113:** 1874–1885.

Address of the authors:

Fakhereh Alidoost, M.Sc Remote Sensing, Tel.: +98-91-98667532, e-mail: f.alidoost@sina.kntu.ac.ir

Mohammad R. Mobasheri, Ph.D. Associate Professor, Tel.: +98-91-21226630, e-mail: mobasheri@kntu.ac.ir

Ali A. Abkar, Ph.D. Assistant Professor, Tel.: +98-91-21403827, e-mail: abkar@ kntu.ac.ir

Remote Sensing Department, Faculty of Geodesy and Geomatics, K.N. Toosi University of Technology, Tehran, P.O. Box: 15875-4416, Iran, Fax: +98-21-88770213.

Manuskript eingereicht: Juni 2012
Angenommen: September 2012

PFG 2013 / 1, 0043–0052
Stuttgart, February 2013

Report

# Federated Catalogue for Discovering Earth Observation Data

Yuanzheng Shao, Liping Di, Fairfax, VA, USA, Yuqi Bai, Beijing, China, Lingjun Kang, Huilin Wang, Fairfax, VA, USA & Chao Yang, Wuhan, China

**Keywords:** earth observation, federated catalogue, mediator-wrapper architecture, geospatial data discovery, CEOS WGISS Integrated Catalogue

**Abstract:** As Earth observation (EO) technologies develop continuously, the volumes of geospatial data archived in data centers also grow. Those geospatial data can be used in many scientific fields such as agriculture, land use and climate change. The complex features and massive amounts of EO data bring challenges on how to make better use of these data for the community and for public service. Most of legacy data center distribute the data through individual catalogue, and use heterogeneous query interface and metadata model. To find the data of interest from multiple data source for multi-disciplinary research, the scientists and data users need to handle different query languages and metadata models. To facilitate Earth observation data discovery for researchers, this paper proposes a federated catalogue to integrate multiple legacy data centers. By analysing existing data discovery mechanism, mediator-wrapper framework was adopted to implement catalogue federation. By solving the query interface translation and metadata model conversion between federated catalogues and individual data centers, a system – The CEOS WGISS Integrated Catalogue (CWIC) was implemented. CWIC was proved to be an effective tool to discovery geospatial data from multi-source data centers by interacting with standardized query interface and metadata model. The architecture and approaches proposed in this paper can be used to establish a federated catalogue system for different communities.

**Zusammenfassung:** *Konzept für einen Zentralkatalog für Fernerkundungsdaten.* Mit dem fortschreitenden Ausbau der Erdbeobachtung steigen auch die zu archivierenden Datenmengen. Die Daten finden in den Geowissenschaften vielfältig Verwendung, z. B. in der Landwirtschaft, beim Monitoring von Landnutzungsänderungen und beim Klimawandel. Die komplexe Datenstruktur und die riesigen Datenmengen sind eine Herausforderung an die geeignete Bereitstellung für private und öffentliche Zwecke. Die meisten staatlichen Datenzentren bieten ihre Daten über eigene Kataloge und sehr unterschiedliche Benutzerschnittstellen und Metadatenmodelle an. Für fächerübergreifende Untersuchungen müssen die Benutzer unterschiedliche Abfragesprachen einsetzen. Zur Vereinfachung wird daher in diesem Artikel ein Konzept für einen Zentralkatalog für die übergreifende Suche in vielen Datenzentren vorgestellt. Nach der Analyse verschiedener vorhandener Lösungen wurde das „Mediator-Wrapper“-Modell für den Zentralkatalog zu Grunde gelegt. Der Zentralkatalog wurde als „CEOS WGISS Integrated Catalogue (CWIC)“ implementiert, nachdem die Transformation der Abfragen (queries) und der Metadaten in eine standardisierte Form gelöst war. Inzwischen hat der CWIC seine Leistungsfähigkeit für katalogübergreifende Abfragen unter Beweis stellen können. Die in diesem Artikel vorgestellte Architektur kann zur Einrichtung von Zentralkatalogen auch in anderen Communities empfohlen werden.

## 1 Introduction

As the development of Earth observation technology progresses, more and more geospatial data used for scientific research are available from various geospatial agencies and government departments. Those geospatial data could be used in many scientific fields such as agriculture, land use and climate change. To find the data of interest from multiple data sources for multi-disciplinary researches, the scientists and data users need to get familiar


www.schweizerbart.de
DOI: 10.1127/1432-8364/2013/0157
1432-8364/13/0157 $ 2.50

with the individual data center and the corresponding web portal. Most of data centers require data users to register an account before searching and acquiring data, which require data users to maintain many user account information for every data center. For some archived data without online access URLs, the users need to place an order against specific data center and get the notification of data access URLs from registered email. Such work is very time-consuming and tedious, especially when the catalogues use different metadata models and catalogue interface protocols (Bai et al. 2007). Moreover, this human-computer interaction of data discovery brings more challenges for data users to build an automatic workflow for some scientific research.

To solve such challenge, it is highly required to build an integrated catalogue, also known as catalogue federation, to conduct the data discovery in a consistent way. This federated catalogue, by solving the inconsistency among multiple data centers, presents a standardized data query interface and metadata model. With the catalogue federation, data user only needs to interact with the federated catalogue to find data of interest other than working with different catalogues. This paper proposes a solution for a geospatial catalogue federation, which integrates some major legacy catalogues, to facilitate geospatial data discovery.

In order to implement a federated catalogue for geospatial data discovery, the mediator-wrapper (Wiederhold 1992) architecture was selected. This architecture has been widely used for the integrated and universal access to multiple, autonomous information sources. Distributed data sources (legacy data center) archive data and distribute them through the Internet. Such architecture has been successfully used in many research areas, such as integration of GIS data source (Stoimenov et al. 2000), digital libraries (Melnik et al. 2000), intelligent web application (Sahuguet & Azavant 2001), and XML data (Baru et al. 1999, Lin et al. 2000).

Song et al. (2006) designed a grid-enabled information integration system which can access heterogeneous and distributed data sources through the standard interface of grid computing. Stoimenov et al. (2000) provided intelligent integration of information using mediation technology, which is used for the integration of spatial data from geographic information system (GIS) databases with alphanumerical data from relational database management systems and other data sources. Hidalgo et al. (2006) described a cost model that stores values from a complete set of web source-focused parameters obtained by the web wrappers in a mediator-wrapper environment. Based on a mediator-wrapper approach, Corcho et al. (2003) designed a framework which supports an integrated view over multiple heterogeneous sources for e-commerce application. Miller & Nusser (2003) presented an infrastructure model which is based on a spatial mediator that takes metadata on the information needs of the user, data sources and tools available, as well as device characteristics (in field settings) into consideration when processing the user's request.

Most of the previous work about data discovery focused on Earth observation retrieval. Geospatial metadata, as an important and effective way to help data users to understand the retrieved data, usually attracted little attention. This paper uses the generic metadata model – ISO 19115:2003 (Geographic information – Metadata) – to describe the data granules returned from a federated catalogue. The architecture, global query interface and metadata model proposed in this paper are used by the Working Group on Information Systems and Services (WGISS) of the Committee on Earth Observation Satellite (CEOS) (WGISS 2012), and are proved to be useful for catalogue federation in Earth observation community.

The rest of this paper is structured as follows. Section 2 introduces and compares some major existing data centers and their data discovery mechanism, including their data distribution policies, query interface and metadata model. Section 3 analyses the challenges and proposes solutions to coordinate different data discovery mechanisms, including query interface and metadata model selection. Section 4 presents the federated catalogue architecture and the implementation of the CWIC system. The conclusion and discussion are drawn in section 5.

## 2 Existing Data Discovery Mechanism

There are some major data centers worldwide which archive massive and heterogeneous geospatial data. This paper focuses on the following seven legacy geospatial catalogues: the NASA EOS ClearingHOuse (ECHO), the NOAA's Comprehensive Large Array-data Stewardship System (CLASS), U.S. Geology Survey (USGS) – Landsat Catalogue System, the Brazil National Institute for Space Research (INPE) catalogue, the China Academy of Opto-Electronics (AOE) catalogue, the Japan Aerospace Exploration Agency (JAXA) and the Group for High-Resolution Sea Surface Temperature (GHRSST) catalogue. All of those data centers have already provided a web portal or a service to enable data user to discover data of interest. The following part of this chapter will analyze the data discovery mechanism of some of them, and pay more attention to the comparison of query interface and metadata model.

### 2.1 *NASA ECHO Data Catalogue*

The NASA-developed Earth Observing System (EOS) Clearinghouse (ECHO) is a spatial and temporal metadata registry and order broker built by NASA's Earth Science Data and Information System (ESDIS) that enables the science community to more easily use and exchange NASA's data and services (ECHO 2012).

1) Data query interface: ECHO developed a query language, named IIMSAQL, to enable the query on collection-level and granule-level in the ECHO system. This is an XML-based language with a detailed DTD definition. IIMSAQL defined the element for specifying collection identifier, spatial extent, temporal range, data center identifier, and many other features, such as Percentage of Cloud Cover, of the data center and collection.
2) Metadata Conceptual Model: the ECHO's metadata conceptual model is named as ECHO Earth Science Metadata Conceptual Model (EESMCM). It is developed from the EOSDIS Core System (ECS) Science Data Model. This metadata model is used to describe collection and granule. In the ECS, a granule is the smallest unit of data that is independently described and taken stock, while a collection represents a logical grouping of granules. Each Collection is identified with an Earth Science Data Type (Wei et al. 2007).

### 2.2 *NOAA CLASS Data Catalogue*

The CLASS system is an electronic library of NOAA environmental data. This web site provides capabilities for finding and obtaining those data. CLASS provides more than 70 data collections. The data archived in CLASS system do not have an online access URL, so the client has to register an account with email address, and the query response containing access URLs will be sent to the specified email address. Beside the web site, NOAA Enterprise Archive Access Tool (NEAAT) is also developed by NOAA to enable data query through an Application Programmer Interface. NEAAT is an access API designed to integrate various heterogeneous NOAA data systems for the purposes of data discovery and retrieval.

1) Data query interface: NEAAT supports a number of query types for both catalogue- and inventory-level. Both simple queries and compound quires are supported. There are four comparisons implemented in NEAAT API: string, algebraic, temporal and spatial. NEAAT provides Java Archive (JAR) files which expose many easy-to-use functions. Data clients need to call the corresponding function to specify query parameters and execute a data inventory query.
2) Metadata Conceptual Model: the CLASS system defines a very simple XML model to encode the returned data granule. NEAAT contains limited metadata about returned granule, but the basic spatial extent, temporal range, platform and data size information are included.

### 2.3 *USGS Landsat Data Catalogue*

LandSAT data has wide use in geospatial-related scientific research. The USGS offers all users the entire Landsat 1–5 and 7 archive

data at no charge using a standard data product recipe. The user can discover Landsat data through several web portals, such as EarthExplorer, GloVis and GeoBrain. Based on these portals, data users could discover and access all types of Landsat data.

1) Data query interface: the USGS releases a Web API which could be used to discover Landsat data. The access URL for this Web API is as follows: *http://edcsns17.cr.usgs.gov/EE/InventoryStream/latlong?* Some simple parameters could be specified in the data query request of the Web API, including collection identifier, spatial bounding box, temporal range and the number of returned records.
2) Metadata Conceptual Model: A simple XML model is defined to describe the response from the USGS Landsat catalogue. The response from the USGS Landsat catalogue includes information like browser image URL, data ordering URL, platform, cloud cover rate and spatial-temporal information.

### 2.4 *China AOE Data Catalogue*

China has launched several EO satellites, such as the CBRES series, the FengYun series and so on. The data products generated from those satellites have been widely applied to the field of agriculture and other fields. The EO data have good catalogue and archive systems in several satellite data centers (Feng et al. 2011).

To facilitate data discovery for those EO data, the AOE of the Chinese Academy of Science designed and developed an OGC Catalogue Service for the Web (CSW). AOE CSW adopts the OGC CSW standard as the query interface, and the ISO 19115 standard to describe metadata.

### 2.5 *JAXA Data Catalogue*

JAXA is an independent administrative institution to be able to perform all activities in the aerospace field as one organization, from basic research and development to utilization. JAXA has archived a huge amount of Earth observation data products, such as the Advanced Land Observation Satellite (ALOS), the Greenhouse gases Observing SATellite (GOSAT) and the Advanced Earth Observing Satellite (ADEOS). JAXA provides the Earth Observation Satellite Data Search/Order System (JAXA 2012) which facilitates data users to retrieve the archived data through a web portal-based interface.

Besides the web portal, JAXA also developed its CSW service to distribute its archived data based on GeoNetwork and deployed the CSW on Amazon Cloud Computing platform. Both the ebRIM profile and the ISO profile are implemented.

## 3 Challenges to Integrate Different Data Catalogues

Based on the analysis and the comparison in the second section, it is noticeable that heterogeneity exists among those data catalogues. To design and implement a federated catalogue, which aims to integrate different catalogues and provides a universal data discovery mechanism, a global data query language and metadata model should be selected. Moreover, the mapping between the federated catalogue and the individual catalogues also should be established. This chapter will address the challenges in data discovery mechanisms coordination and its solutions.

### 3.1 *Global Query Interface Selection*

In order to implement an integrated catalogue, a global query interface should be adopted. The OpenGIS CSW specification defines three protocol bindings for the catalogue service: Z39.50, CORBA/IIOP and HTTP. In this paper, the OGC CSW version 2.0.2 is implemented. The OpenGIS CSW specification proposes an OGC common catalogue query language, which has to be supported by all compliant OpenGIS catalogue services (Voges & Senkler 2007). This query language supports nested Boolean queries, text comparison operations and temporal-spatial operators. The federated catalogue in this paper implements the OGC Filter specification (Vretanos 2010).

The heterogeneity feature of query interfaces of different data catalogues brings challenges to determine queryables of a global query interface. To translate the query language from a global to a native query interface, the federated catalogue has to solve the following problems:

1) Asymmetry of metadata queryables: the queryables defined in the global query language may not have the corresponding one in a legacy data catalogue. The queryables supported by different data centers also are various. For example, NASA ECHO query API supports the granule query against cloud cover rate, but other data centers do not support such query. To solve the asymmetry of metadata queryables, the federated should select the minimal subset of all queryables implemented among different data centers. By analysing those legacy catalogues, the dataset identifier, spatial bounding box and temporal range query parameters are selected as the mandatory queryables of a federated catalogue, which are also the most important attributes of geospatial data.
2) Heterogeneity of query formats: as described in section 2, those legacy data catalogues have different query interfaces and formats. For example, NOAA CLASS uses native NEAAT API package, USGS and INPE accepts Web API query format, while ECHO only accepts IIMSAQL format. Even for the catalogues implementing a CSW service, such as AOE, JAXA and GHRSST, the queryables name for the same metadata object may also be different. To solve the heterogeneity of query formats, a federated catalogue has to translate the queryables and query format from a global query language to the corresponding query language supported by an individual data catalogue.

The HTTP protocol is selected as the protocol binding, and both HTTP GET and HTTP POST methods are implemented. The following operation shall be implemented based on the CSW specification.

GetCapabilities: this mandatory operation allows CSW clients to retrieve service metadata from a server. The response of GetCapabilities request shall be an XML document containing service metadata about the server.

DescribeRecord: this mandatory operation allows a client to discover elements of the information model supported by the target catalogue service. The operation allows some or the entire information model to be described.

GetDomain: this optional operation is used to obtain runtime information about the range of values of a metadata record element or a request parameter. The runtime range of values for a property or a request parameter is typically much smaller than the value space for that property or parameter based on its static type definition.

GetRecords: this mandatory operation is used to search the catalogue content. It supports not only requesting metadata records at different levels of detail (full, summary, and brief) and in different output schemas, but also allows for paging and sorting, as well as stating the filter criteria in different query languages.

GetRecordById: this mandatory operation retrieves the default representation of a catalogue records using their identifier. The records identifier could be retrieved from the GetRecords response.

## 3.2 *Global Metadata Model Selection*

The existing data centers adopted different metadata models to describe their archived data. In order to provide a universal metadata schema to describe data returned from all catalogue, it is necessary to define a global metadata model for a federated catalogue, and build the mapping from individual metadata model to the global one.

Geographical information – Metadata (ISO 19115) and its extension for imagery and gridded data (ISO 19115-2), which define comprehensive and detailed elements to describe geospatial data, are widely used in the Earth observation field (ISO 2003). Some software packages, such as GeoNetwork and ESRI GeoPortal, have overall support of the ISO 19115 metadata model. In this paper, ISO 19115 is selected as the global metadata model for the federated catalogue.

Some legacy catalogues, such as GHRSST, AOE and JAXA have already implemented the CSW service and fully support the global metadata model. For such data center, federated catalogue does not need to make any conversion for the returned metadata. But for the data center with a customized metadata model, such as the ECS model defined in ECHO, the federated catalogue has to convert the metadata from their native schema to a global one.

Since the richness of the metadata returned from different catalogues is also various, the asymmetry of the metadata model is becoming another challenge to implement a catalogue federation. The asymmetry features are expressed in two aspects: some metadata items in a legacy data center cannot be mapped to corresponding elements in a global metadata model; some mandatory elements in the global metadata model cannot find the corresponding elements in the response of a legacy catalogue. For the first problem, the current solution is to ignore the elements that cannot be mapped to global metadata. For the latter problem, the a priori knowledge is used to fill the mandatory elements in the global metadata. Taking NASA ECHO as example, the point of contact information are required in ISO 19115 metadata, but the XML response returned from ECHO does not include any contact information. For such situation, we can find the point of contact information from the NASA Distributed Active Archive Centers (DAAC) or their web portal, and fill that information to mandatory element of global metadata.

## 4 Federated Catalogue Implementation

### 4.1 *System Architecture Design*

The mediator-wrapper architecture is used to design the federated catalogue. As shown in Fig. 1, data is archived in heterogeneous models and disseminated through different interfaces to the data sources. The wrapper layer tackles the heterogeneity through providing a universal querying interface (i.e. OGC CSW) and an intermediate information model, i.e. Dublin Core, ISO 19115. Mediator, on the other hand, acts as a proxy accepting the query from data users, dispatching the request to corresponding wrapper, assembling the query results from individual data center and returning it to the data users.

Specifically, the interactions among the user, mediator, and wrapper are summarized as follows:

1) The data client queries against mediator through the OGC CSW interface.
2) The mediator parses the query and dispatches it to a related wrapper.

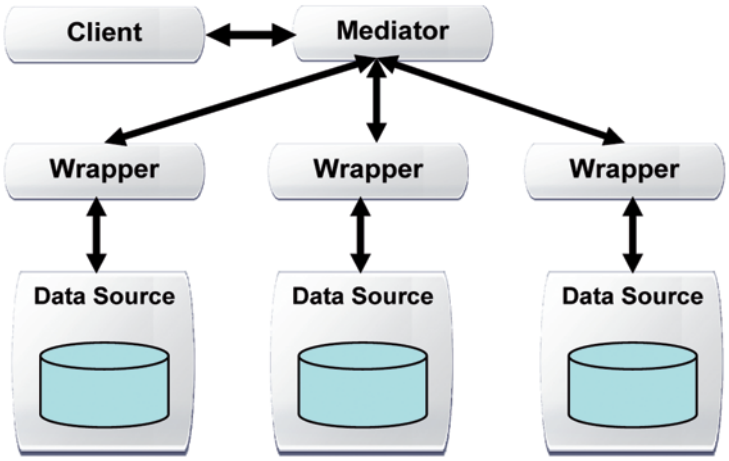


**Fig. 1:** The mediator-wrapper architecture.

3) The wrapper converts the request to a local query language and queries against a data catalogue. After getting a response, the wrapper converts the response to an intermediate information model and returns it to the mediator.
4) The mediator sends the response to the data users.

### 4.2 *CEOS WGISS Integrated Catalogue*

The Committee on Earth Observation Satellite (CEOS) is the international inter-agency organization addressing the coordination of the satellite EO programs of the world's governmental space agencies. The Working Group on Information Systems and Services (WGISS) is a subgroup of CEOS, which aims at promoting collaboration in the development of systems and services that manage and supply EO data to users world-wide. With the initiation by NOAA and NASA, WGISS started the CWIC project in 2010, aiming at creating a federated catalogue system for providing inventory-level search to catalogue systems of all major CEOS members around the world through a standard-based unified interface.

The architecture, query interface and metadata model proposed in the previous section are used in the project of CWIC. CWIC is designed to provide a single access point for the major CEOS agency catalogue systems (Di et al. 2012).

As of August 2012, seven data catalogues described in section 2 have been integrated in the CWIC service. The framework of CWIC system is shown in Fig. 2, and the interaction between major modules within this framework is presented in Fig. 3.

The harvest operation is not implemented in the CWIC service, but the following operations, defined in OGC CSW specification, have been implemented and introduced in section 3.1. They are the operations GetCapabilities, DescribeRecord, GetDomain, GetRecords and GetRecordById.

To support a query interface translation, the mapping between OGC CSW query interface and the local query interfaces is established. At the wrapper level, all queries dispatched from the mediator will be translated to a native query interface. For example, the query about an ECHO dataset will be translated to the IIMSAQL language. Regarding the metadata model conversion like query interface the mapping between the ISO 19115 and the metadata model used in legacy catalogues is also created. The issue that needs to be solved during the conversion is the asymmetry feature of different metadata.

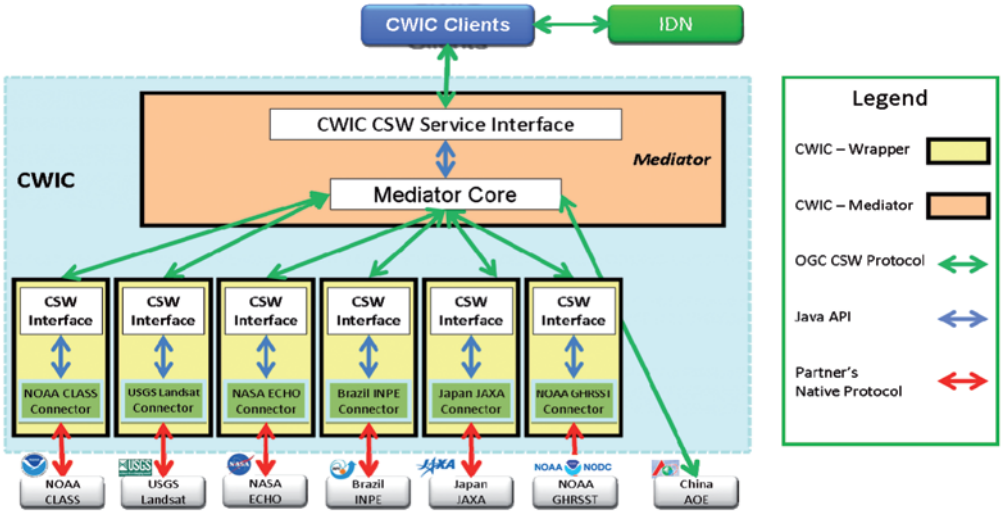


**Fig. 2:** The framework of CEOS WGISS Integrated Catalogue.

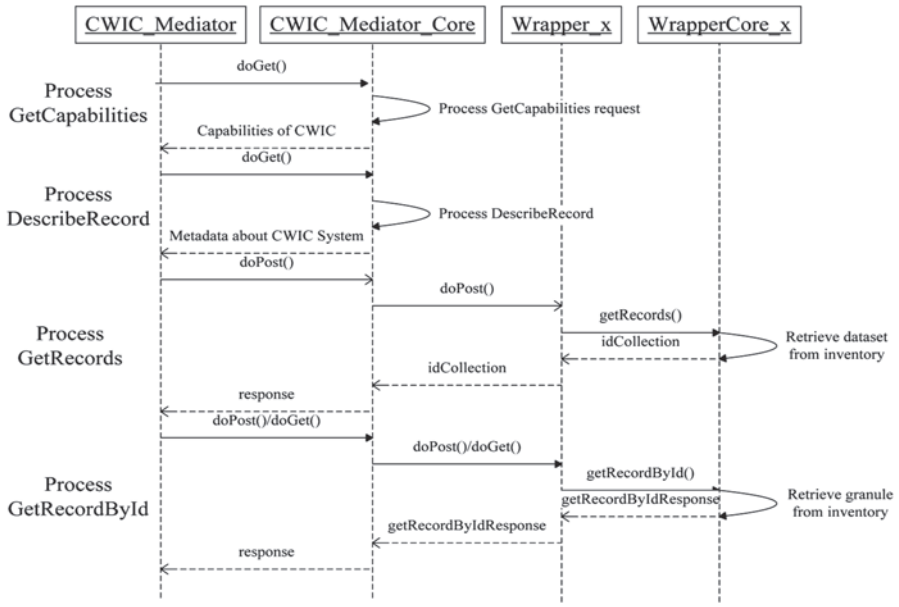


**Fig. 3:** Interaction between major modules of CWIC.

CWIC is supposed to provide more enriched information in its query response. For some data catalogues with overloaded information, the original response contains so much information but some of them cannot find matched elements in global metadata schema. But for some data catalogues, the query response just includes very limited information. To fix the issues of overloaded information, CWIC creates a mapping table to put more information from native metadata to global metadata. For a native response with limited information, CWIC imports pre-defined attributes or a priori knowledge for some mandatory elements such as dataset identifier and point of contact in the global metadata model.

### 4.3 *CWIC servable Datasets*

The entire federated catalogue of CWIC has registered their dataset information into the Global Climate Master Directory (GCMD) (GCMD 2012). Each dataset will be assigned to an individual Directory Interchange Format (DIF) Entry ID and label the dataset with CWIC attributes. The DIF Entry ID is used as the dataset identifier in the GetRecords and GetRecordById query of CWIC.

By interacting with the GCMD CSW interface, data users could get the collection identifier based on free text search and other search options provided by GCMD. Besides interacting with GCMD, data user can also retrieve all servable collection identifiers from CWIC capabilities document by sending GetCapabilities request. Once getting the collection identifier, data users and clients could build the request payload by specifying other temporal-spatial query parameters and post the GetRecords request to CWIC service. In the back end of CWIC, there is a configuration file which maintains the dataset identifier and its corresponding wrapper URL. The CWIC mediator dispatches the request to a proper wrapper based on this configuration file.

## 5 Conclusion and Discussion

This paper discusses the design and the implemention of a federated geospatial catalogue system that provides a single standard interface for inventory-level searches of data

archived in major CEOS member agencies. The CWIC system has successfully integrated seven data catalogues: NOAA CLASS, USGS Landsat, NASA ECHO, Brazil INPE, JAXA, NODC/GHRSST and China AOE. Within the CWIC, data user queries and retrieves data from heterogeneous data catalogues through universal interface and data model. Based on CWIC, more and more clients emerge to discover Earth observation data in the standard way from multiple heterogeneous data centers. For example, some representative clients including GMU GeoBrain, USGS LSI portal, NASA CWIC-Start and Canada CCRS. It is expected that more CWIC clients, especially domain-specific ones, will be developed by the EO communities.

Three conclusions are drawn from the design and implementation of CWIC: (1) the mediator-wrapper architecture is suitable for creating a federated catalogue system, (2) OGC CSW can be used as a universal query interface in catalogue federation, and (3) ISO 19115 and ISO 19115-2 effectively act as the standard metadata information model for such a federated geospatial catalogue system. Both the architecture and the approaches proposed in this paper are also applicable to tackle a heterogeneous problem in other communities for resource discovery.

CWIC does not adopt the caching or harvesting of the metadata from remote catalogues to improve the query performance. So currently the query performance highly depends on remote catalogue. As to the search capabilities, in order to present a universal query interface, CWIC only kept the lowest common queryables, which leads to the problem that some useful query parameters in native catalogue are unsupported in CWIC. In the current version of CWIC, the common queryables (spatial extent, temporal range, and dataset identifier) are sufficient to fulfil the demand from a client.

In the next version 2.0 of the CWIC system, more catalogue systems of CEOS member will be integrated into CWIC system. Moreover, CEOC WGISS query language will be implemented to provide more flexible query capabilities. Besides the common queryables, more native queryables will be supported in future version.

## Acknowledgements

This work is supported mainly by a grant from NOAA. The authors would like to thank the CEOS WGISS CWIC task team as well as scientists of individual CEOS member agencies for their review and comments on the CEOS architectures, information models, and implementation details, and for their testing of the CWIC version 1. The authors would especially acknowledge the contributions from teams of the current seven CWIC member catalogue systems and the NASA GCMD/IDN team during the implementation of CWIC version 1.

## References

Bai, Y., Di, L., Chen, A., Liu, Y. & Wei, Y., 2007: Towards a Geospatial Catalogue Federation Service. – Photogrammetric Engineering & Remote Sensing **73** (6): 699–708.

Baru, C., Gupta, A., Ludäscher, B., Marciano, R., Papakonstantinou, Y., Velikhov, P. & Chu, V., 1999: XML-Based information mediation with MIX. – ACM SIGMOD International Conference on Management of Data: 597–599, Philadelphia, Pennsylvania, USA.

Corcho, O., Gomez-perez, A., Leger, A., Rey, C. & Toumani, F., 2003: An Ontology-Based Mediation Architecture for E-Commerce Applications. – Proceedings of Intelligent Information Systems: 477–486, Zakopane, Poland.

Di, L., Bai, Y., Shao, Y., Wang, H., Kang, L., Warnock, A., Yapur, M. & Enloe, Y., 2012: A Global Earth Observation Data Discovery System – the CEOS WGISS Integrated Catalog. – IEEE Geoscience and Remote Sensing Society, in press.

ECHO, 2012: EOS Metadata Clearinghouse (ECHO), http://earthdata.nasa.gov/about-eosdis/system-description/eos-metadata-clearing-house-echo (10.6.2012).

Feng, L., Wang, C., Li, C. & Deng, Z., 2011: Catalogue system integration of China EO data for CWIC system. – **19th** International Conference on Geoinformatics: 1–4, Shanghai, China.

GCMD, 2012: Earth Science data and services directory: Global Change Master Directory. – http://gcmd.nasa.gov/, NASA (30.8.2012).

Hidalgo, J., Pan, A., Álvarez, M. & Guerrero, J., 2006: Efficiently Updating Cost Repository Values for Query Optimization on Web Data Sources in a Mediator/Wrapper Environment. – Lecture Notes in Computer Science: 1–12.

ISO, 2003: ISO 19115: Geographic information – Metadata. – http://www.iso.org/iso/iso_cata-

logue/catalogue_tc/catalogue_detail.htm?csnumber=26020 (30.8.2012).

JAXA, 2012: Observation/Research Result Databases. – http://www.jaxa.jp/archives/db/index_e.html, Japan Aerospace Exploration Agency (30.8.2012).

Lin, H., Risch, T. & Katchaounov, T., 2000: Object-oriented mediator queries to XML data. – **First** International Conference on Web Information Systems Engineering: 39–46, Hong Kong, China.

Melnik, S., Garcia-Molina, H. & Paepcke, A., 2000: A mediation infrastructure for digital library services. – **5th** ACM conference on Digital libraries: 123–132, San Antonio, Texas, USA.

Miller, L. & Nusser, S., 2003: An Infrastructure for Supporting Spatial Data Integration. – Federal Committee on Statistical Methodology Conference: Arlington, Virginia, USA.

Sahuguet, A. & Azavant, F., 2001: Building intelligent Web applications using light weight wrappers. – Data & Knowledge Engineering **36** (3): 283–316.

Song, J., Yoo, S., Park, C., Choi, D. & Lee., Y., 2006: The Design of a Grid-enabled Information Integration System Based on Mediator/Wrapper Architectures. – 2006 International Conference on Grid Computing & Applications: 114–120, Las Vegas, Nevada, USA.

Stoimenov, L., Djordjevic-Kajan, S. & Stojanovic, D., 2000: Integration of GIS data sources over the Internet using mediator and wrapper technology. – **10th** Mediterranean Electrotechnical Conference: 334–336, Lemesos, Cyprus.

Voges, U. & Senkler, K., 2007: OpenGIS Catalogue Services Specification 2.0.2 – ISO Metadata Application Profile (07-045). – http://www.opengeospatial.org/standards/cat, OpenGIS (10.6.2012).

Vretanos, P., 2010: OpenGIS Filter Encoding 2.0 Encoding Standards (OGC 09-026r1 and ISO/DIS 19143). – http://www.opengeospatial.org/standards/filter, OpenGIS (30.8.2012).

Wei, Y., Di, L., Zhao, B., Liao, G. & Chen, A., 2007: Transformation of HDF-EOS metadata from the ECS model to ISO 19115-based XML. – Computers & Geosciences **33** (2): 238–247.

WGISS, 2012: WGISS Information Systems. – http://wgiss.ceos.org, CEOS WGISS (10.6.2012).

Wiederhold, G., 1992: Mediators in the architecture of future information systems. – IEEE Computer **25** (3): 38–49.

Addresses of the authors:

Dr. Yuanzheng Shao, Dr. Liping Di, Lingjun Kang, Huilin Wang, Center for Spatial Information Science and Systems, George Mason University, 10519 Braddock Road Suite 2900, Fairfax, VA 22032, USA, e-mail: {yshao3}{ldi}{lkang3}{whuilin}@gmu.edu

Dr. Yuqi Bai, Tsinghua University, 1 Qinghuayuan Road, Haidian District, Beijing 100084, China, e-mail: yuqibai@gmail.com

Chao Yang, Wuhan University, 129 Luoyu Road, Wuhan, Hubei 430079, China, e-mail: cyang9@gmu.edu

Manuskript eingereicht: September 2012
Angenommen: Oktober 2012

# Berichte von Veranstaltungen

## 22. ISPRS-Kongress 2012 in Melbourne, Australien, Kommissionsberichte

Der 22. ISPRS Kongress fand vom 25. 8. bis 1. 9. 2012 in Melbourne, Australien, statt und stand unter dem Thema *Imaging a sustainable future*. Wie üblich wurden jeder Kommission eine bestimmte Anzahl an Sitzungen für Vorträge und Posterpräsentationen zugewiesen. Die Auswahl der eingereichten Papers fand kommissionsabhängig auf Basis von vollständigen Papers oder/und mittels eingereichter Abstracts statt. In Abhängigkeit des durchgeführten Begutachtungsprozesses wurden die Beiträge in unterschiedlichen Reihen der ISPRS veröffentlicht. Artikel mit *full paper* review finden sich in den *ISPRS-Annals* (www.isprs.org/publications/annals.aspx) und alle anderen wurden in den *Archives* veröffentlicht (www.isprs.org/publications/archives.aspx).

Die Vorträge während des Kongresses in Melbourne waren von Sonntag bis Samstag auf 6,5 Tage konzentriert, so dass man wegen der Vielfalt und Menge der angebotenen Informationen leider teilweise bis zu 13 Parallelveranstaltungen akzeptieren musste. Dabei kam es auch vor, dass Sitzungen mit gleichem thematischem Bezug unterschiedlichen Kommissionen zugewiesen und teilweise parallel durchgeführt wurden. Diese Überschneidungen hätte man nach Ansicht vieler Teilnehmer durch eine bessere inhaltliche Vortragsprogrammplanung vermeiden können. Die konventionelle Art der Posterpräsentationen wurde revolutioniert: Anstelle ausgedruckter Poster bekamen die Autoren die Gelegenheit, ihre Arbeit in dreiminütigen Kurzvorträgen vorzustellen und anschließend mittels digitaler Bildschirmpräsentationen zu diskutieren. Manchmal wurde man auch enttäuscht, wenn angekündigte Vorträge – insbesondere bei den Kurzpräsentationen – nicht gehalten wurden. Das neue Posterkonzept schaffte zweifelsohne neue interaktive Präsentations- und auch Diskussionsmöglichkeiten. Hinderlich war jedoch die deutlich zu geringe Anzahl an Bildschirmen, so dass eine Reihe von Präsentationen gar nicht oder erst nach längerer Suche besucht werden konnte. Ein Ort für diese Sitzungen mit ausreichend Platz und Möglichkeiten der Präsentationen und dies ggf. über den gesamten Tag an prominenter Stelle des Veranstaltungsortes wäre in Zukunft sicherlich zu begrüßen.

Im Folgenden findet sich eine Kurzberichtesammlung der ISPRS-Berichterstatter der PFG über den ISPRS-Kongress bzw. die zurückliegende Vierjahresperiode.

### Kommission I

Die Beiträge der sechs Arbeitsgruppen in der Kommission I wurden in 16 technischen Sessions und in drei *short-interactive* Sessions vorgetragen. Zusätzlich gab es auch Beiträge in kommissionsübergreifenden Arbeitsgruppen zu den Themen unbemannte Systeme (UAVs, UVSs), mobile Kartierungssysteme (land-based mobile mapping systems), Anwendungen der Pléïades Satellitendaten und, zusammen mit der IAG (International Association of Geodesy), neue Trends bei der direkten Georeferenzierung.

Wichtigste Neuerung bei Kommission I ist die Ernennung des neuen Kommissionspräsidenten Charles Toth, Ohio State University, mit Boris Jutzi vom KIT aus Karlsruhe als Vizepräsidenten.

Franz Leberl wurde zu Beginn des Kongresses für seine Verdienste bei der Entwicklung der UltraCam Kamera mit der Brock Goldmedaille ausgezeichnet. Dieser revanchierte sich mit einem Vortrag über die Entstehungsgeschichte des UltraCam Systems. Die Idee für eine, so wie er sagt, zusätzlich ergänzende photogrammetrische Digitalkamera ist auf dem ISPRS Kongress in Amsterdam im Jahre 2000 entstanden, wo zeitgleich die ersten Versionen der DMC Kamera und der ADS40 vorgestellt wurden. Drei Jahre später wurde die erste Version der UltraCam Kamera vorgestellt und hat sich seitdem zu einem Markführer entwickelt. In weiteren Beiträgen wurden die Genauigkeiten der UltraCam und der DMC Kamera untersucht. Bemerkenswert


DOI: 10.1127/1432-8364/2013/0158 1432-8364/13/0158 $ 3.50

ist, dass die Systeme heute zwölf Jahre nach der Einführung der ersten digitalen photogrammetrischen Kamera eine praktisch fehlerfreie Sensorgeometrie aufweisen und die radiometrische Qualität deutlich über dem Niveau vergleichbarer analoger Systeme liegt.

Viele Beiträge befassten sich mit neuartigen Sensoren auf Flugzeugen, auf unbemannten Systemen (UAV/UVS) und auf mobilen Kartierungssystemen. Dabei werden oft handelsübliche optische Kameras mit verschiedenen Blickwinkeln zu einem Sensorsystem verknüpft, angefangen von flugzeuggestützten Fünf-Kamera-Systemen wie z.B. MIDAS mit vier schräg blickenden Kameras über einfachen Ein-Kamerasystemen auf Micro-UAVs bis hin zu mobilen Systemen wie Bubble Cam, einem 360° Kamerasystem zur Erfassung von Fassaden und Straßen (Street view). Eine Spezialentwicklung wie das flugzeuggestützte multispektrale, polarimetrisch und aus mehrfachen Blickwinkeln aufnehmende optische Sensorsystem AirMSPI der NASA dient als Vorläufer einer neuen multispektral-polarimetrischen Satellitenmission. Ähnlich innovativ ist auch der Einsatz einer 3D entfernungsmessenden Kamera (RIM) auf einem niedrig fliegenden UAV zur millimetergenauen Erfassung von Oberflächen. In diesem Zusammenhang wurde in den Beiträgen u.a. die Validierung der erreichten Genauigkeiten, die Problematik der exakten Georeferenzierung und Koregistrierung, die Kalibrierung, die Bildverbesserung und die Fusion der verschiedenen Sensordaten adressiert. So wurden u.a. Lösungen zur Kalibrierung schräg aufgenommener Bilder und zur Beseitigung von Unschärfen in UltraCam Bildern verursacht durch Rotationen des Flugzeugs während der Aufnahme vorgestellt.

Für mobile Kartierungssysteme wurden u.a. Lösungen zur Genauigkeitssteigerung bei kurzfristigen Ausfällen des GNSS, was häufig in Städten durch Verdeckungen geschieht, präsentiert. Für zukünftige Mondlandungen wurde ein Navigationssystem basierend auf einem Stereokamerasystem, einem Sternentracker, einem Schrittzähler und einer IMU vorgestellt, die den Astronauten bei der Fortbewegung auf dem Mond unterstützt. Getestet wurde dieses Verfahren in einem mondähnlichen Krater auf Hawaii.

Beiträge zu Satellitensystemen befassten sich mit neuen und zukünftigen Satellitenmissionen, wie z. B. die französischen Pléïades Satelliten mit optischen Sensoren, die Ende 2011 gestartet in der endgültigen Ausbaustufe mit zwei Satelliten täglich jeden Punkt auf der Erde mit einer Genauigkeit von 12 m und bis zu einer Auflösung von 70 cm abbilden werden können. In weiteren Beiträgen wurden auch der aktuelle Status des europäischen optischen Satellitensystems Sentinel-2 mit geplantem Start Ende 2013 und des deutschen hyperspektralen Satellitensystems EnMAP mit geplantem Start 2017 vorgestellt. Aktuelle Herausforderungen bei der Verarbeitung von Satellitendaten sind neben der präzisen und hochauflösenden DEM Generierung die flächendeckende kontinentale bzw. globale Ausgleichung von Satellitenszenen. Vorgestellt wurden hier u.a. eine globale Ausgleichung von SPOT-5 und Cartosat-1 Szenen, sowie eine kontinentale Ausgleichung von ALOS PRISM Szenen über Australien.

Zusammenfassend lässt sich festhalten, dass in den Beiträgen der Kommission I ein weites Spektrum von Sensoren auf sehr verschiedenen Plattformen verbunden mit einer Vielzahl möglicher Auswertemethoden präsentiert worden ist. Jedoch war die Anzahl von Beiträgen, die sich mit aktiven Sensoren wie LIDAR oder SAR beschäftigen, eher gering.

Franz Kurz, Oberpfaffenhofen

## Kommission II

In der Periode 2008 – 2012 wurde die Kommission von John Shi und seinem wissenschaftlichen Sekretär Eric Guilbert aus Hong Kong geleitet. In sieben Arbeitsgruppen und zwei mit der Kommission IV gemeinsamen Arbeitsgruppen wurden Fragen der raumbezogenen Datenanalyse, Modellierung und Visualisierung untersucht. Die Themen der Arbeitsgruppen reichten von Kognition über maßstabsabhängige Darstellungen, Data Mining, Unsicherheitsmodellierung bis hin zu entscheidungsunterstützenden Systemen. In der vierjährigen Phase wurden von den Arbeitsgruppen der Kommission über 20 Workshops und Symposien durchgeführt – teilweise auch in Kooperation mit anderen

Gesellschaften, z. B. der ICA. Die Beiträge wurden in verschiedenen Publikationsorganen abgedruckt, u.a. auch in Spezialausgaben des ISPRS Journals. Als besondere Aktivität der letzten Periode ist die Etablierung einer neuen Zeitschrift hervorzuheben: das ISPRS Journal of Geo-Information, welches unter Federführung von Wolfgang Kainz seit Ende 2011 erscheint. In 2010 fand in Hong Kong das Symposium statt, welches zusammen mit der Spatial Data Handling Konferenz abgehalten wurde. Dort wurde bereits eine Unterscheidung in Beiträge mit vollem Review-Prozess und solchen mit einem Review lediglich auf Basis einer Kurzfassung gemacht. Diese qualitätsbezogenen Maßnahmen wurden auch während des Weltkongresses in Melbourne durchgeführt. Dort gestaltete die Kommission Sitzungen und brachte insgesamt 68 Vorträge und 30 Poster zur Präsentation. Mit 33 Beiträgen ist die Kommission in den Annals vertreten, mit 37 in den regulären Proceedings.

Während des Kongresses wurden verschiedene Personen für ihr Engagement in der ISPRS ausgezeichnet. So erhielt John Shi den Wang Zhizhuo Preis und Tao Cheng eine President's citation für exzellente Arbeit in einer Arbeitsgruppe. Für die Deutsche wissenschaftliche Gesellschaft ist es eine besondere Freude, dass Jan-Henrik Haunert (Universität Würzburg, ehemals Leibniz Universität Hannover) den Otto-von-Gruber Preis gewonnen hat, eine hervorragende Auszeichnung für seine bedeutenden wissenschaftlichen Arbeiten im Bereich der Optimierungsverfahren für die Generalisierung von Geodaten.

Zum neuen Präsidenten der Kommission wurde Songnian Li aus Toronto gewählt. Er geht mit acht Arbeitsgruppen und drei Inter-Kommissionsarbeitsgruppen die Forschungsfragen in der nächsten Periode an. Einige der bestehenden Arbeitsgruppen werden fortgeführt. Hinzu kommen Arbeitsgruppen zur Bearbeitung sehr großer Datenmengen *Advanced Geo-Computing and Geo-Statistics for Big Spatial Data Processing*, zur Verarbeitung von Mobilitätsdaten *Mobility – Tracking, Analysis and Communication* sowie zur Datenintegration und Interoperabilität (Semantic Interoperability and Ontology for Geospatial Information).

Monika Sester, Hannover

## Kommission III

Kommission III war bei dem Kongress in Melbourne mit 66 Artikeln mit *full paper* review und 105 Artikel mit Abstract-Review vertreten. Die Sitzungen waren inhaltlich an die Arbeitsgruppen der zurückliegenden Periode 2008 – 2012 angelehnt: *Pose Estimation and Surface Reconstruction from Image and/or Range Data*, *3D Point Cloud Processing*, *Image Analysis for Indexation and Image Retrieval*, *Complex Scene Analysis and 3D Reconstruction* und *Image Sequence Analysis* sowie die Inter-Commission Arbeitsgruppe *Pattern Recognition in Remote Sensing.*

Alle Vortragssitzungen von Kommission III erfreuten sich eines großen und sehr diskussionsfreudigen Auditoriums. Nicht zuletzt die durch das strenge, wenn auch nicht immer transparente, Begutachtungsverfahren geförderte hohe Qualität der Beiträge führte dazu, dass für einige Sitzungen die Räumlichkeiten etwas knapp bemessen waren. Als kritisch sind dagegen die Posterveranstaltungen zu beurteilen. Auch wenn die neue, digitale Konzeption sehr vielversprechend ist, so standen doch deutlich zu wenige Präsentationsmöglichkeiten zu Verfügung.

Inhaltlich lässt sich festhalten, dass die automatische Bildanalyse eines der beherrschenden Forschungsthemen bleibt. Neben den klassischen Arbeiten der Detektion und Rekonstruktion von Gebäuden und Straßen aus optischen Bildern und Laserscanner Daten werden zunehmend Aufgaben der Bewegungs- und Veränderungsdetektion angegangen. Hierzu finden Lern- und Analysemethoden aus der Computer Vision basierend auf statistischer Modellierung von Objekten und deren Umgebung (Kontext) wie z. B. Conditional Random Fields oder Discriminative Random Fields Anwendung. Diese wurden auch für unterschiedliche Zeit- und Auflösungsskalen erweitert. Als Input dienen neben Bilddaten häufig dichte Tiefenkarten, die mittels modernen dense-matching Verfahren abgeleitet werden. Trotz der beachtlichen Fortschritte bleibt die Objektextraktion in natürlichen Umgebungen eine große Herausforderung für die Zukunft. Diese Entwicklungen werden zunehmend durch „real-time mapping" Methoden eweitert. Das große Potential von klei-

nen unbemannten Plattformen (UAVs, MAVs) konnte in einer Reihe von Studien aufgezeigt werden, die über mehrere Sitzungen verteilt waren. Eine Herausforderung bleiben Kalibrierungs-, Matching und Auswertemethoden in Echtzeit, die insbesondere aufgrund der unruhigen Flugeigenschaften und schlechteren Bildcharakteristiken weiteren Forschungsbedarf erzeugen.

Dem scheidenden Präsidenten Nicolas Paparoditis vom IGN in Paris mit seinem Team sei an dieser Stelle für die engagierte Leitung der Kommission III gedankt. Zum neuen Kommissionspräsidenten wurde Konrad Schindler, ETH Zürich, ernannt. Schindler ist nicht nur in der Photogrammetrie sondern gleichermaßen in der Computer Vision aktiv, was einen weiteren intensiven Austausch zwischen den beiden „communities" erwarten lässt. So soll z. B. das Mid-term Symposium 2014 in Zürich zusammen mit der European Conference on Computer Vision (ECCV) durchgeführt werden.

Stefan Hinz, Karlsruhe

## Kommission IV

Kommission IV wurde in der Zeit 2008 bis 2012 von Marguerite Madden, University of Georgia, geleitet. Während dieses Zeitraums bestand die Kommission aus folgenden Arbeitsgruppen:

- AG IV/1: *Geodateninfrastrukturen*
- AG IV/2: *Automatische Geodatenerfassung und bildbasierte Datenbanken*
- AG IV/3: *Kartierung aus hochaufgelösten Daten*
- AG IV/4: *Virtuelle Globen und kontextbasierte Visualisierung/Analyse*
- AG IV/5: *Verteilte und webbasierte Services und Anwendungen*
- AG IV/6: *Globale DHM Interoperabilität*
- AG IV/7: *Planetare Kartierung und Datenbanken*
- AG IV/8: *Integration von raumbezogenen 3D Daten für Katastrophenmanagement und Umweltmonitoring.*

Hinzu kommen die drei kommisions-übergreifenden Arbeitsgruppen:

- AG IV/II: *Geosensornetzwerke und GEOGRID*
- AG IV/VIII: *Fortführung und Verwaltung von räumlichen Basisdatenbanken*
- AG II/IV: *Semantische Interoperabilität und Ontologien von raumbezogenen Informationen*

Für den ISPRS-Kongress in Melbourne wurden in der Kommission IV 104 Beiträge zur Veröffentlichung ausgewählt. Die Arbeiten wurden in 24 Vortragssitzungen und sieben Postersitzungen vorgestellt. Die Beiträge finden sich in dem Band XXXIX Teil B4 auf 558 Seiten wieder.

Abb. 1 zeigt eine Auswertung der Beitragstitel aller Beiträge der Kommission IV als Wortwolke. Eine Wortwolke ist eine visuelle Darstellung der am häufigsten vorkommenden Wörter aus einer Liste. Die zwei am häufigsten vorkommenden Begriffe sind dabei DATA und IMAGE. Die Beiträge mit diesen Begriffen im Titel beschäftigen sich vor allem mit der Erfassung und der Fortführung von raumbezogenen Daten. Dieser Schwerpunkt wird von den Arbeitsgruppen IV/2 und IV/3 abgedeckt. Diese beiden Arbeitsgruppen bilden traditionell einen Schwerpunkt der Kommission IV. So finden sich 24 der 104 Beiträge in diesen beiden Arbeitsgruppen.

Betrachtet man die restlichen Begriffe der Wortwolke lassen sich nur schwer weitere Trends identifizieren. Vielmehr zeigt sich eine große Breite unterschiedlicher Themen. Die folgende Aufzählung zeigt die Schwerpunkte der publizierten Arbeiten:

- Geodateninfrastrukturen werden derzeit in vielen Ländern aufgebaut. Hier stellen vor allem die Standardisierung und Integration von Services und Daten eine große Herausforderung dar.
- Geodaten spielen immer mehr eine Rolle im Leben vieler Menschen. Neue Technologien, wie z. B. Programmierschnittstellen, wie Google API, Bing Maps API oder Yahoo Map API, ermöglichen eine einfache Integration von Geodaten in webbasierte Anwendungen.
- Die Erfassung von raumbezogenen Daten mit Web 2.0-Technolgien, wie z. B. OpenStreetMap, erschließt Anwendungsgebiete, die noch bis vor kurzem undenkbar waren.

- Im Bereich der Geodatenbanken gibt es einen Trend von 2-dimensionalen zu 3-dimensionalen Daten. Es lässt sich feststellen, dass die Erfassung, vor allem mittels Laserscanner, als auch die Visualisierung von 3D-Daten mittlerweile auch von sehr großen Datenbeständen möglich ist. Es besteht jedoch noch ein Defizit bei der Analyse und Datenhaltung.
- Die automatische bildbasierte Fortführung von Geodatenbanken ist trotz Fortschritten immer noch ein Forschungsthema.
- In den letzten vier Jahren hat sich die Anzahl der bildgebenden digitalen Sensoren weiter erhöht. Insbesondere der mittlerweile flächenhafte Einsatz von digitalen Luftbildkameras, aber auch neue Satellitensensoren, liefern umfangreiche und qualitativ hochwertige Daten zur Erfassung und Fortführung von raumbezogenen Daten.
- Fortschritte wurden im Bereich der Geosensornetzwerke erreicht. Hierbei handelt es sich um autonome, räumlich verteilte Infrastrukturen, welche verschiedenste Parameter erfassen und innerhalb eines Netzwerkes oder mit einer zentralen Instanz kommunizieren können. Geosensornetzwerke erfassen Daten nicht nur passiv, sondern können auch auf bestimmte Phänomene regieren, um bestimmte Ereignisse besser zu erfassen.

Für die nächste Periode (2012 bis 2016) geht die Präsidentschaft an Frau Jiang Jie, National Geomatics Center of China. Sie engagiert sich schon seit über 20 Jahren in der Forschung und Entwicklung von Geodateninfrastrukturen. In den letzten Jahren war sie verantwortlich für die Entwicklung einer nationalen Geodatenbank für e-Government in China als auch für den Aufbau einer landesweiten Plattform für raumbezogene Services. Mit dem Wechsel der Präsidentschaft ist auch immer eine Neuorientierung und Strukturierung der Kommission verbunden. Die momentan geplanten Änderungen sind eine Zusammenlegung der Arbeitsgruppen IV/2 und IV/3 in eine gemeinsame Arbeitsgruppe mit dem Titel: *Datenerfassung*, *Datenprozessierung und Datenvisualisierung von multisensoriellen und multiplattform Systemen*. Zusammengelegt werden sollen weiterhin die Arbeitsgruppen IV/6 und II/IV in eine gemeinsame Arbeitsgruppe mit dem Titel: *Dateninteroperabilität* sowie die Arbeitsgruppen IV/4 und IV/5 in eine gemeinsame Arbeitsgruppe mit dem Titel: *Web/Cloud-basierte Services*. Die beiden kommissionsübergreifenden Arbeitsgruppen IV/VII und IV/II werden eigenständige Arbeitsgruppen der Kommission IV mit den Titeln: *Fortführung, Versionierung und Archivierung von multiskaligen Daten von sehr großen Gebieten* bzw. *Sensor Web und*


**Abb. 1:** Auswertung aller Beitragstitel der Kommission IV als Wortwolke

*Internet der Dinge*. Die endgültige Struktur und Aufgaben der Arbeitsgruppen werden auf dem nächsten Treffen des ISPRS Councils im Dezember festgelegt. Bis dahin können sich noch Änderungen ergeben.

Der neuen Präsidentin und den neuen wie auch alten Arbeitsgruppenleitern wünschen die Verfasser für die kommende Arbeit in den nächsten vier Jahren viel Erfolg.

Volker Walter und Susanne Becker,
Stuttgart

## Kommission V

Die Kommission V der ISPRS befasst sich traditionell mit der Datenaufnahme, Datenverarbeitung und -analyse von Objekten im Nahbereich. Eine wesentliche Rolle spielen dabei die Verwendung einer Vielzahl unterschiedlicher bild- und distanzbasierter Sensoren und deren Kalibrierung, die Digitalisierung und 3D-Rekonstruktion von Objekten und die Herstellung von Folgeprodukten wie 3D-Modelle, Visualisierungen und Animationen. Wichtige Anwendungsbereiche der Kommission V bleiben die industrielle Messtechnik, die Robotik, die Dokumentation des Kulturerbes, die Sensortechnologie, die 3D-Modellierung und die Geowissenschaften. Anwendungen in der Medizin und Biometrie waren dieses Mal thematisch mit anderen Kommissionen verknüpft.

Die Kommission V war insgesamt an 18 Technical Sessions, fünf Poster Sessions, vier Theme Sessions und zwei Special Sessions (CIPA & ICOMOS) mit ihren Arbeitsgruppen beteiligt. Die Poster Sessions boten generell mit den ePostern, die über eine App für das iPhone oder Smartphone verfügbar waren, eine interessante Neuheit. Leider fehlten wie schon in den vorherigen Kongressen viele Poster-Präsentationen.

In den elektronischen Proceedings der Kommission V befinden sich 101 Beiträge, wobei 24 weitere Beiträge der Interkommissions-Arbeitsgruppe I/V der Kommission I zugeordnet wurden. Von den 125 Konferenzbeiträgen, an denen die Kommission V beteiligt ist, kommen 23 Beiträge (18,4%) aus Deutschland. Die Aufteilung auf die sechs Arbeitsgruppen zeigt folgendes Bild:

- WG V/1 *Vision Metrology – Best Practice, Systems and Applications*: 13 Beiträge, u.a. über Kamerakalibrierung bzw. Modellierung der Kamerageometrie, Genauigkeitstests von 3D-Messsystemen, Systemintegration, sowie diverse Anwendungen).
- WG V/2 *Cultural Heritage Data Acquisition and Processing*: 13 Beiträge. Eine Vielzahl sehr guter Berichte zur Erfassung, Modellierung und Dokumentation bzw. Überwachung von meist sehr attraktiven Objekten des Kulturerbes, aufgenommen mit verschiedenen Sensoren oder Sensorkombinationen. Oberflächenmessungen, Texturierung und Genauigkeitsvergleiche standen hier im Vordergrund.
- WG V/3 *Terrestrial Laser Scanning and 3D Imaging*: 18 Beiträge. Berichte zur Registrierung, Integration, Weiterverarbeitung und Interpretation der erfassten Punktwolken, zur Fusion von TLS und Bilddaten sowie Anwendungen, vor allem mobiler Systeme, Deformations- bzw. Bewegungsmessungen mit Laserscannern.
- WG V/4 *Image-Based and Range-Based 3D Modelling*: 10 Beiträge, u. a. zur automatischen Objekttexturierung, 3D-Modellierung durch Edge-Matching in Bilddaten und Punktwolken, effiziente Schadensbeurteilung von Brücken und Oberflächenmodelle von Tunneln durch Bilddaten, automatisierte CAD-Modellierung unter Nutzung geometrischer Primitiver, automatische Bildorientierung, adaptives Dense Stereo Matching sowie die Schätzung von Baumparametern aus Bildern.
- WG V/5 *Image Sensor Technology*: 14 Beiträge. Vergleiche verschiedener Ansätze zur Kamerakalibrierung, Untersuchungen von Kameras mit speziellen Optiken (Fisheye-Objektive, Spiegellinsenobjektive), Panoramakameras, Handy-Kameras, Stereo-Videokameras, Laserscanner, etc.
- WG V/6 *Close Range Morphological Measurement for the Earth Sciences*: 8 Beiträge, vor allem Oberflächenerfassungen in topographischen Umgebungen wie Gletscher oder Gebirgsregionen.

Hinzu kommen die Beiträge für die Inter-Commission Working Groups sowie die Theme und Special Sessions:

- IC WG V/I *Land-Based Mobile Mapping Systems* (zusammen mit Kommission I; 11 Beiträge)
- IC WG I/V *Unmanned Vehicle Systems (UVS) for Mapping and Monitoring Applications* (24 Beiträge, siehe Bericht zur Kommission I)
- 4 Theme Sessions: *Morphological Change Detection* (V/6 & IV/8 – 4 Beiträge), *Waveform Lidar for Remote Sensing* (III/2, V/3 & VII/7 – 4 Beiträge), *Medical Imaging and Human Motion* (TC III/V – 4 Beiträge) und *Low-cost UAVs and Mobile Mapping Systems* (div. WGs – 2 Beiträge)
- 2 Special Sessions: CIPA, ICOMOS and WG V/2 – *Advances in Digital Documentation* (8 Beiträge)

Das Poster *Investigations on a combined RGB/ Time-of-Flight Approach for close range applications* von Heidi Hastedt and Thomas Luhmann (Oldenburg) hat den Best Poster Award der Kommission V erhalten. Zusammenfassend lässt sich festhalten, dass es im Vergleich zum Kongress in Peking signifikant weniger Beiträge in der Kommission V gab. Die Anzahl der Beiträge und der Teilnehmer in den entsprechenden Sitzungen zeigte während des Kongresses deutlich, dass immer noch ein großer „Hype" im Bereich der Unmanned Vehicle Systems besteht.

Bereits im Vorfeld des Kongresses hat sich die Kommission V entschlossen, der ISPRS-Generalversammlung die Änderung des Kommissionsnamens in *Close-range imaging, analysis and applications* vorzuschlagen. Während des Kongresses in Melbourne wurden von der Kommission V folgende drei Resolutionen in die Generalversammlung eingereicht: (1) Gaming Sensors – die ISPRS Forschungsaktivitäten sollen auf aktive 3D-Sensor erweitert werden, um die Anwendung und Entwicklung dieser Sensoren aus der Spieleindustrie für Messaufgaben einzubinden, (2) Mobile Mapping – vertiefte Forschung in der automatisierten Objekterkennung in Punktwolken, die durch mobile Plattformen erfasst werden. Dabei soll die Zusammenarbeit zwischen den Kommissionen I, III und V in Bezug auf solche Systeme vertieft werden und (3) Open-source und freie web-basierte Objektrekonstruktion mit Bilddaten von Konsumerkameras – Untersuchungen über die on-line Leistungsfähigkeit der genauen 3D-Objektrekonstruktion aus beliebig verfügbaren Bilddaten und zugehörigen Informationen, um durch dieses Thema auch Nicht-Photogrammeter in die ISPRS Aktivitäten einzubinden.

Für die Periode 2012–2016 wurde die Präsidentschaft der Kommission V an Fabio Remondino (Fondazione Bruno Kessler, Trento, Italia) übergeben. Das Mid-term Symposium der Kommission V ist für den 24.–27.6.2014 in Riva del Garda in Italien geplant. Die Struktur der Kommission V ist wie folgt vorgesehen: WG V/1 – Vision metrology, WG V/2 – Cultural heritage data acquisition and processing, WG V/3 – Terrestrial 3D imaging and sensors, WG V/4 – 3D modelling: algorithms and methods, WG V/5 – Close-range measurements for bio- and geosciences, ICWG V/I – Landbased mobile mapping system und ICWG I/V – UVS for mapping and monitoring applications.

Thomas Kersten, Hamburg, und Thomas Luhmann, Oldenburg

## Kommission VI

Wie bereits in den vorhergehenden Kongressen der ISPRS blieb die Beteiligung im Bereich Aus- und Weiterbildung im Vergleich zu der Beitragsdichte der Kommissionen mit wissenschaftlichen Inhalten unter den Erwartungen. Dennoch fiel die Bilanz in Melbourne überaus positiv aus: die Fachvorträge der Kommission VI konnten erfolgreich in neun Technischen Sessions vorgestellt und diskutiert werden. Allerdings waren die Vortragssäle selten voll, was bei meist mehr als 10 parallelen Sessions nicht verwunderlich war. Dies betraf allerdings nicht ausschließlich Beiträge der Kommission VI allein.

Die Schwerpunkte der Fachvorträge konzentrierten sich auf Curriculum- und Ausbildungsfragen in den jeweiligen Fachgebieten und beschäftigten sich mit der Entwicklung von Lernmaterialien und Strategien zu deren Nutzung. Besondere Bedeutung kommt der internationalen Zusammenarbeit und Kooperation zu. In den Vorträgen und anschließenden Diskussionen betonten die Teilnehmer der

Arbeitskreissitzung der *WG VI/4 Cross-Border Education – Joint Educational Programs* die Notwendigkeit der Erweiterung von Kompetenz durch Qualifizierungsmaßnahmen und die Unterstützung von fördernden Strukturen und Mechanismen für den Technologietransfer.

Eine zentrale Rolle beim Wissenstransfer spielt die konsequente Nutzung des Internets, wodurch ein verteiltes Lehren und Lernen über Grenzen hinweg möglich wird. Diese Themen wurden in den Beiträgen der *WG VI/1 Web based Education* bzw. *WG VI/2 E-Delivery of Education Services* diskutiert. Nicht nur für Entwicklungsländer ist die Arbeit mit kostenfreier Lernsoftware und Datenmaterial wertvoll, auch Dozenten in technisch entwickelten Regionen können die bereitgestellten Module für die eigene Lehre nutzen oder Anregungen dafür darin finden. Informationen über Angebot und Qualität frei verfügbarer Ressourcen war deshalb Gegenstand der Vorträge ebenso wie Fragen zur Entwicklung attraktiver und nachhaltiger E-Learning Software.

Positiv hervorzuheben sind die Aktivitäten des 2004 in Istanbul initiierten *Student Consortiums* (*SC*), die im Rahmen der *WG VI/5 Promotion of the Profession to Young People* vorgestellt wurden. Das SC dient der Netzwerkbildung und spricht gezielt den wissenschaftlichen Nachwuchs an, der durch Fördermaßnahmen durch die ISPRS Foundation unterstützt wird und u.a die Teilnahme an Summer Schools, Workshops und Kongressen ermöglicht. In Melbourne wurden vom SC vier Sessions des Youth Forums (YF) organisiert, in denen junge, unter 30 jährige Wissenschaftler ihre Arbeiten zu aktuellen Themen den Kongressteilnehmern präsentierten. Den von Leica-Geosystems/Hexagon gestifteten Best Paper Award des YF (1000 CHF) erhielt Wilfried Hartmann von der ETH Zürich für den Beitrag *Determination of the UAV Position by Automatic Processing of Thermal Images*. Xue Wan (Wuhan Universität) wurde für ihren Vortrag *An Improved Algorithm Used in Automatic Matching for Low-altitude Aerial Image* mit dem Best Presentation Award im Youth Forum ausgezeichnet.

Zum sechsten Mal fand der Computer Assisted Teaching Contest (CATCON) statt, an dem sich Entwickler kostenfreien Lernmaterials beteiligen können. Nach einführenden Kurzvorträgen gaben die Wettbewerbsteilnehmer in praktischen Vorführungen den Besuchern Gelegenheit ihre Produkte zu testen und zu beurteilen. In diesem Jahr wurden dank der ISPRS Foundation sehr großzügige Prämien vergeben: den Gold Award (3000 CHF) erhielt das Department of Primary Industries (State Government of Victoria, Australien) um Mark Imhof. Es handelt sich dabei um eine Internet basierte Landschaftsvisualisierung (www.dpi.vic.gov.au/vro), in der durch interaktive Landschaftspanoramen, grafische Animationen und Experten-Videos Landschaftsformen, Bodenprofile und Landschaftsentwicklung in Victoria anschaulich erläutert und vermittelt werden. Mit dem zweiten Preis (2500 CHF) wurde die Wissenschaftlergruppe um Diego Gonzalez-Aguilera der Universität Salamanca, Spanien ausgezeichnet, die mit *PW – Photogrammetric Workstation* ein semi-professionelles Programm zur photogrammetrischen Auswertung vorstellten. Interessenten können die für den Lehrbetrieb ausgezeichnete Software auf Anfrage von den Entwicklern kostenfrei beziehen (daguilera@usal.es; dguerrero@usal.es). Der dritte Preis (1500 CHF) wurde ebenfalls an ein photogrammetrisches Programmsystem vergeben: *E-Photo*, das am Institut für Cartographic Engineering der Rio de Janeiro State University (UERJ), Brasilien entwickelt wurde (Jorge Luis Nunes e Silva Brito et al.). Ausführbare Module für Linux, Windows und in Kürze auch für MacOS stehen unter www.efoto.eng.uerj.br/en zum Download bereit. Alle Beiträge der Kommission VI sind wie gewohnt im Tagungsband veröffentlicht bzw. können online abgerufen werden.

Besonderer Dank gilt dem ehemaligen Kommissionspräsidenten Martien Molenaar (ITC Enschede), der nach Ablauf seiner Amtsperiode von Jianya Gong (Wuhan University) abgelöst wurde. Inhaltliche Schwerpunkte werden sich weiterhin auf die Themen Capacity Building und E-Learning / Internet Resources fokussieren. Eine engere Kooperation mit den benachbarten Schwesterorganisationen FIG (International Federation of Surveyors) und ICA (International Cartographic Association), die in den kommenden Jahren zu gemeinsamen Workshops führen soll, stellt ein

wesentliches Anliegen zukünftiger Aktivitäten der Kommission VI dar.

GERHARD KÖNIG, Berlin

## Kommission VII

Nach dem ISPRS Kongress 2008 in Peking war die Kommission VII mit sieben Arbeitsgruppen und der kommissionsübergreifenden Arbeitsgruppe ICWG III/VII *Pattern Recognition for Remote Sensing* an den Start gegangen. Der gerade vergangene ISPRS-Kongress in Melbourne bot nun die Gelegenheit, sich über den Bereich der Kommission VII ein aktuelles Bild zu verschaffen.

Zum zweiten Mal – nach dem Symposium 2010 in Wien – gab es zwei unterschiedliche Modalitäten zur Einreichung von Beiträgen: Zum einen als vollständige Beiträge *Full reviewed paper* – wie auch in anderen Kommissionen – zur Veröffentlichung in den neu geschaffenen Annalen, zum anderen wie bisher als Zusammenfassung zur Veröffentlichung in den Archiven, ehemals Teil B des Tagungsbandes. Die Veröffentlichungen der Kommission VII zum ISPRS-Kongress umfassen 60 begutachtete vollständige Beiträge in den Annalen und 97 Beiträge in den Archiven. Die Beiträge wurden in mehr als 30 Sitzungen im Rahmen von Vorträgen oder im neuen Format der Kurzpräsentation mit anschließender interaktiver Vorstellung präsentiert. Die Beiträge verteilten sich gemäß Programm wie folgt auf die verschiedenen Arbeitsgruppen: VII/1 *Physical Modelling and Signatures in Remote Sensing* mit 9 Vorträgen und 13 Kurzpräsentationen, VII/2 *SAR Interferometry* mit 8 Vorträgen, VII/3 *Information Extraction from Hyperspectral Data* mit 19 Vorträgen und 7 Kurzpräsentationen, VII/4 *Methods for Land Cover Classification* mit 24 Vorträgen und 15 Kurzpräsentationen, VII/5 *Methods for Change Detection and Process Modelling* mit 23 und 15 Kurzpräsentationen zusammen in einer Sitzung mit der Arbeitsgruppe VII/6 *Remote Sensing Data Fusion* mit 13 Vorträgen, VII/7 *Theory and Experiments in Radar and Lidar* mit 7 Vorträgen in eigenen Sitzungen sowie weiteren Sitzungen in Kombination mit anderen Arbeitsgruppen. Im Rahmen von Sitzungen der kommissionsübergreifenden Arbeitsgruppe ICWG III/VII *Pattern Recognition for Remote Sensing* gab es 5 Vorträge und 17 Kurzpräsentationen. Das Programm wurde abgerundet durch eine eigene Sitzung *Highlights of TC VII* – leider parallel zu einer anderen Arbeitsgruppensitzung – mit 4 Vorträgen und Vorträgen im Rahmen von Plenarsitzungen z. B. von RAINER SANDAU (Small Satellites – Status, Opportunities and Challenges), MADHU CHANDRA (Whither Radar Remote Sensing?) und RANGANATH NAVALGUND (Earth Observation for Early Warning Systems). Im Detail auf Beiträge einzugehen würde den Rahmen dieses Berichtes sprengen. Alle Beiträge stehen unter den bereits oben genannten Links zur Verfügung.

Insgesamt handelte es sich um ein volles Programm und damit verbunden fast durchgängigen Parallelsitzungen im Rahmen der Kommission VII, ganz abgesehen davon, dass es in Sitzungen der anderen Kommissionen interessante Beiträge mit Bezug zur Fernerkundung gab. Ein fleißiger Kongressbesucher hatte somit die Qual der Wahl: Welche Vortragssitzung soll ich besuchen? Das Sitzungsprogramm ist im Wesentlichen durch die Einteilung der Kommissionen und deren Arbeitsgruppen definiert. Dieses bereitet Autoren bereits bei der Einreichung von Beiträgen Schwierigkeiten, weil die Frage zu klären ist, in welcher Arbeitsgruppe Beiträge thematisch am besten aufgehoben seien. Für den Bereich Fernerkundung gilt dies aufgrund der Aufteilung in zwei Kommissionen trotz der Einteilung in Methodik und Anwendungen in besonderem Maße.

Insgesamt betrachtet war der ISPRS-Kongress Melbourne bezüglich Kommission VII eine gelungene Veranstaltung. Eine solche Veranstaltung bietet eine Plattform, um bestehende Kontakte zu pflegen und neue zu knüpfen. Die Einführung des Reviews von vollständigen Beiträgen in der vergangenen Periode von 2008 bis 2012 ist eine richtige Entscheidung. Dies bedeutet für die Organisatoren einen großen Aufwand und zeitlichen Vorlauf, insbesondere, wenn im Rahmen des Reviewprozesses tatsächlich Zeit für eine Iteration zur Stellungnahme und Verbesserung der Beiträge vorgesehen wird. Den Organisatoren aus Kommission VII und dem örtlichen Organisationsteam ist für die Durchführung

des diesjährigen Kongresses herzlich zu danken.

Für die nach dem Kongress startende neue Periode ist die Kommissionspräsidentschaft an Filiz Sunar (ITU, Istanbul) übergegangen. Wolfgang Wagner (IPF, Wien) wird als Vize-Präsident weiterhin in der Kommission tätig sein. Die Arbeitsgruppen der Kommission VII für die Periode 2012–2016 müssen noch vom ISPRS-Council bestätigt werden, jedoch kann man schon jetzt sagen, dass die bisherigen Arbeitsgruppen mit ihren Themen im Wesentlichen weitergeführt werden.

Uwe Weidner, Karlsruhe

## 12th European Conference on Computer Vision (ECCV), 7.–13. Oktober 2012, Florenz, Italien

Vom 7.–13. Oktober 2012 fand in Florenz, Italien, die 12th European Conference on Computer Vision (ECCV) statt. Die Veranstaltung bestand aus einem viertägigen Konferenzteil, der von 8 Tutorials und 21 Workshops im Vorfeld und Anschluss begleitet wurde. Mit etwas mehr als 1100 Teilnehmern war die Veranstaltung sehr gut besucht.

Inhaltliche Schwerpunkte des Konferenzteils waren *Geometry: Theory and Application*, *Learning and Large-Scale Recognition*, *Detection and Attributes*, *Actions and Activities*, *MRFs and Early Vision*, *Geometry and Recognition*, *Lights, Action* und *Semantic Segmentation*. Von 1437 eingereichten Beiträgen wurden 40 (2,8%) in Form eines Vortrags und 368 (25,6%) als Poster präsentiert. Damit lag die gesamte Annahmequote im Rahmen des für die Veranstaltung üblichen Review-Prozesses bei 28,4%, was eine hohe Qualität der vorgestellten Arbeiten sicherstellte. Parallel zu den Poster Sessions, welche eine gute Möglichkeit zum wissenschaftlichen Austausch hinsichtlich spezieller Themen boten, wurden noch zusätzlich 22 Live Demonstrationen bezüglich bestimmter Verfahren, Sensoren oder Systemen gezeigt.

Die Kathedrale Santa Maria del Fiore (Baujahr: 1436)

Als Gastredner war Tomaso Poggio vom McGovern Institute des MIT eingeladen, der in seinem Vortrag zum Thema *The Quest for a Theory of Vision: From the Level Framework to the Invariances of the Ventral Stream* auf die Analyse von Wahrnehmungsprozessen, das Verstehen menschlicher Intelligenz und den technischen Transfer in Form von intelligenten Maschinen einging.

Wie bei der letzten ECCV wurden wieder besondere Arbeiten mit Preisen ausgezeichnet. Der Best Paper Award ging an Daniel Küttel, Matthieu Guillaumin und Vittorio Ferrari für ihre Arbeit zum Thema *Segmentation Propagation in ImageNet*. Die Arbeit *Activity Forecasting* von Kris Kitani, Brian D. Ziebart, James Bagnell und Martial Hebert wurde mit dem Best Paper Award – Honorable Mention ausgezeichnet. Der Best Student Paper Award wurde an Jianxiong Xiao und Yasutaka Furukawa für ihre Arbeit zum Thema *Reconstructing the World's Museums* verliehen. Der Koenderink Prize for Fundamental Contributions in Computer Vision wurde an Vladimir Kolmogorov und Ramin Zabih für ihre Arbeit zum Thema *What Energy Functions Can Be Minimized via Graph Cuts?* vergeben. Mit dem Demo Paper Award wurde die Arbeit *Emotion Mirror: A Novel Intervention for Autism Using Real-Time Expression Recognition* von David Derisory, Josh Susskind, Lauren Kreiger und Marian Bartlett ausgezeichnet.

Als Ausgleich zum umfangreichen fachlichen Programm wurden drei Social Events angeboten, welche den Konferenzteilnehmern Einblicke in das historische und kulturelle Erbe von Florenz boten sowie weitere Austauschmöglichkeiten eröffneten. Am ersten Tag des Konferenzteils wurde ein Welcome Dinner in der Fortezza da Basso, einer Festungsanlage aus dem 16. Jahrhundert, angeboten, umrahmt von historischen Darbietungen in Form von Gesang und Tanz der Renaissance. Am folgenden Tag waren die Konferenzteilnehmer abends zur Darbietung eines gregorianischen Gesangs in die Basilika San Miniato al Monte, welche sich auf einem der

Die Basilika San Miniato al Monte von innen

höchsten Punkte der Stadt befindet und als eine der schönsten Kirchen in Italien gilt, geladen. Das Social Dinner fand am dritten Tag des Konferenzteils in der Stazione Leopolda, dem ehemaligen und mittlerweile historischen Bahnhof von Florenz, unter Begleitung von Harmoniemusik statt.

Abschließend lässt sich festhalten, dass die ECCV 2012 eine gut organisierte und fachlich hervorragende Veranstaltung in angenehmer Umgebung war. Die Vorträge sowie der wissenschaftliche Austausch im Rahmen von Poster Sessions und Social Events boten eine sehr gute Möglichkeit zur wissenschaftlichen Weiterbildung und zur internationalen Vernetzung zwischen den Teilnehmern.

Die nächste ECCV wird 2014 in Zürich, Schweiz, stattfinden. Für 2016 wurde Amsterdam, Niederlande, als Austragungsort gewählt.

Martin Weinmann, Karlsruhe

## Neuerscheinung

Klärle, M. (2012): Erneuerbare Energien unterstützt durch GIS und Landmanagement. – Wichmann-Verlag, 448 Seiten. ISBN 978-3-87907-518-8.

Die Umsetzung der Energiewende liegt in der Hand von Kommunen, Landkreisen und Regionen. Potenziale erkennen, Standorte finden – dazu brauchen die Gebietskörperschaften objektive, transparente Diskussionsgrundlagen und Entscheidungshilfen. Hier können Landmanagement und Geoinformation einen wichtigen Beitrag leisten. Der erste Teil des Buchs widmet sich den aktuellen bodenpolitischen und planungs-rechtlichen Grundlagen der Energiewende sowie der zukünftigen Weiterentwicklung der Planungsinstrumente. Im zweiten Teil der interessanten Neuerscheinung werden GIS-basierte Werkzeuge und konkrete Anwendungsbeispiele vorgestellt, welche für die Gebietskörperschaften bei der Umsetzung der Energiewende von unschätzbarem Wert sind: Solardachkataster, ganzheitliche Potenzialanalysen für alle Formen der Erneuerbaren Energien, Sichtbarkeitsanalysen, flexible Energienetze, etc.

# Veranstaltungskalender

**2013**

13.–14. Februar: **Oldenburger 3D-Tage**. jade-hs.de/3dtage

17.–23. Februar: 17. **Internationale Geodätische Woche** in **Obergurgl**, Österreich. uibk.ac.at/vermessung/veranstaltung/obergurgl.html

27. Februar – 1. März: **DGPF Jahrestagung 2013 (Dreiländertagung)** in **Freiburg**. dgpf.de/neu/jahrestagung/informationen.htm

13.–15. März: **Geoinformatics 2013** in **Heidelberg**. geoinformatik2013.de

19.–20. März: **Internationales 3D-Forum Lindau**, 3d-forum.li

24.–28. März: **ASPRS Annual Meeting** in **Baltimore**, USA. asprs.org/Conferences/Baltimore-2013

21.–23. April: **Joint Urban Remote Sensing Event (JURSE 2013)** in **Sao Paulo**, Brasilien. inpe.br/jurse2013/

30. April – 2. Mai: 8th **International Symposium on Mobile Mapping Technology 2013** in **Tainan**, Taiwan. conf.ncku.edu.tw/mmt2013/

6.–7. Mai: 19. **Workshop Computer-Bildanalyse in der Landwirtschaft / 2. Workshop Unbemannte autonom fliegende Systeme (UAS) in der Landwirtschaft**, Beuth Hochschule für Technik in **Berlin**. atb-potsdam.de/workshop-cba-uas .

6.–8. Mai: **Symposium Königslutter 2013** der DGfK in **Königslutter am Elm**. angewandte-kartographie.de/

21.–23. Mai: **IAPR Conference on Machine Vision Applications (MVA 2013)** in **Kyoto**, Japan. mva-org.jp/mva2013/

21.–24. Mai: **ISPRS Hannover-Workshop „High-Resolution Earth Imaging for Geospatial Information“** in **Hannover**. ipi.uni-hannover.de

3.–6. Juni: 33rd **EARSeL Symposium** in **Matera**, Italien. earsel.org/symposia/2013-symposium-Matera/

23.–28. Juni: **Computer Vision and Pattern Recognition (CVPR 2013)** in **Portland**, USA. pamitc.org/cvpr13/

14.–20. Juli: **International Computer Vision Summer School** in **Punta Sampieri**, Italien. svg.dmi.unict.it/icvss2013/

21.–26. Juli: **IGARSS 2013** in **Melbourne**, Australien. igarss2013.org/

25.–30. August: 26th **International Cartographic Conference (ICC)** in **Dresden**. icc2013.org/

2.–6. September: XXIVth **CIPA Heritage Documentation Symposium** in **Strasbourg**, Frankreich. cipa.icomos.org

9.–13. September: 54. **Photogrammetrische Woche** in **Stuttgart**. ifp.uni-stuttgart.de/phowo

9.–13. September: **British Machine Vision Conference (BMCV 2013)** in **Bristol**, England. bmvc2013.bristol.ac.uk/

15.–18. September: **International Conference on Image Processing (ICIP 2013)** in **Melbourne**, Australien. www.ieeeicip.org/

8.–15. Dezember: **ICCV 2013**, International Conference on Computer Vision, **Sydney**, Australien. iccv2013.org

# Korporative Mitglieder

**Firmen**

AEROWEST GmbH
AICON 3D Systems GmbH
aphos Leipzig AG
Becker GeoInfo GmbH
Bernhard Harzer Verlag GmbH
Blom Deutschland GmbH
Brockmann Consult GmbH
bsf swissphoto GmbH
Büro Immekus
CGI Systems GmbH
con terra GmbH
DB Netz AG
DELPHI IMM GmbH
Deutsches Bergbau-Museum
EFTAS Fernerkundung Technologietransfer GmbH
ESG Elektroniksystem- und Logistik-GmbH
Esri Deutschland GmbH
EUROPEAN SPACE IMAGING
Eurosense GmbH
fokus GmbH
g.on experience gmbh
GAF GmbH
GeoCart Herten GmbH
GeoContent GmbH
Geoinform. & Photogr. Engin. Dr. Kruck & Co. GbR
geoplana Ingenieurgesellschaft mbH
GEOSYSTEMS GmbH
GGS - Büro für Geotechnik, Geoinformatik, Service
Hansa Luftbild AG
IGI - Ingenieur-Gesellschaft für Interfaces mbH
ILV Ingenieurbüro für Luftbildauswertung und Vermessung
Imetric 3D GmbH
Infoterra GmbH
INVERS - Industrievermessung & Systeme
ITT Visual Information Solutions Germany
J. Linsinger ZT-GmbH
Jena-Optronik GmbH
Leica Geosystems GmbH
Luftbilddatenbank-Würzburg
Messbildstelle GmbH
Microsoft Photogrammetry
MILAN Geoservice GmbH
M.O.S.S. Computer Grafik Systeme GmbH
PHOENICS GmbH
PMS - Photo Mess Systeme AG
RIEGL Laser Measurement Systems GmbH
RWE Power AG, Geobasisdaten/Markscheidewesen
technet GmbH
TRIGIS Vermessung + Geoinformatik GmbH
Trimble Germany GmbH
trimetric 3D Service GmbH
Wichmann, VDE Verlag GmbH
Z/I Imaging Ltd.

**Behörden**

Amt für Geoinformationswesen der Bundeswehr
Bayerische Landesanstalt für Wald und Forstwirtschaft
Bundesamt für Kartographie und Geodäsie
Bundesmininisterium für Ernährung, Landwirtschaft und Verbraucherschutz
Hessisches LA für Bodenmanagement und Geoinformation
Innenministerium NRW, Gruppe Vermessungswesen
Institut für Umwelt- und Zukunftsforschung
LA für Geoinformation und Landentwicklung, BW
LA für Vermessung und Geoinformation, Bayern
LB Geoinformation und Vermessung, Hamburg
LB für Küstenschutz, Nationalpark und Meeresschutz, SH
Landesvermessung und Geobasisinformation Niedersachsen
Märkischer Kreis, Vermessungs- und Katasteramt
Regierungspräsident Tübingen, Abt. 8 Forstdirektion
Regionalverband Ruhr
Staatsbetrieb Sachsenforst Pirna
Stadt Bocholt, Fachbereich 31
Stadt Düsseldorf, Vermessungs- und Katasteramt
Stadt Köln, Amt für Liegenschaften, Vermessung und Kataster
Stadt Wuppertal, Vermessung, Katasteramt und Geodaten
Thüringer LA für Vermessung und Geoinformation

**Hochschulen**

BTU Cottbus, Lehrstuhl für Vermessungskunde
FH Frankfurt a.M., FB 1, Studiengang Geoinformation
FH Mainz, Institut für Raumbezogene Informations- und Messtechnik
Jade Hochschule, Institut für Angewandte Photogrammetrie und Geoinformatik
HCU HafenCity Universität Hamburg, Geomatik
HfT Stuttgart, Vermessung und Geoinformatik
HS Bochum, FB Vermessung und Geoinformatik
HS Karlsruhe, Fakultät für Geomatik
HTW Dresden, FB Vermessungswesen/Kartographie
LUH Hannover, Institut für Kartographie und Geoinformatik
LUH Hannover, Institut für Photogrammetrie und Geoinformation
MLU Halle, FG Geofernerkundung
Ruhr-Uni Bochum, Geographisches Institut
RWTH Aachen, Geodätisches Institut
TU Bergak. Freiberg, Institut für Markscheidewesen und Geodäsie
TU Berlin, Computer Vision & Remote Sensing
TU Berlin, Institut für Geodäsie und Geoinformationstechnik
TU Braunschweig, Institut für Geodäsie und Photogr.
TU Clausthal, Institut für Geotechnik und Markscheidewesen
TU Darmstadt, Institut für Photogrammetrie und Kartographie
TU Dresden, Institut für Photogrammetrie und Fernerkundung
TU München, FG Photogrammetrie und Fernerkundung
TU Wien, Institut für Photogrammetrie und Fernerkundung
Uni Bonn, Institut für Photogrammetrie
Uni Göttingen, Institut für Waldinventur und Waldwachstum
Uni Heidelberg, IWR Interdisziplinäres Zentrum für Wissenschaftliches Rechnen
Uni Kassel, FB Ökologische Agrarwissenschaften
Uni Kiel, Geographisches Institut
Uni Stuttgart, Institut für Photogrammetrie
Uni Würzburg, Geographisches Institut
Uni zu Köln, Geographisches Institut